Measurement of the Neutron (^{3}He) Spin Structure Function at Low Q^2 : a connection between the Bjorken and Drell-Hearn-Gerasimov sum rules.

Thesis by

John Steffen Jensen

In Partial Fulfillment of the Requirements
for the Degree of
Doctor of Philosophy

California Institute of Technology
Pasadena, California

2001

(Submitted August 28, 2000)

Acknowledgements

or

How Steffen got his Thesis

Starring

Emlyn "The Hammer" Hughes

David "Phone Call Time" Pripstein

Connie "Puts up with me" Jensen

Jang Ping "No error is small enough" Chen

Gordon "Story Time" Cates

Zein-Eddine "Cross section while we're at it" Meziani

Alex "The French Connection" Deur

Ioannis "Come on Man" Kominis

Karl "Impression Master" Sliffer

Pibero "Run for the Border" Djawotho

Seonho "With Child" Choi

"M.C." Xiaodong Jiang

Wolfgang "Put a label on everything" Korsch

Ed "Magic Oil" Folts and the entire Hall A team

John "Physica Master" Arrington

and

Various Kelloggites

Abstract

The spin dependent cross sections, $\sigma^T_{1/2}$ and $\sigma^T_{3/2}$, and asymmetries, $A_{||}$ and $A_\perp$, for ^{3}He have been measured at the Jefferson Lab's Hall A facility. The inclusive scattering process $^3\vec{\mathrm{He}}(\vec{e},e)X$ was performed for initial beam energies ranging from 0.86 to 5.1 GeV, at a scattering angle of 15.5°. Data includes measurements from the quasi-elastic peak, resonance region, and the deep inelastic regime. An approximation for the extended Gerasimov-Drell-Hearn integral is presented at a 4-momentum transfer Q^2 of 0.2-1.0 GeV^2.

Also presented are results on the performance of the polarized ^{3}He target. Polarization of ^{3}He was achieved by the process of spin-exchange collisions with optically pumped rubidium vapor. The ^{3}He polarization was monitored using the NMR technique of adiabatic fast passage (AFP). The average target polarization was approximately 35% and was determined to have a systematic uncertainty of roughly ±4% relative.

Contents

List of Figures

List of Tables

Chapter 1 Introduction

1.1 Polarized Electron Scattering

In 1988 the European Muon Collaboration (EMC) at CERN published results on the spin structure of the proton [5, 6]. They measured the proton spin structure function by scattering high energy polarized muons by a polarized ammonia target. Before the EMC result it was expected that the three valence quarks (up, up, and down) could account for the proton's spin. Such a line of thinking did not seem unreasonable since the naive quark model appeared to do quite well at explaining the charge, the magnetic moment, parity, isospin, and symmetry properties of hadrons [7]. Indeed early experiments at the Stanford Linear Accelerator Center (SLAC) confirmed the premise that the valence quarks were the dominate contribution to the proton's spin [8, 9]. By measuring the quark contribution over a wider kinematic region, the European Muon Collaboration found that the quark contribution was $12\% \pm 9\%_{stat} \pm 14\%_{sys}$, a small value consistent with zero. The resulting situation was dubbed the "proton spin crisis."

What followed was an explosion in theoretical work. In addition a number of experimental programs began dedicated to understanding the spin structure of the proton, neutron, and deuteron. The European Muon Collaboration reorganized into the Spin Muon Collaboration (SMC) and became dedicated to studying both the proton and deuteron spin structure functions [10]. Meanwhile, at the Stanford Linear Accelerator Center (SLAC) a series of experiments began using a polarized electron beam and polarized ^{3}He, ammonia, and Lithium Deuteride (LiD) targets to extract the spin structure functions of the neutron, proton, and deuteron: E142 [11], E143 [12], E154 [3], and E155 [13]. In Europe, at DESY, the HERMES collaboration began a

program using polarized electrons and polarized hydrogen, deuterium, and ^{3}He [14]. For a recent review of these experiments, see [15].

Much of this recent work focused on measuring the Bjorken sum rule:

$$\int_0^1 (g_1^p - g_1^n)dx = \frac{1}{6}\frac{g_A}{g_V}, \tag{1.1}$$

where $g_1^{p(n)}$ is the spin structure function for the proton (neutron), $\frac{g_A}{g_V}$ is the ratio of axial and vector coupling constants, and the integration is taken over the full range of the kinematic variable x (Eq. 1.8). Because of the surprising EMC proton result, experimenters raced to check this fundamental relation by measuring the neutron. If found, a violation of the Bjorken sum rule would represent a major problem for perturbative quantum chromodynamics (pQCD). With the large amount of data from the polarized scattering experiments listed above, the Bjorken sum rule was verified and the quark contribution towards a nucleon's spin was determined to be 30%$\pm$10% [15].

One condition of the Bjorken sum rule is that it only holds true at high energies. That is, the electron four-momentum transfer to the target nucleon must be large. Interactions at high momentum transfers are governed by perturbative QCD. For the case of the Bjorken sum rule, pQCD corrections are made for the fact that experiments were not conducted at infinite momentum transfer.

At low energies the validity of pQCD comes into question. No longer are interactions strictly between the electron and a constituent quark, as modeled at high energy. More of the nucleon's macroscopic structure is expected to play a role. This structure is complicated by the addition of sea quarks (quark-antiquark pairs) and gluons (carriers of the strong interaction). There is currently no way to predict or calculate accurately the spin structure functions at low energy without directly measuring them. The hope is that someday lattice QCD will be able to derive the nucleon structure functions from first principals.

Experiments in the low energy region can use the Gerasimov-Drell-Hearn (GDH)

sum rule as a lighthouse to study the evolution of the nucleon spin structure functions:

$$\int_{thr}^{\infty}(\sigma_{1/2}-\sigma_{3/2})\frac{d\nu}{\nu}=-\frac{2\pi^2\alpha}{M^2}\kappa^2. \tag{1.2}$$

The GDH sum rule relates the difference in polarized cross sections ($\sigma_{1/2(3/2)}$), for the scattering of real photons, to the target's anomalous magnetic moment (κ), mass (M), and the electro-magnetic coupling constant (α). There is now a large effort to study the nucleon spin structure in the low energy region, much of it focused on testing the GDH sum rule. This thesis focuses on experiment E94-010 conducted at Jefferson Lab in Virginia. The experiment measured the neutron's spin structure functions in both the low and high energy regimes in order to provide data to connect the Bjorken and GDH sum rules. The remainder of this chapter deals with the formalism of polarized electron scattering and describes in detail the GDH and Bjorken sum rules.

1.2 Formalism

The purpose of the E94-010 experiment was to measure the extended Gerasimov-Drell-Hearn sum rule for ^{3}He and the neutron. From the detection of the scattered electrons with different polarization configurations, the polarized ^{3}He cross sections were determined. These were in turn used to calculate the GDH sum rule. The sum rule requires that data be recorded over a wide range of energies. Therefore, E94-010 measured the four principal regions of the cross section: the elastic, quasi-elastic, resonance, and deep inelastic regions (Figure 1.1).

These distinct regions are a consequence of the ^{3}He structure. The virtual photon probes the target and has a wavelength that depends upon its energy. The shorter the wavelength, the greater the resolution of the probe (Figure 1.2). At low energies the ^{3}He appears as one object. Scattering occurs elastically, leaving the ^{3}He nucleus intact. As the energy increases, the constituent nucleons are resolved and scattering can occur elastically from the protons or the neutron. This is called the quasi-elastic

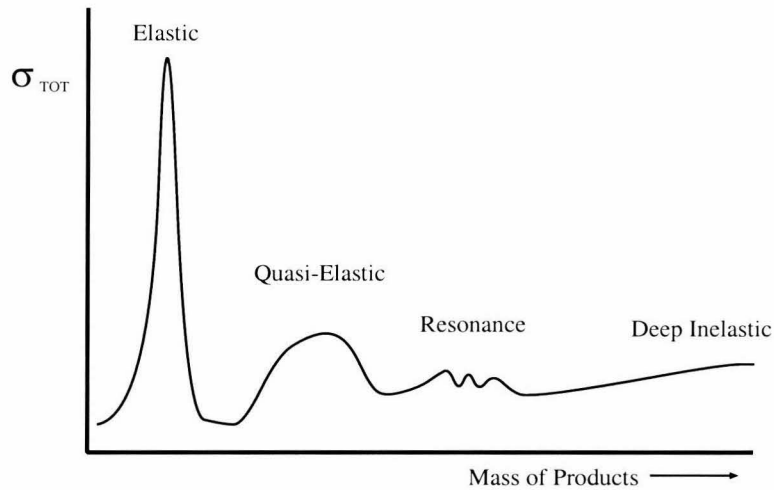

Figure 1.1: Schematic of the ^{3}He cross section. The relative peak heights change depending upon the momentum of the virtual photon.

regime. The cross-sectional peak is smeared due primarily to Fermi motion. Increasing the energy allows for the excitation of the nucleons. There are numerous types of resonances in this region. For example, a proton, having interacted with the scattered electron, becomes a Δ particle which then decays into a pion and a baryon. Finally, when the energy is high enough, the interaction probes the individual quarks. This is known as deep inelastic scattering.

The purpose of this chapter is to introduce the formalism used to describe the extended Gerasimov-Drell-Hearn sum rule. Since E94-010 measures polarized scattering cross sections, particular emphasis is placed on defining the scattering asymmetries and their relation to total cross sections in each region.

There are a number of ways to describe the kinematics of electron scattering by a target. In the experimental hall (lab frame) the three parameters measured are the electron's incident energy, E, the scattered electron's energy, E', and the scattering angle, θ (Figure 1.3). The electron's initial helicity and the target polarization are also known. These three lab variables are related to variables used when considering

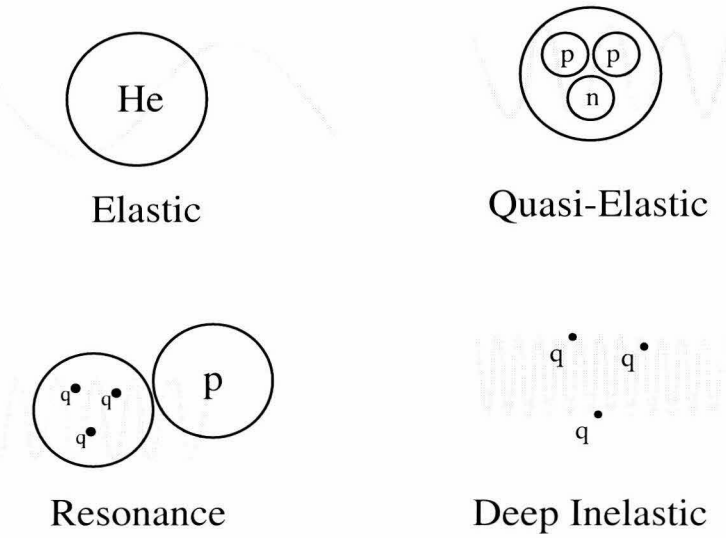

Figure 1.2: The increasing resolution of the ^{3}He nucleus. As the virtual photon energy increases so too does its ability to probe the internal structure of the ^{3}He nucleus and constituent nucleons.

the interaction of the electron and the target.

The interaction between the electron and the target can be described as an electron emitting a virtual photon, which in turn interacts with the target (bottom of Figure 1.3). The electron has an initial four vector k^μ and a final four vector k'^μ. The initial spin of the electron is s^μ and the final spin is not measured in inclusive scattering. For the target, the initial momentum and spin are P^μ and S^μ. The hadronic products have an invariant mass squared given by W^2. The virtual photon has a four vector given by $q^\mu = (\nu, \vec{q})$. Some useful quantities related to the lab frame variables are

$$\nu = E - E', \tag{1.3}$$

$$Q^2 = -q^\mu q_\mu = 4EE' \sin^2 \frac{\theta}{2}, \tag{1.4}$$

$$|\vec{q}| = \sqrt{Q^2 + \nu^2}, \tag{1.5}$$

$$\cos\theta^* = -\frac{E - E'\cos\theta}{|\vec{q}|}, \tag{1.6}$$

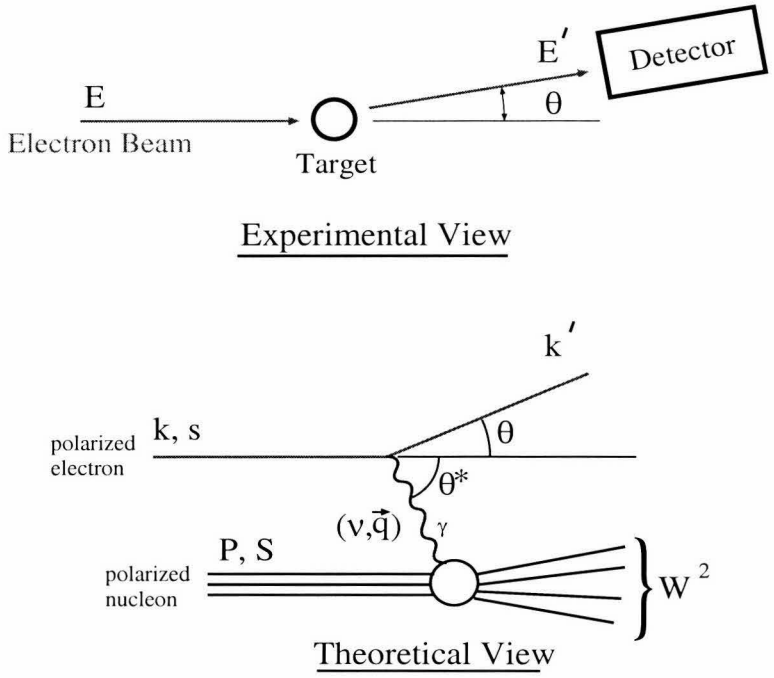

Figure 1.3: The scattering of an electron by a nucleus. The top picture shows scattering in the laboratory frame. The bottom picture depicts how scattering occurs as an exchange of a virtual photon.

$$W^2 = (q^\mu + P^\mu)^2 = M_T^2 + 2M_T\nu - Q^2, \tag{1.7}$$

$$x = \frac{Q^2}{2M_T\nu}, \tag{1.8}$$

$$\tau = \frac{Q^2}{4M_T^2}, \tag{1.9}$$

$$\epsilon = (1 + 2\frac{|\vec{q}|^2}{Q^2}\tan^2\frac{\theta}{2})^{-1}, \tag{1.10}$$

where M_T is the target mass (either the ^{3}He or nucleon mass), $Q^2 > 0$, θ^* is the angle between $\vec{k}$ and $\vec{q}$, x is related to the fractional momentum carried by the struck parton, $\tau > 0$, and ϵ is related to the virtual photon's polarization.

Now that some common variables have been defined, the particular formalism for each region is described.

Elastic Scattering

Following the formalism presented in [16], the differential cross section for elastic scattering ($Q^2 = 2M\nu$) of an electron by a nucleus or nucleon is given by

$$\frac{d\sigma}{d\Omega} = \sigma_M \frac{E'}{E}\left[\left(F_1^2(Q^2) + \tau\kappa^2 F_2^2(Q^2)\right) + 2\tau(F_1(Q^2) + \kappa F_2(Q^2))^2 \tan^2\frac{\theta}{2}\right] \tag{1.11}$$

where κ is the anomalous magnetic moment in Bohr magnetons, F_1 and F_2 are the Dirac and Pauli form factors, and σ_M is the Mott cross section. The Mott cross section describes scattering of an electron from a point-like particle:

$$\sigma_M = \frac{\alpha^2 \cos^2\frac{\theta}{2}}{4E^2 \sin^4\frac{\theta}{2}} \tag{1.12}$$

where $\alpha = \frac{1}{137}$ is the fine structure constant. The Dirac and Pauli form factors are functions that account for our lack of knowledge regarding the photon-hadron vertex. At $Q^2 = 0$ they have the following values for the proton and neutron: $F_1^p(0) = 1$, $F_2^p(0) = 1$, $F_1^n(0) = 0$, and $F_2^n(0) = 1$. Typically, for elastic scattering, a new set of form factors are defined:

$$G_E(Q^2) = F_1(Q^2) - \tau\kappa F_2(Q^2), \tag{1.13}$$

$$G_M(Q^2) = F_1(Q^2) + \kappa F_2(Q^2). \tag{1.14}$$

These are known as the Sachs form factors, and they have a direct physical interpretation. If ν is small compared to the nucleon mass, then G_E is the Fourier transform of the charge density and G_M is related to the magnetization density. At $Q^2 = 0$, $G_E^p = 1$, $G_M^p = \mu_p$, $G_E^n = 0$, and $G_M^n = \mu_n$, where $\mu_p = 2.79$ and $\mu_n = -1.91$ in Bohr magnetons. In terms of the Sachs form factors, the elastic scattering cross section is [17]

$$\frac{d\sigma}{d\Omega} = \sigma_M \frac{E'}{E}\frac{1}{\epsilon(1+\tau)}[\epsilon G_E^2 + \tau G_M^2]. \tag{1.15}$$

Because the target and initial electron spins are known, three polarized cross sections can be measured: the case when the spins are aligned, the case when they are anti-aligned, and the case when the target spin is perpendicular to the electron spin. By measuring the scattering rates for the different combinations, two asymmetries are measured:

$$A_{||} = \frac{d\sigma^{\downarrow\uparrow} - d\sigma^{\uparrow\uparrow}}{d\sigma^{\downarrow\uparrow} - d\sigma^{\uparrow\uparrow}} \qquad \text{and} \qquad A_{\perp} = \frac{d\sigma^{\downarrow\leftarrow} - d\sigma^{\uparrow\leftarrow}}{d\sigma^{\downarrow\leftarrow} - d\sigma^{\uparrow\leftarrow}}. \tag{1.16}$$

The first arrow refers to the beam helicity and the second refers to the direction of the target's polarization. The up and down arrows represent spin directions parallel and anti-parallel to the beam axis. A left arrow means that the spins of the target are perpendicular to the beam momentum direction.

In the case of elastic scattering from ^{3}He these asymmetries are related to the ^{3}He form factors in the following way [18]:

$$A = -\frac{2\tau v_{T'} G_M^2 \cos\psi - 2v_{TL'}\sqrt{2\tau(1+\tau)} G_E G_M \sin\psi}{v_L(1+\tau)G_E^2 + 2v_T \tau G_M^2}, \tag{1.17}$$

where ψ is the angle between the target spin vector and $\vec{q}$. For $A_{||}$, $\psi = \theta^*$. For $A_{\perp}$, $\psi = \theta^* \pm 90°$. The quantities v_X are kinematic variables and are given by:

$$v_{T'} = \tan\frac{\theta}{2}\sqrt{\tan^2\frac{\theta}{2} + \frac{1}{1+\tau}}, \tag{1.18}$$

$$v_{TL'} = -\frac{1}{\sqrt{2}}\frac{1}{1+\tau}\tan\frac{\theta}{2}, \tag{1.19}$$

$$v_L = \left(\frac{1}{1+\tau}\right)^2, \tag{1.20}$$

$$v_T = \tan^2\frac{\theta}{2} + \frac{1}{1+\tau}. \tag{1.21}$$

Measured values for the ^{3}He electric and magnetic form factors can be found in [19][1].

[1] Dunn uses the form factors F_C and F_M which are related to G_E and G_M: $G_E = ZF_C$ and $G_M = \mu_{^3He} F_M$ and $F_C(0) = F_M(0) = 1$.

The size of $A_{||}$ can easily be estimated. For an incident electron energy of 0.86 GeV and a scattering angle of 15.5°, $|A_{||}| \approx 0.02\frac{G_M}{G_E}$. If the assumption is made that the form factors for ^{3}He are just the addition of proton and neutron form factors, then[2]

$$G_E^{He} = G_E^p + G_E^p + G_E^n \overset{Q^2\to 0}{\approx} 1 + 1 + 0 = 2, \tag{1.22}$$

$$G_M^{He} = G_M^p + G_M^p + G_M^n \overset{Q^2\to 0}{\approx} \mu_p - \mu_p + \mu_n = -1.913, \tag{1.23}$$

and $|A_{||}| \approx 2 \times 10^{-2}$ which is correct to within a factor of two.

Quasi-Elastic Scattering

Quasi-elastic scattering is essentially elastic scattering from a nucleus' constituent nucleons. The scattering cross section for a nucleon is given by Eq.(1.11). The quasi-elastic peak is not as sharp as the ^{3}He elastic peak. This is because the nucleons carry a large momentum dispersion due to their confinement in Δx ($\Delta p \Delta x \sim h$). The Fermi motion smears the peak [20]. As for the spin-dependent asymmetry in this region, the contributions from the two proton spins should cancel due to the Pauli exclusion principle. This dilutes the asymmetry contributed by the neutron. Dilution from the fact that the ^{3}He wavefunction is not only in a ground state also occurs, but the contribution to the asymmetry is small [21]. The spread due to Fermi motion also dilutes the asymmetry. Therefore, the measured quasi-elastic asymmetry is expected to be smaller than the elastic asymmetry for ^{3}He.

Resonance Region

When the energy of the virtual photon is large enough to distinguish the constituent quarks of a nucleon, but not large enough to scatter individually off quarks, resonant scattering can occur. In such an interaction the photon excites the nucleon's internal

[2]The magnetic moments of the two protons in ^{3}He should anti-align due to the Pauli Exclusion Principal. That's why the second μ_p has a negative sign.

constituents. Shortly after excitation (10^{-23}s) the excited nucleon decays into a nucleon and a meson (Figure 1.4). The lowest energy resonance is the Δ particle or P_{33} state (the 3's represent the (isospin, J) (3/2,3/2) state). Because of the $\frac{1}{\nu}$ weighting in the GDH integral (Eq. 1.63), this lowest energy resonance is the dominate contribution to the sum rule for the neutron.

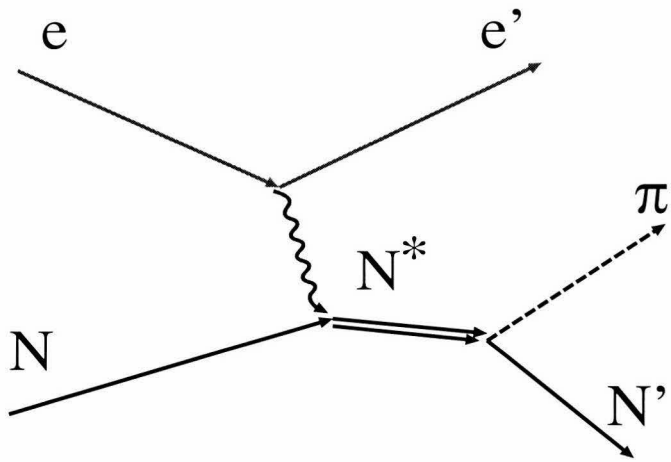

Figure 1.4: Resonance scattering. The virtual photon excites the nucleon (N) into an excited state (N*) which then decays into a nucleon (N') and a meson (π).

Polarized scattering in this regime is characterized by the total photo-absorption cross sections. These cross sections describe the interaction between the virtual photon and the target. The virtual photon can have transverse and longitudinal polarizations. This will yield four photo-absorption cross sections when the target has a spin of 1/2. In terms of |(initial photon projection), (initial target spin projection)> they are:

$$\begin{aligned}
\sigma_{1/2} &\sim |(1,-1),(1/2,1/2)>, \\
\sigma_{3/2} &\sim |(1,1),(1/2,1/2)>, \\
\sigma_{L} &\sim |(1,0),(1/2,1/2)>, \\
\sigma_{TL} &\sim |(1,0),(1/2,1/2)> |(1,-1),(1/2,1/2)> .
\end{aligned}$$

The total transverse photo-absorption cross section is $\sigma_T = \sigma_{1/2} + \sigma_{3/2}$, where $\sigma_{3/2(1/2)}$ is for the case when the photon and target spins are aligned(anti-aligned). The difference in these cross sections is $\sigma_{TT} = \sigma_{1/2} - \sigma_{3/2}$. The total longitudinal cross section is σ_L. There is also an interference term between the transverse and longitudinal interactions given by σ_{TL}.

Two virtual photon asymmetries can be formed from these cross sections:

$$A_1 = \frac{\sigma_{1/2} - \sigma_{3/2}}{\sigma_T} \quad \text{and} \quad A_2 = \frac{\sigma_{LT}}{\sigma_T}. \tag{1.24}$$

The boundary on their values are [22]

$$-1 \leq A_1 \leq 1 \quad \text{and} \quad A_2 \leq \sqrt{\frac{\sigma_L}{\sigma_T}}. \tag{1.25}$$

The asymmetries A_1 and A_2 are related to $A_{||}$ and $A_\perp$ [23]:

$$A_{||} = D(A_1 + \eta A_2) \quad \text{and} \quad A_\perp = d(A_2 - \zeta A_1), \tag{1.26}$$

where

$$D = \frac{1 - E'\epsilon/E}{1 + \epsilon R}, \tag{1.27}$$

$$\eta = \epsilon \frac{\sqrt{Q^2}}{E - E'\epsilon}, \tag{1.28}$$

$$d = D\sqrt{\frac{2\epsilon}{1+\epsilon}}, \tag{1.29}$$

$$\zeta = \frac{\eta(1+\epsilon)}{2\epsilon}, \tag{1.30}$$

$$R = \frac{\sigma_L}{\sigma_T}. \tag{1.31}$$

If the incoming electron transfers all its energy, $D = 1$ and $d = 0$ and therefore $A_{||} = A_1$.

The P_{33} resonance, or Δ particle, is a proton (neutron) with both up (down) quark

spins pointing in the same direction and with a total angular momentum of $L_z = 0$ for all three quarks. The P_{33} asymmetry can be predicted by examining the following transitions:

$$|u(\uparrow)u(\downarrow)d>_p \rightarrow |u(\uparrow)u(\uparrow)d>_\Delta \qquad \text{or} \qquad |d(\uparrow)d(\downarrow)u>_n \rightarrow |d(\uparrow)d(\uparrow)u>_\Delta . \tag{1.32}$$

Relating these transitions to their Clebsch-Gordan coefficients, the ratio $\sigma_{1/2}/\sigma_{3/2} = \frac{1}{3}$, and therefore $A_1 = -\frac{1}{2}$, which is in good agreement with the data [24].

The double polarized differential cross section in terms of the virtual photon asymmetries and photo-absorption cross sections is [25]

$$\frac{d^2\sigma}{d\Omega dE'} = \Gamma_T(\sigma_T + \epsilon\sigma_L \pm \sqrt{1-\epsilon^2}\cos\psi\sigma_T A_1 \pm \sqrt{2\epsilon(1-\epsilon^2)}\sin\psi\sigma_T A_2), \tag{1.33}$$

where Γ_T is the virtual photon flux:

$$\Gamma_T = \frac{\alpha}{4\pi Q^2}\frac{(W^2-M^2)E'}{ME}\frac{1}{1-\epsilon}. \tag{1.34}$$

The unpolarized portion of the differential cross section $(\sigma_T + \epsilon\sigma_L)$ can be approximated by σ_T since the ratio σ_L/σ_T is fairly small in the P_{33} resonance region. This, in turn, is broken down into resonant and non-resonant contributions:

$$\sigma_T + \epsilon\sigma_L \approx \sigma_T = \sigma_R + \sigma_{NR}. \tag{1.35}$$

The non-resonant background is generally parameterized by a polynomial [25]:

$$\sigma_{NR} = \sqrt{W - W_{thr}}\sum_{i=0}^{m} a_i(W - W_{thr})^i, \tag{1.36}$$

where a_i are free parameters fit to the data and W_{thr} is the value of $\sqrt{W^2}$ at the threshold of Δ production. The resonant cross section for P_{33} can be expressed in terms of electric and magnetic form factors for the Δ and the total width of the

resonance, Γ:

$$\sigma_R(P_{33}) = \frac{4\pi\alpha}{\Gamma}\frac{|\vec{q}|^2}{W(W^2-M^2)}(|G_M^\Delta|^2 + 3|G_E^\Delta|^2). \tag{1.37}$$

The cross section for P_{33} is strongly excited at Q^2 near zero, and G_M^Δ, the dominate form factor, falls off rapidly with increasing Q^2 [1]. This implies that the GDH sum rule will have a strong Q^2 dependence at low Q^2 (Figure 1.5).

Deep Inelastic Scattering

The scattering of electrons in the deep inelastic region is described by the contraction of two tensors. The electron virtual photon vertex is described by the lepton tensor $L_{\mu\nu}$ and the nucleon virtual photon vertex is described by the hadron tensor $W^{\mu\nu}$. Each is comprised of a spin-independent part and a spin-dependent part. The differential cross section is given by [20]:

$$\frac{d^2\sigma}{d\Omega dE'} = \frac{4\alpha^2}{Q^4}\frac{E'}{E}L_{\mu\nu}W^{\mu\nu}. \tag{1.38}$$

Following the form of Hughes and Kuti [22], the lepton tensor, when the final spin state of the scattered electron is summed over, is given by

$$L_{\mu\nu} = \underbrace{k'_\mu k_\nu + k'_\nu k_\mu - g_{\mu\nu}k'\cdot k}_{spin-independent} + \underbrace{im_e\varepsilon_{\mu\nu\alpha\beta}s^\alpha q^\beta}_{spin-dependent}, \tag{1.39}$$

where $\varepsilon_{\mu\nu\alpha\beta}$=1 for even permutations of 1234, $g_{\mu\nu}$ is the metric tensor, and m_e is the mass of the electron. The hadron tensor is represented by

$$W^{\mu\nu} = W^{\mu\nu}_{(S)} + W^{\mu\nu}_{(A)}, \tag{1.40}$$

where

$$W^{\mu\nu}_{(S)} = \left(-g^{\mu\nu} + \frac{q^\mu q^\nu}{q^2}\right)W_1 + \frac{1}{M^2}\left(P^\mu - \frac{P\cdot q}{q^2}q^\mu\right)\left(P^\nu - \frac{P\cdot q}{q^2}q^\nu\right)W_2 \tag{1.41}$$

and

$$W^{\mu\nu}_{(A)} = iM\varepsilon^{\mu\nu\alpha\beta}q_\alpha S_\beta G_1 + \frac{i}{M}\varepsilon^{\mu\nu\alpha\beta}q_\alpha[(P\cdot q)S_\beta - (S\cdot q)P_\beta]G_2. \tag{1.42}$$

Here, four new parameters have been introduced: W_1, W_2, G_1, and G_2. They are the inelastic structure functions, and they represent the interaction between the virtual photon and the nucleon. The first two, W_1 and W_2, characterize unpolarized scattering, and G_1 and G_2 are relevant for polarized scattering. All four of the structure functions depend on ν and Q^2 (not simply Q^2 as in the case of elastic scattering).

For unpolarized scattering, the inclusive cross section, when the final electron spin state is averaged over, is given by

$$\frac{d^2\sigma}{d\Omega dE'} = \frac{4\alpha^2 E'^2}{Q^4}\left(\cos^2\frac{\theta}{2}W_2 + 2\sin^2\frac{\theta}{2}W_1\right). \tag{1.43}$$

Polarized scattering is characterized by measuring the asymmetries A_1 and A_2. The virtual photon cross sections have the following relations to the structure functions [20, 23]:

$$\sigma_{3/2} \sim \quad < 1, 1/2|1, 1/2 > \quad = W_1 + \nu M G_1 - Q^2 G_2, \tag{1.44}$$

$$\sigma_{1/2} \sim \quad < 1, -1/2|1, -1/2 > \quad = W_1 - \nu M G_1 + Q^2 G_2, \tag{1.45}$$

$$\sigma_L \sim \quad < 0, 1/2|0, 1/2 > \quad = (1 + \frac{\nu^2}{Q^2})W_2 - W_1, \tag{1.46}$$

$$\sigma_{TL} \sim \quad < 1, 1/2|0, 1/2 > \quad = \sqrt{Q^2}(M G_1 + \nu G_2). \tag{1.47}$$

When the scattering energies are sufficiently high (Q^2 large) the structure functions become dependent upon only one variable: x. This behavior is known as scaling, and it arises from the fact that the nucleon is comprised of point-like particles. The relationship between the general structure functions and those used when the scattering is in this regime are given by

$$\frac{1}{M^2}W_1(\nu, Q^2) = F_1(x), \qquad \frac{\nu}{M^3}W_2(\nu, Q^2) = F_2(x), \tag{1.48}$$

$$\frac{\nu}{M}G_1(\nu,Q^2) = g_1(x), \quad \text{and} \quad \frac{\nu^2}{M^2}G_2(\nu,Q^2) = g_2(x). \tag{1.49}$$

Furthermore, F_1 and F_2 are related to one another by a modification of the Callan-Gross relationship:

$$F_1(x) = F_2(x)\frac{1+\frac{Q^2}{\nu^2}}{2x(1+R)}. \tag{1.50}$$

The confirmation of this relationship indicates that the quarks have a spin of 1/2. As $Q^2 \to \infty$ for constant x, $R \to 0$, and $F_2 = 2xF_1$. The relation between the structure functions and the virtual photon asymmetries are given by

$$g_1 = \frac{F_1}{\left(1+\frac{Q^2}{\nu^2}\right)}\left(A_1 + \sqrt{\frac{Q^2}{\nu^2}}A_2\right) \quad \text{and} \quad g_2 = \frac{F_1}{\left(1+\frac{Q^2}{\nu^2}\right)}\left(\sqrt{\frac{\nu^2}{Q^2}}A_2 - A_1\right). \tag{1.51}$$

At high energies, the spin structure functions have a simple physical interpretation in the quark-parton model [22]. For F_1 and g_1, the interpretation is that they are equal to the sum over longitudinally polarized quark types:

$$F_1(x) = \frac{1}{2}\sum_i e_i^2[f_i^{\uparrow}(x) + f_i^{\downarrow}(x)], \tag{1.52}$$

$$g_1(x) = \frac{1}{2}\sum_i e_i^2[f_i^{\uparrow}(x) - f_i^{\downarrow}(x)], \tag{1.53}$$

where $f_i^{\uparrow(\downarrow)}(x)$ is the probability of finding a quark with its spin aligned (anti-aligned) with the nucleon's spin and with a fraction x of the nucleon's total momentum. The charge of the quark type is given by e_i.

1.3 Sum Rules

Theoretical knowledge of the spin structure functions is limited to integrals over some kinematic region (e.g., $\int_0^1 g_1(x)dx$). These types of integrals, or combinations thereof, are known as sum rules. Measurement of these sum rules allow for tests of their assumptions. Some of these sum rule studies represent fundamental tests of QCD.

1.3.1 Bjorken Sum Rule

In 1966 Bjorken [26] derived a sum rule using current algebra in the limit of $Q^2 \to \infty$ (Eq. 1.61). Integrating Eq. 1.53 over the full range of x gives, what is called, the first moment:

$$\Gamma_1 = \int_0^1 g_1(x)dx = \frac{1}{2}\left(\frac{4}{9}\Delta u + \frac{1}{9} + \Delta d\frac{1}{9}\Delta s\right). \tag{1.54}$$

The quantities Δq are the helicity carried by each quark type. They can be calculated from the following matrix element:

$$2\Delta q s^\mu =< N|\overline{q}\gamma^\mu\gamma^5 q|N >, \tag{1.55}$$

where N represents the nucleon, γ^μ and γ^5 are the Dirac matrices. The Bjorken sum rule relates the first moment to the weak current matrix element for neutron decay:

$$< \bar{p}|J_w|n >=< \bar{p}|\tau^+\gamma^\mu(1-\gamma^5)|n >= \bar{U}\gamma^\mu\left(1 - \frac{g_A}{g_V}\right)U = 2\left(p^\mu - \frac{g_A}{g_V}s^\mu\right), \tag{1.56}$$

where U represents a Dirac spinor and τ is a Pauli matrix for isospin. Equation 1.56 can be converted to a matrix element between proton states:

$$< \overline{p}|\tau^+\gamma^\mu\gamma^5|n >=< \overline{p}|\tau^3\gamma^\mu\gamma^5|p > . \tag{1.57}$$

This, in turn, is related to the helicity carried by the quarks:

$$< \overline{p}|\tau^3\gamma^\mu\gamma^5|p >=< \overline{p}|\overline{u}\gamma^\mu\gamma^5 u - \overline{d}\gamma^\mu\gamma^5 d|p >= 2s^\mu(\Delta u_p - \Delta d_p). \tag{1.58}$$

Now, a portion of the matrix element in Eq. 1.56 is related to the quark helicities in Eq. 1.58:

$$< \overline{p}|\tau^+\gamma^\mu\gamma^5|n >= 2s^\mu\frac{g_A}{g_V} = 2s^\mu(\Delta u_p - \Delta d_p) \tag{1.59}$$

and the Bjorken sum rule is realized:

$$\Gamma_1^p - \Gamma_1^n = \frac{1}{6}(\Delta u_p - \Delta d_p) = \frac{1}{6}\frac{g_A}{g_V}. \tag{1.60}$$

At finite Q^2, gluon interactions modify the sum rule. The modification is calculated using pQCD and amounts to a correction by a power series in $\alpha_s(Q^2)$:

$$\int_0^1 (g_1^p(x) - g_1^n(x))dx = \frac{1}{6}\frac{g_A}{g_V}\left(1 - \frac{\alpha_s(Q^2)}{\pi}\right). \tag{1.61}$$

The strong coupling constant, $\alpha_s(Q^2)$, has the following form

$$\alpha_s(Q^2) = \frac{1}{\left(\frac{33-2f}{12\pi}\right)\ln Q^2/\Lambda^2}, \tag{1.62}$$

where f is the number of quark flavors, and Λ ($\sim$100 MeV) characterizes the strength of the strong coupling constant. Today the Bjorken sum rule corrections have been calculated up to third order in α_s [27].

1.3.2 Gerasimov-Drell-Hearn Sum Rule

In 1966, S.B. Gerasimov [28] and, independently, S.D. Drell and A.C. Hearn [29] derived a sum rule for the absorption of polarized real photons on a polarized nucleon. The sum rule takes the photon energy weighted difference of two spin dependent cross sections and relates it to the nucleon's anomalous magnetic moment:

$$\int_{thr}^{\infty} \frac{\sigma_{1/2} - \sigma_{3/2}}{\nu} d\nu = -\frac{2\pi^2\alpha}{M^2}\kappa^2. \tag{1.63}$$

Here, $\sigma_{3/2(1/2)}$ is the absorption cross section when the photon and nucleon spins are aligned (anti-aligned), ν is the photon energy, κ is the anomalous magnetic moment, α is the electromagnetic coupling constant, and M is the mass of the nucleon. The integration is carried out from the pion threshold ($\frac{Q^2+2m_\pi M+m_\pi^2}{2M}$) to infinity.

Derivation of the sum rule starts by using the results of Gell-Mann, Goldberger, and Thirring [30] for the forward scattering of photons. They derived the Compton scattering amplitude for a photon scattering at zero degrees:

$$f(\nu) = f_1(\nu)\vec{\epsilon}'^* \cdot \vec{\epsilon} + f_2(\nu) i\vec{\sigma} \cdot \vec{\epsilon}'^* \times \vec{\epsilon}. \tag{1.64}$$

Here $\vec{\epsilon}'^*$ and $\vec{\epsilon}$ are the final and incident photon polarization vectors, ν is the photon energy, and $\vec{\sigma}$ is the target spinor. The functions $f_1(\nu)$ and $f_2(\nu)$ are scalar invariants. The optical theorem relates the imaginary parts of $f_1(\nu)$ and $f_2(\nu)$ to the polarized cross sections $\sigma_{3/2}$ and $\sigma_{1/2}$:

$$\mathrm{Im}f_1(\nu) = \frac{\nu}{4\pi}\frac{\sigma_{3/2} + \sigma_{1/2}}{2} \quad \text{and} \quad \mathrm{Im}f_2(\nu) = \frac{\nu}{4\pi}\frac{\sigma_{3/2} - \sigma_{1/2}}{2}. \tag{1.65}$$

For the GDH sum rule, the interest is in the real part of $f_2(\nu)$. This real part can be related to the imaginary part using a non-subtractive dispersion relation [31]:

$$\mathrm{Re}f_2(\nu) = \frac{2}{\pi}\int_{thr}^{\infty} \frac{\nu' \mathrm{Im}f_2(\nu')}{\nu'^2 - \nu^2} d\nu'. \tag{1.66}$$

By differentiating with respect to ν and then letting $\nu \to 0$, Eq. 1.66 becomes

$$f_2'(0) = \frac{2}{\pi}\int_{thr}^{\infty} \frac{\mathrm{Im}f_2(\nu)}{\nu^2} d\nu. \tag{1.67}$$

In the same year, 1954, as Gell-Mann, Goldberger, and Thirring published their results for forward Compton scattering, F.E. Low [32] and Gell-Mann and Goldberger [33] derived a result for the scattering of low energy light by a system of spin $\frac{1}{2}$ particles. For the case of forward scattering in the low energy limit, they found that the derivative of the scattering amplitude was related to the anomalous magnetic moment:

$$f_2'(0) = \frac{\alpha}{2M^2}\kappa^2. \tag{1.68}$$

The Gerasimov-Drell-Hearn (GDH) sum is completed by taking Eqs. 1.68 and 1.65 and substituting them into Eq. 1.67.

Extended GDH Sum Rule

The GDH sum is only valid for real photons ($Q^2 = 0$). In the case of electron scattering we have virtual photons ($Q^2 \neq 0$). While there is no sum rule for virtual photons, we can construct a related integral by considering the difference of polarized cross sections:

$$\sigma_{TT} = \sigma_{1/2} - \sigma_{3/2} = \frac{8\pi^2\alpha}{M^3(\nu - Q^2/2M)}(M\nu G_1(\nu, Q^2) - Q^2 G_2(\nu, Q^2)). \tag{1.69}$$

The integral [34]

$$I(Q^2) = -\int_{thr}^{\infty} \frac{d\nu}{\nu}(\sigma_{1/2} - \sigma_{3/2}) \tag{1.70}$$

converges to the GDH sum rule result as $Q^2 \to 0$:

$$I(0) = -\frac{2\pi^2\alpha}{M^2}\kappa^2, \tag{1.71}$$

which is equal to $-204\mu b$ for protons, $-232.8\mu b$ for neutrons, and $-496\mu b$ for ^{3}He. For a ^{3}He GDH sum rule, integration begins just above the elastic peak and goes to infinity. For a neutron GDH sum rule, integration is from the pion threshold to infinity. The extent to which a polarized ^{3}He can be modeled as a polarized neutron and two unpolarized protons can be tested by integrating $\sigma_{TT'}$ for ^{3}He over the neutron range:

$$\underbrace{\int_{\nu>elastic}^{\infty} \frac{\sigma_{TT}^{^3He}(\nu, Q^2 = 0)}{\nu} d\nu}_{-496\mu b} = \underbrace{\int_{\nu>elastic}^{\nu=pion} \frac{\sigma_{TT}^{^3He}(\nu, Q^2 = 0)}{\nu} d\nu}_{-263.2\mu b} + \underbrace{\int_{\nu>pion}^{\infty} \frac{\sigma_{TT}^{^3He}(\nu, Q^2 = 0)}{\nu} d\nu}_{-232.8\mu b(\text{free neutron})} \tag{1.72}$$

1.3.3 Motivation for Measurement of Nucleon Spin Structure for Intermediate and Low Values of Q^2

The early motivation to study the spin structure functions in the low Q^2 regime was to study in more detail the 'proton spin crisis'. Anselmino and others [35] proposed that higher twist effects could alter the value of the Bjorken sum rule for finite Q^2 beyond pQCD corrections (Eq. 1.61). The size of the effect could be estimated using the GDH sum rule. By doing this, they found that the quark contribution to the Bjorken sum rule could be as high as 50%. Not only did the GDH sum rule bring the quark contribution up to something "reasonable", but it also suggested dramatic spin structure at intermediate values of Q^2 ($.02 \leftrightarrow 1$ GeV^2). With measurements taken after EMC, the Bjorken sum rule for finite Q^2 is entirely accounted for using pQCD corrections implying that higher twist effects are small. However, dramatic spin structure effects at low energy are still possible.

Polarized data in this region ($Q^2 < 1$) is nonexistent. For the extended GDH sum rule, unpolarized data in the resonance region has been used to try and understand its Q^2 evolution. Because of the $1/\nu$ weighting, the largest contribution to the neutron is expected to come from the P_{33} resonance (Figure 1.5).

Current interest in the intermediate region has been spurred on by the development of a generalized GDH sum rule proposed by Ji and Osborne [36]. This sum rule relates the spin structure function $G_1(\nu, Q^2)$ to the forward virtual Compton scattering amplitude $S_1(\nu, Q^2)$:

$$4\int_{el}^{\infty} \frac{G_1(\nu, Q^2)}{\nu} d\nu = S_1(0, Q^2). \tag{1.73}$$

At $Q^2 = 0$, Eq. 1.73 is related to the GDH sum rule:

$$S_1(\nu, 0) \xrightarrow{\nu \to 0} -\frac{\kappa^2}{M^2}. \tag{1.74}$$

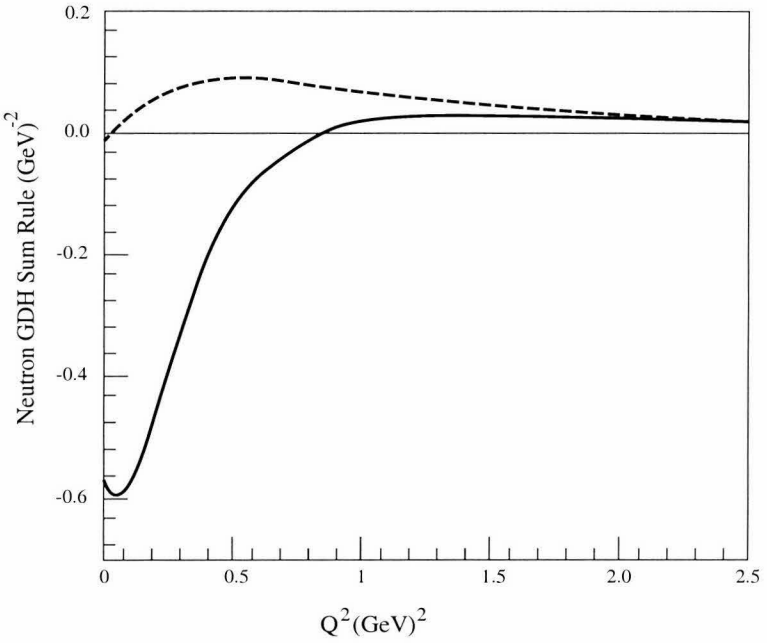

Figure 1.5: The extended GDH sum rule as presented in [1]. The solid line is the integral $I^n(Q^2)$ with the P_{33} resonance. The long-dashed line is without the P_{33} contribution.

For $Q^2 \to \infty$, Eq. 1.73 is connected to the Bjorken sum rule by the use of the dispersion relation for $S_1(\nu, Q^2)$:

$$S_1^{(p)}(0, Q^2) - S_1^{(n)}(0, Q^2) = \frac{4}{3Q^2}\frac{g_A}{g_V}. \tag{1.75}$$

The forward virtual Compton Scattering amplitude can be extended from $Q^2 = 0$ using chiral perturbation theory and from $Q^2 \to \infty$ using Operator Product Expansion. These theoretical predictions can be tested against the measured value of $G_1(\nu, Q^2)$.

Experiment E94-010 marked the first time the spin structure functions will have been measured for ^{3}He and the neutron in the low and intermediate energy regimes.

Chapter 2 Experimental Setup

2.1 Overview

Jefferson Lab is located approximately twenty miles up the James River in Newport News, Virginia. The facility consists of, among other things, an electron accelerator and three experimental halls, which are ingeniously named A, B, and C. Hall A contains two high resolution spectrometers used to detect particles scattered by a fixed target. Electrons can be delivered to all three halls simultaneously. They are initially accelerated to 45 MeV at the injector site (Figure 2.1). From there they pass through a linac where they acquire another 400 MeV. Next, they travel through a 180° turn in the recirculation arc and accelerate an additional 400 MeV as they pass down a second linac. The electrons can now be delivered to any or all of the experimental halls, or they can enter a recirculation arc that returns them to the first linac. If returned, the electrons pick up an additional 800 MeV before going to a Hall or transported for another pass. Up to five passes are allowed for a maximum electron energy of nearly 6 GeV. The 400 MeV acceleration for each linac section is a nominal amount. It can be adjusted to deliver a variety of energies.

Experiment E94-010 (*Measurement of the Neutron (3He) Spin Structure Function at Low Q^2 : a connection between the Bjorken and Drell Hearn Gerasimov sum rules.*) was conducted in Hall A. It used beam energies of 0.860, 1.720, 2.591, 3.384, 4.255, and 5.070 GeV at currents ranging from 3μA to 15μA. The electrons were longitudially polarized, and their helicity was flipped at a rate of 30 Hz. The fixed target was a 40 centimeter long glass tube filled to 10 atmospheres of polarized ^{3}He. The two spectrometers were configured with detector packages designed to detect scattered electrons. The experiment ran from September 25 through Christmas Eve of 1998

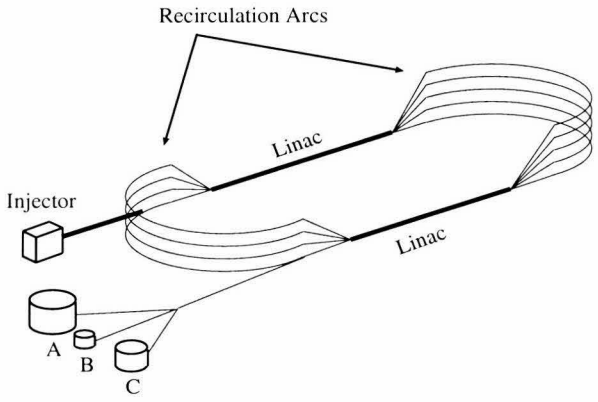

Figure 2.1: Accelerator configuration.

and recorded approximately five and a half billion scattered electron events.

2.2 Polarized Electron Beam

2.2.1 Beam Source

Jefferson Lab's source of polarized electrons is based upon the source used at SLAC [37]. It utilizes a strained GaAs cathode to create highly polarized electrons. The cathode is created by growing layers of various GaAs combinations (Figure 2.2). The top-most layer is pure GaAs. The layer below it is made of $GaAs_{0.72}P_{0.28}$. The shorter lattice spacing of the $GaAs_{0.72}P_{0.28}$ (5.5968 Å) causes the natural spacing of the GaAs (5.6533 Å) to shrink slightly, creating strain [38]. The stain creates a gap in the different sub-levels of the $P_{3/2}$ electrons in the valence band of the GaAs. By tuning a circularly polarized laser to the proper frequency, electrons from the $P_{3/2}$ m= 3/2 state can be excited to the $S_{1/2}$ m= 1/2 level of the conduction band (Figure 2.2). From there the polarized electrons diffuse to the surface and escape into the surrounding vacuum. Because the strain creates a sufficiently wide gap between the $P_{3/2}$ sublevels, electrons from the m=1/2 state will not be excited by the tuned laser. The consequence is the electrons leaving the surface of the cathode are nearly 100% polarized.

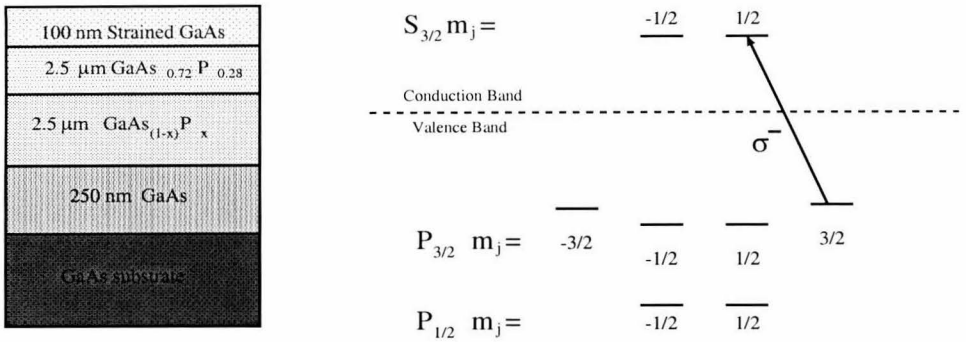

Figure 2.2: The layers of the strained GaAs cathode and the level diagram of the conduction and valence bands.

2.2.2 Møller Polarimeter

Precision measurements of the electron beam polarization were conducted using the Hall A Møller polarimeter [39]. The name "Møller" refers to the scattering of two electrons. For our case, the scattering process was polarized, namely $\vec{e} + \vec{e} \rightarrow e + e$. The scattering cross section depends on the angle at which the two electrons scatter and the polarizations of the beam and target electrons:

$$\sigma \propto 1 + \sum_{i=x,y,z} (A_{ii}(\theta_{CM}) \cdot P_{targ\ i} \cdot P_{beam\ i}), \tag{2.1}$$

where $i = x, y, z$ refer to the the projections of the polarizations, θ_{CM} is the center of mass scattering angle, and $P_{targ(beam)}$ is the polarization of the target (electron beam). If the beam is taken to travel along the z direction and the scattering occurs in the xz-plane, then A_{ii} takes the following form:

$$A_{zz} = -\frac{\sin^2\theta_{CM} \cdot (7 + \cos^2\theta_{CM})}{(3 + \cos^2\theta_{CM})^2}, \tag{2.2}$$

$$A_{xx} = -\frac{\sin^4\theta_{CM}}{(3 + \cos^2\theta_{CM})^2}, \tag{2.3}$$

$$A_{yy} = -A_{xx} \tag{2.4}$$

Measurement of the longitudinal component of the electron beam polarization depends on A_{zz}, which has a maximum value of 7/9 for a center of mass scattering angle of 90°. By measuring the number of electrons scattered when the beam is polarized parallel and anti-parallel to its momentum direction, the following asymmetry is formed::

$$A = \frac{N^{\uparrow\downarrow} - N^{\uparrow\uparrow}}{N^{\uparrow\downarrow} + N^{\uparrow\uparrow}} = A_{zz} \cdot P_{targ\ i} \cdot P_{beam\ i}, \tag{2.5}$$

where $N^{\uparrow\downarrow(\uparrow\uparrow)}$ are the counting rates of the scattered electrons when the beam polarization is anti-parallel (parallel) to the target's spin direction. The transverse components, A_{xx} and A_{yy}, can yield a small asymmetry if the target electrons have a spin component in the yz-plane. However, for a center of mass scattering angle of 90°, the value of A_{xx} is 1/9, so this effect is somewhat suppressed.

The Møller polarimeter for Hall A used a 12 μm thick supermendur foil (Fe plated onto a Cu foil) for its target. Due to boundary conditions, the foil is polarized along its length [40]. It was tilted at angles ranging from 20 to 160° with respect to the beam, making the effective target polarization $P_{targ\ z} = P_{foil} \cdot \cos\theta_{target}$. The angle was determined visually by looking at the target with respect to an engraved scale on the target holder and by comparing the counting rates at different angles. The foil was magnetically saturated using two Helmholtz coils, which produce a magnetic field of about 300 G along the beam at the target center. Out of 26 electrons, 2 per atom are polarized in the iron, translating into a polarization of P_{foil}=7.6%.

The Møller spectrometer is comprised of three quadrupole magnets and one dipole magnet followed by two detectors consisting of scintillators and lead glass counters (Figure 2.3). The two spectrometers were set to record events occurring in coincidence with one another. The angular acceptance of the spectrometers ranges from 76° to 104° in the center of mass frame. For incident energies less than 1 GeV the angular acceptance is between 83° and 97°. Taking into account these acceptances, the average value of $< A_{zz} >$ was 0.759 as determined by a Monte-Carlo simulation.

Twenty-six Møller measurements were taken during the E94-010 experiment. Mea-

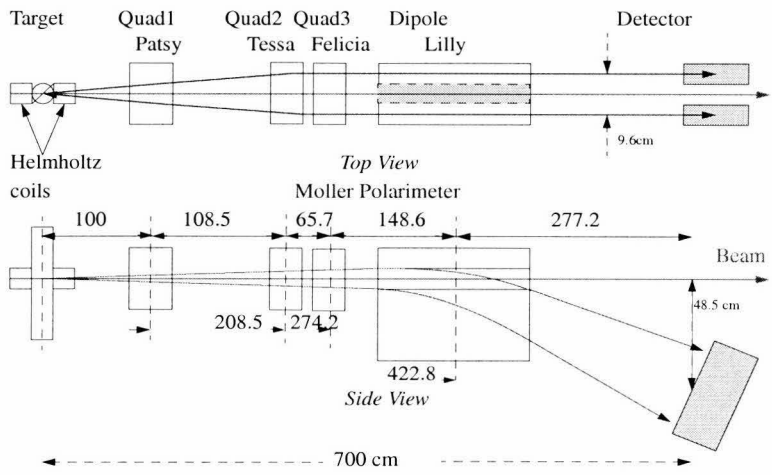

Figure 2.3: Schematic of the Hall A Møller polarimeter.

surements were taken with the target angle at 25 and 155° in order to understand effects due to transverse polarization within the foil and to study the target angle by comparing the counting rates. Several runs of ∼30k events were taken at each angle. The background and Møller peak were fitted to obtain $N^{\uparrow\uparrow(\uparrow\downarrow)}$. The fit took into account the Levchuk effect [41]. This effect is due to the fact that the unpolarized Fe atom electrons are contained in the inner atomic shells. They have a higher momentum and momentum spread and therefore broaden the elastic peak compared to the polarized (outer shell) electrons. This systematic effect was taken into account by correcting the apparent beam polarization down by 2% relative. The results with statistical error bars are shown in Figure 2.4. Also given are the polarization results used for each beam energy.

The systematic uncertainties are listed in Table 2.1. Polarization of the target is given by $P_{target} = P_{foil} \cdot \cos\theta_{foil}$. The angle θ_{foil} is known to $\pm 0.4°$ which contributes

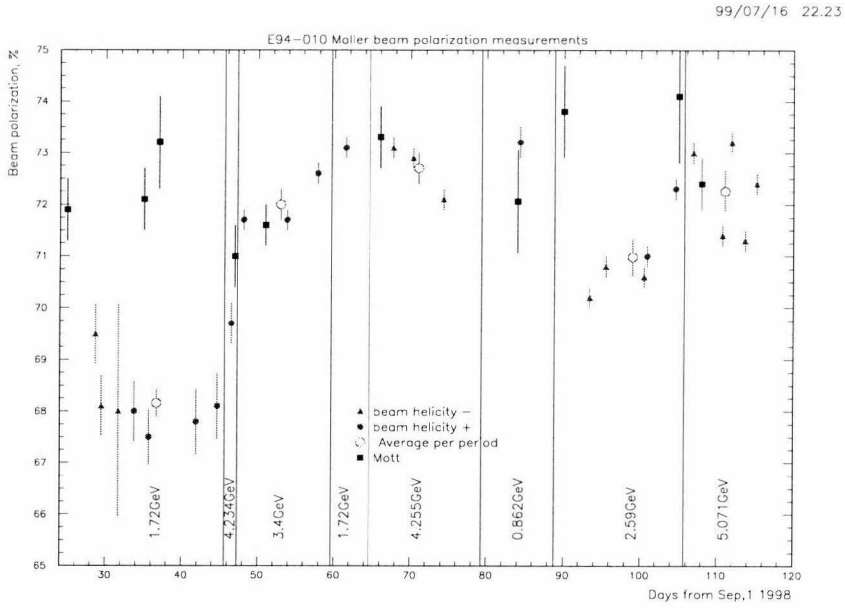

Figure 2.4: Results of the Mott and Møller measurements.

0.3% to the uncertainty of P_{target}. The polarization of the target foil is given by

$$P_{foil} = B_{foil} \frac{g' - 1}{2\pi g'} \frac{1}{N_e \mu_e}, \tag{2.6}$$

where g' is a spin-orbital correction for supermendur and is equal to 1.900±0.005 [39] (this uncertainty contributes negligibly to the uncertainty in P_{foil}), N_e is the number of electrons per unit volume, and B_{foil} is the field within the foil. B_{foil} is given by $\Phi \cdot \text{width} \cdot \text{thickness}$, where Φ is the applied magnetic flux and was determined by varying the external field and measuring the induced EMF in a coil wound around the foil. From systematic studies, maximum deviations in Φ of ±1.5% were observed. The foil thickness is uniform to within ±1.0%. Taking this and the flux into account, a ±2.0% uncertainty is placed on P_{foil}. Background counts make up about 50% of the data but contribute an uncertainty of less than 1% after subtraction. The deadtime

Source	**Uncertainty** [%]
$< A_{zz} >$	0.3
P_{foil}	2.0
θ_{foil}	0.5
Background	<1
Deadtime	<2
Transverse Polarization	0.2
Other fluctuations	1.0
Total	**3.2**

Table 2.1: Systematic uncertainties on P_{beam}.

correction contributed an uncertainty of ~2%. Having taken data at two complementary angles, the uncertainty in the observed asymmetry due to transverse components of polarization was extracted and found to be ±0.2%. The total uncertainty from the beam polarization is taken to be $\pm 0.5\%_{stat} \pm 3.2\%_{syst}$.

2.2.3 Beam Current Monitors

The accumulated electron beam charge that the target sees was recorded using two Beam Current Monitors (BCMs). A BCM is a resonance cavity tuned to the frequency of the electron beam: 1497 MHz. When the beam passes through the cavity it excites the TM_{010} mode. A large wire loop inside the cavity detects the changing magnetic field (Figure 2.5). The amplitude 1497 MHz signal produced by this loop is proportional to the beam's current.

The BCM signal was recorded in two ways. The first method converts the output amplitude into a DC voltage proportional to the original amplitude. This voltage is recorded every 4, 10, and 50 seconds by a VME crate. The second method converts the DC voltage signal into a sine wave whose frequency is proportional to the DC voltage. This sine wave is continuously recorded by a scaler counter.

Calibration of the BCMs was conducted in two ways. Relative changes were measured by using a second excitation loop located within the BCM. A current source

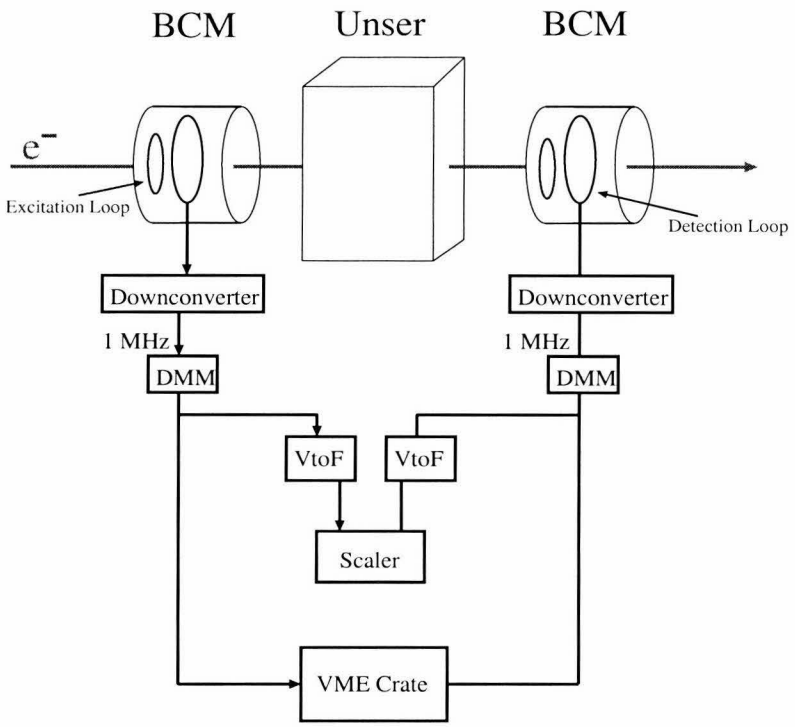

Figure 2.5: Schematic of the beam monitoring device.

sends a 1497 MHz signal into the excitation loop. By measuring the response of the detection loop, relative changes were recorded. Absolute calibration is conducted using an Unser device [42]. The device sits between two BCMs, see Figure 2.5, and uses two identical toroidal cores. Opposite currents are passed trough the cores by an external modulation source. A common sensing wire that is wound around both coils detects a zero voltage when there is no beam current passing through the center of the toroids. However, when a DC current is present it creates an asymmetry in the amount of flux within the cores, and a signal can then be recorded with a common sensing wire. By using a wire that is located along the beam path and a high-precision current source, the electron beam can be simulated, and the Unser calibrated. Once the Unser is calibrated the beam is turned on and the BCMs are calibrated using the Unser. Using this method a calibration value was calculated to convert the scaler

response of the BCMs to the amount of charge incident upon the target. This number had an uncertainty on the order of $\pm 1\%$ coming primarily from the non-linearity in the BCM response.

2.2.4 Beam Position Monitors

The beam position at the target was monitored using Hall A's beam position monitors (BPMs). They consisted of four antennae situated around the beam in a diamond pattern. The antennae pick up the signal from the fundamental frequency of the beam (1497 MHz). The strength of the signal in a particular antenna is inversely proportional to the distance between the beam and that particular antenna. By combining the signals from all four antennae, the beam location is reconstructed. At a current of 10 μA (typical for this experiment) the beam position was resolved to ± 20 μm. The two BPMs used to determine the location of the beam on the target were located 1.3 and 7.5 meters upstream of the target platform (Figure 2.6).

Fast Raster

A fast raster located 23 meters upstream of the target steers the beam to create a profile of a 3mm diameter disk on the target. By knowing the current pattern of the magnets in the raster and by recording the position of the beam using the BPMs, the position of the beam is steered and determined to ± 0.1 mm in the beam's y-direction and $\pm$ 0.3 mm in the beam's x-direction. Overall location of the beam was kept to within ± 0.5 mm of the target center.

2.2.5 Beam Energy

For the E94-010 experiment, three independent methods were used to measure the energy of the incident electrons [43]: by measuring the electron trajectory in a B-field (Arc Energy), by electron-proton scattering, and by electron-^{3}He elastic scattering.

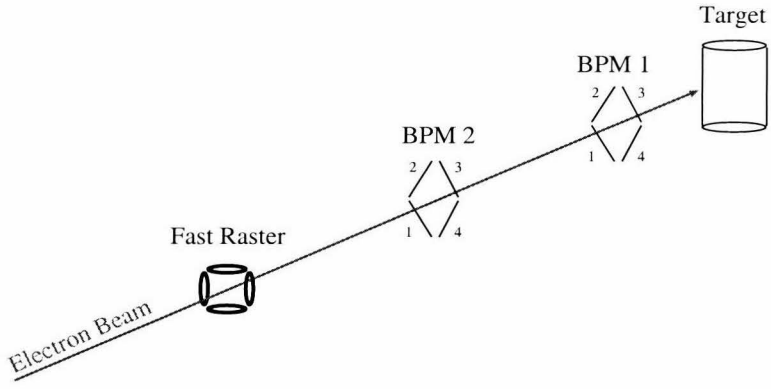

Figure 2.6: Relative positions of the BPMs and Fast Raster.

The Arc Energy method used the principal that an electron in a magnetic field moves in a circular pattern, the radius of which depends on the strength of the magnetic field and the electron's energy. Before electrons enter Hall A, they pass through a 34.3° bend: see Figure 2.7. The energy of these electrons is determined by the following relation: $E = c\frac{\int B_\perp \cdot dl}{\theta_{||}}$, where $B_\perp$ is the magnetic field perpendicular to the electron motion, dl is the path length of the electron, and $\theta_{||}$ is the angle by which the electrons are deflected. Precise knowledge of the beam's entrance to and exit from the bend is given using two sets of superharps. A superharp is a set of three wires that are spaced evenly apart. The superharp is moved across the beam path. When the beam strikes a wire, a current is generated and the beam's position is recorded. This information, along with the knowledge of the magnetic field, allowed for the determination of the electron's energy to a precision of $\Delta p/p$ to $\pm 2\times 10^{-4}$.

A second method used for the energy determination involved the scattering of an incident electron by a proton: p(e,e′p). The carbon target (CH_2) and detectors for this measurement were located 21.7 meters upstream of the target. For elastic scattering, the angles of the scattered electron and proton determine the energy of the incident electron:

$$E = M_p(\cot\frac{\theta_e}{2} \cdot \cot\theta_p - 1). \tag{2.7}$$

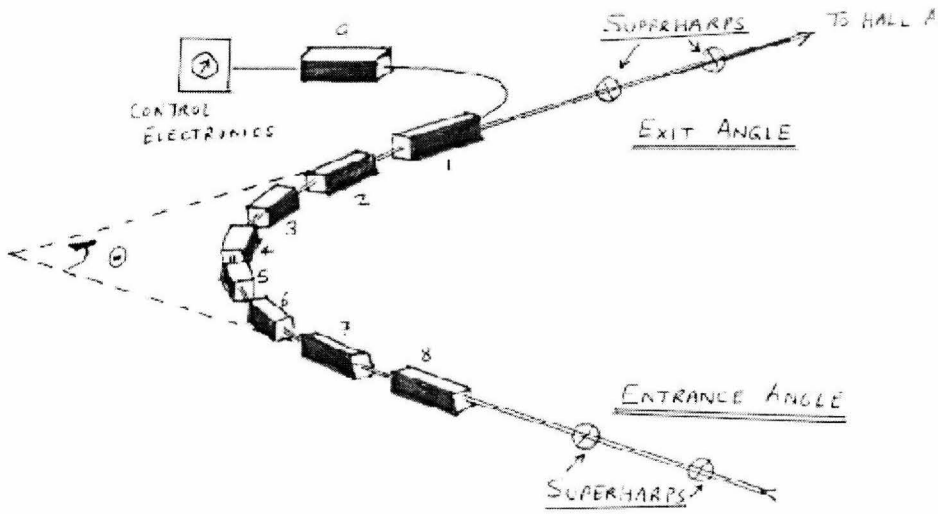

Figure 2.7: The Arc Energy device for Hall A.

Here $\theta_{p(e)}$ is the proton (electron) scattering angle and M_p is the proton mass.

The eP measuring device, as it's known in Hall A, consists of Cerenkov chambers, scintillators, silicon microstrips, and a CH_2 target, see Figure 2.8. An electron entering the eP device is scattered by a proton and then triggers a scintillator. The scattered proton is detected first with a microstrip (a plate of silicon that gives precise knowledge of the location of a particle passing through it) and then a set of scintillators. The scattered electron passes through a microstrip, then a scintillator, and then through a Cerenkov chamber. The Cerenkov light is detected by a phototube. Coincidence signals from the electron and proton scintillators define an event. Knowledge of the beam position and information from the microstrips allows for a calculation of the electron and proton scattering angles, from which the electron's incident energy can be calculated. The eP device has an energy resolution of $\Delta p/p = 1\times10^{-4}$.

A third method used to measure the incident electron's energy comes from elastic

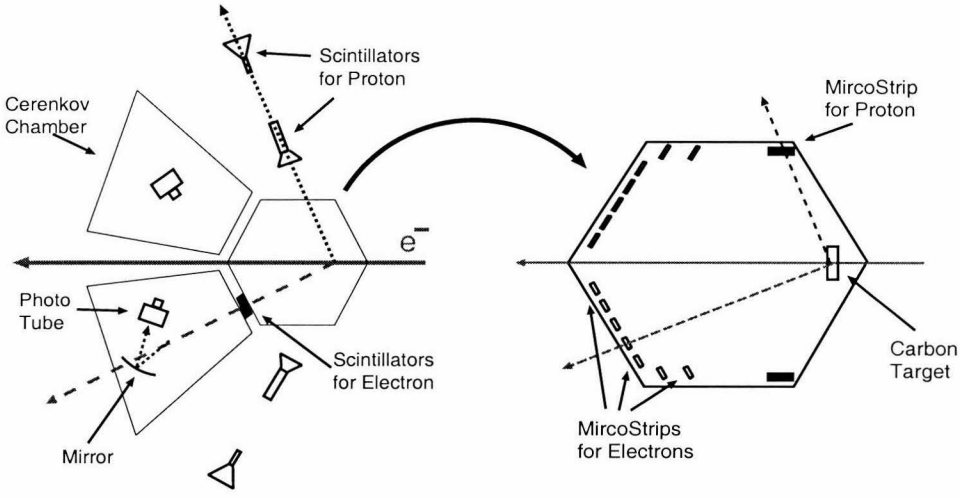

Figure 2.8: Schematic for the eP measuring device.

scattering by ^{3}He. The incident energy is given by

$$E = E'(1 + \frac{2E}{M_{^3He}} \sin^2 \frac{\theta}{2}), \tag{2.8}$$

where E is the incident energy and E is the energy of the scattered electron. By knowing the strength of the dipole field (γB [MeV]) and the spectrometer dispersion coefficients (d [m^{-1}]), one can determine the energy of the scattered electron. The equation $E = \gamma B[1 + \sum_{i=1}^{2} d_i x_{fp}^i]$ relates these quantities and the focal plane position (x_{fp} [m]) to the scattered energy (E). This measurement is limited by the uncertainty in the dispersion coefficients. Energy measurement made using this technique had an uncertainty of $\pm 3 \times 10^{-3}$.

Results for the three methods are shown in Table 2.2.

2.3 The Hall A Spectrometers

The detection of scattered electrons was conducted using Hall A's two high resolution spectrometers: the HRSH (High Resolution Spectrometer Hadron) and the HRSE

Nominal [GeV]	Arc [GeV]	eP [GeV]	Elastic [GeV]
0.860	-	-	0.8595
1.720	-	1.7179	1.715
2.500	2.5811	-	-
3.385	3.3850	3.3818	-
4.225	4.2362	4.2386	-
5.071	5.0555	-	-

Table 2.2: Energy measurements.

(High Resolution Spectrometer Electron). Each arm is approximately 26 meters long and 25 meters high, and both can be positioned at any angle between 12.5 and 165° relative to the beam line, see Figure 2.9. The scattered electrons first pass through a collimator ($\sim$ 121mm×63mm). The collimator was used to reduce the number of electrons entering the spectrometer originating from the target windows. The electrons then pass through four magnets. The first two are quadrupoles which focus the electrons in the vertical and transverse planes. The third magnet is a dipole which deflects the electrons 45° towards the ceiling. It has a central momentum range from 0.3 to 4 GeV/c with a momentum acceptance per setting of $\Delta p = 0.1$ and a resolution of $\Delta p/p \cong 10^{-4}$. The final quadrupole magnet de-focuses the electrons in the transverse direction. Next, the electrons enter the detector package (Figure 2.10) consisting of two planes of vertical drift chambers, a plane of scintillators, a gas Čerenkov detector, a second plane of scintillators, a lead glass pre-shower (HRSE arm only), and finally a lead glass shower counter.

2.3.1 Scintillators and Triggering

The two scintillator planes (S1 and S2) were responsible for triggering on electron candidates. Each plane consists of six scintillator paddles which overlap by 0.5 cm each (Figure 2.10). The active area of S1 is approximately 170cm × 35cm, and the active area of S2 is about 220cm × 54cm. There is a single photo-multiplier (PM)

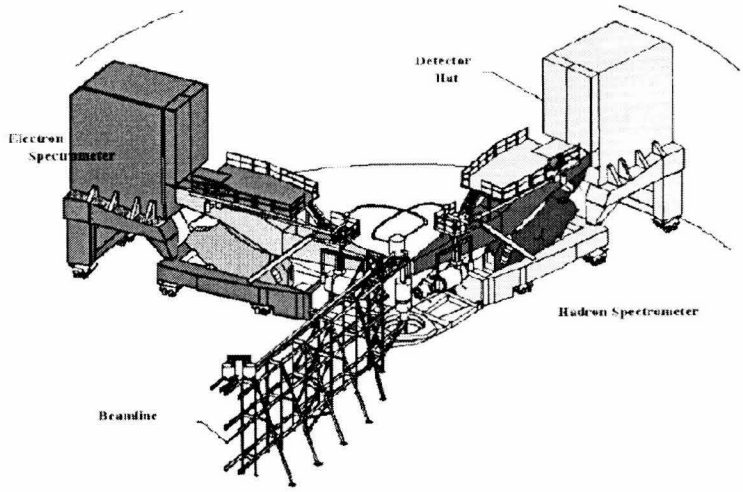

Figure 2.9: Hall A.

located at each end of a paddle. The PM signal is read out by an Analog-Digital Converter (ADC) and a Time-Digital Converter (TDC).

A signal in the two scintillators is considered a candidate when the following three conditions are satisfied. Both photo-multipliers on a paddle receive a signal. The signal from S1 and S2 are in coincidence. And the paddle on S2 corresponds to the paddle on S1 with some angular acceptance ($\pm$ 1 paddle on S1 and S2). A second type of event was also recorded when two of the three detectors, S1, S2, or Čerenkov (Section 2.3.3), fire. Most of these second type of events were junk. They were used to study the efficiency of the detectors.

2.3.2 Vertical Drift Chambers

The scattered electron's trajectory is a key element in determining its energy and in reconstructing its vertex at the target. Located in front of the other detectors and after the third quadrupole, two vertical drift chambers (VDCs) were used to measure the electron's trajectory [44, 45]. Each VDC is a panel of crisscross wires measuring

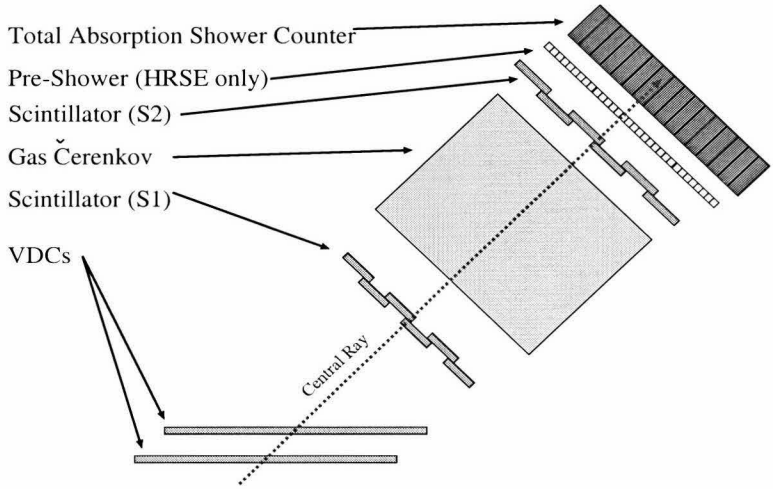

Figure 2.10: Detector package used for the E94-010 experiment.

211.8 cm $\times$ 28.8 cm. The panels are parallel to the Hall A floor. The scattered electron passes through the panels at 45° (Figure 2.11).

The wires form two planes: one U and one V. The U and V planes are perpendicular to one another. The VDC wires are enclosed between two Mylar windows. A voltage drop of -4kV was held between the windows and the enclosed wires. The gas between the windows consists of an equal mixture of argon and ethane. Each plane contains 368 wires made of gold-plated tungsten each with a diameter of 20 μm.

When an electron passes through the VDC chamber the gas along its path is ionized. The free electrons then accelerated towards a signal wire. As the electrons approach the wire they gain sufficient kinetic energy to ionized other gas atoms, creating more free electrons. This process continues, creating what is called an avalanche. As the electrons finally collide with the wire, they create a signal which is fed into a TDC and an ADC. The ADC and TDC are used to determine when the greatest number of avalanche electrons are hitting the wire. The time at which the electron passed through the VDC is given by the TDC connected to the scintillators. Knowledge of the drift velocity and the TDC signal from the signal wire yield the distance from the wire at which ionization first occurred. The resolution on the electron's

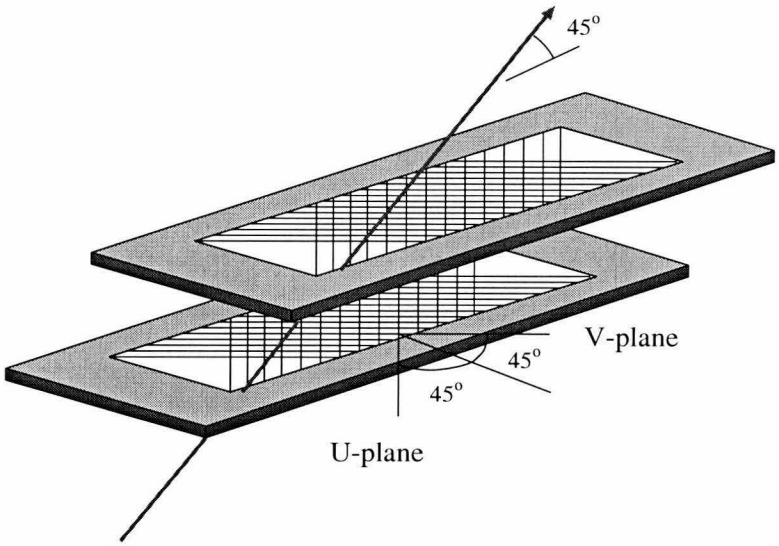

Figure 2.11: Schematic of VDC wire planes. Each plane has 368 signal wires.

position is approximately ± 200 μm.

2.3.3 Gas Čerenkov

A gas Čerenkov was employed in both the HRSE and HRSH in order to discriminate between electrons and pions. Čerenkov counters rely upon the fact that particles moving faster than the speed of light ($\beta > 1/n$), in a particular medium, will emit Čerenkov light [46]. This light is emitted in a cone at an apex angle given by $\theta_c = \cos^{-1}(1/(\beta n))$. By selecting a gas with the correct index of refraction, the term $1/(\beta \mathrm{n})$ will be less than one for electrons (real value for θ_c) and greater than one for pions (imaginary value for θ_c). Therefore, light will be emitted when an electron passes through, but not for a pion.

The Hall A Čerenkov detector [47] (Figure 2.12) is a rectangular tank measuring approximately 2×0.56 m on the entrance window and 1.5 m along the electron path. The tank was filled with 1 atm of CO_2, which has an index of refraction of n=1.00041. Electrons emit Čerenkov light if they have a minimal energy of 0.017 GeV. Pions

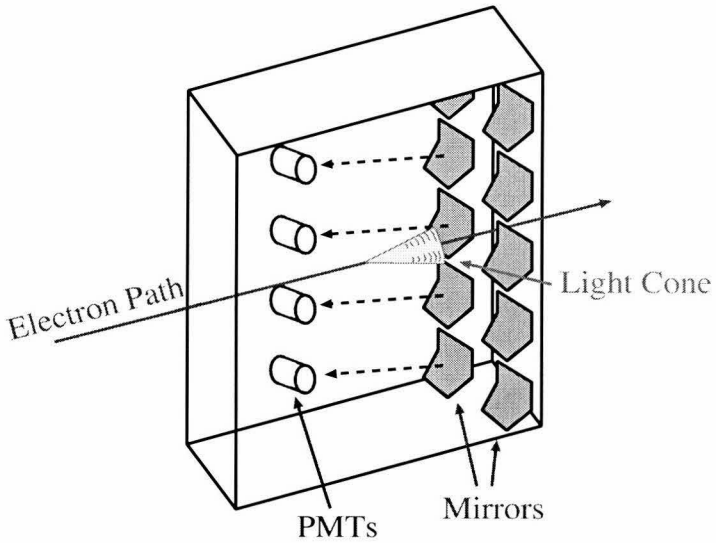

Figure 2.12: The CO_2 gas Čerenkov detector.

require an energy of at least 4.8 GeV to emit Čerenkov light. Since the spectrometers have a maximum momentum acceptance of 4.0 GeV, no pions in principal should be observed in the Čerenkov detector. Light from the passing electrons is collected by ten spherical mirrors located in front of the exit window of the detector. Each mirror reflects the light towards a particular photo-multiplier tube (PMT): see Figure 2.12. The electron detection inefficiency was found to be less than a few parts per thousand throughout the experimental run [48].

2.3.4 Shower Detector

The Hall A shower detector was used in conjunction with the Čerenkov detector to reject pions. When an electron passes through material it emits Bremsstrahlung radiation [44] along its path. This radiation creates secondary particles (γ,e^-,e^+) which, in turn, create still more particles. The result is a cascade of particles which is eventually converted to light and heat. The total amount of light emitted is proportional to the scattered electron's energy. A properly calibrated shower detector has an energy

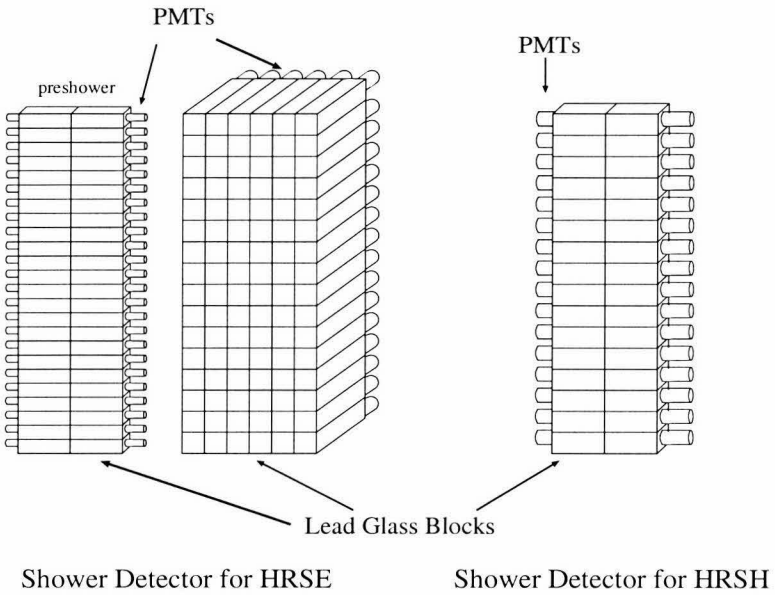

Figure 2.13: The configurations of the HRSE and HRSH shower detectors.

over momentum (E/p) ratio of one for electrons. Pions do not deposit as much energy as electrons and have an E/p ratio less than one; therefore, selection of electron can be based upon an event's E/p ratio.

The HRSE shower detector consists of two layers (Figure 2.13). The first layer, called the pre-shower, is made from 48 (24×2) blocks of TF-1 lead glass. Each block measures 10×10×35 cm. The pre-shower's total number of radiation lengths is 3.65 [49]. Here a radiation length refers to the distance an electron, on average, travels before its energy is reduced by a factor of 1/e. The second layer is made from 96 (16×6) blocks of SF-5 lead glass. The blocks measure 15×15×35 cm each, and the total number of radiation lengths is 15.2 [49]. Attached to the ends of the glass blocks are PMTs to collect the light.

The HRSH shower counter was installed specifically for the E94-010 experiment. It consists of 32 (16×2) SF-5 lead glass blocks (Figure 2.13). The total radiation length is approximately six.

Chapter 3 The Polarized ^{3}He Target

The E94-010 experiment used polarized ^{3}He as a source of polarized neutrons. The design was based upon a similar target built at SLAC [50]. Polarization of the ^{3}He nuclei was achieved via spin-exchanged collisions with optically pumped rubidium vapor [51, 52, 53, 54]. Details of this process along with a description of the target design and target cells are covered in this chapter.

3.1 Optical Pumping and Spin Exchange

3.1.1 Optical Pumping

The first step towards polarizing the ^{3}He nucleus is to create a source of polarized electrons that will later collide and transfer their spin polarization to the ^{3}He nuclei. These polarized electrons are provided by optically pumping Rb atoms. A review of optical pumping of alkali metals is described by W. Happer [51] and more recently by S. Appelt *et al.* [55]. Rubidium has a single outer shell electron ($5S_{1/2}$) and when placed in a magnetic field its Hamiltonian operator is given by [55]

$$\hat{H}_g = A_g \hat{\mathbf{I}} \cdot \hat{\mathbf{S}} + g\mu_B \hat{S}_z B_z - \frac{\mu_I}{I} \hat{I}_z B_z. \tag{3.1}$$

The first term of Equation 3.1 represents the vector coupling of the electron's spin ($\hat{\mathbf{S}}$) to the spin of the nucleus ($\hat{\mathbf{I}}$), with a strength given by A_g. The last two terms of Equation 3.1 describe the coupling of the electron and nuclear spins to the magnetic field (B_z). The strength of these couplings is proportional to the value of the magnetic field and depends on the g value for the electron (g=2.00232), the Bohr magneton (μ_B=9.2741$\times 10^{-21}$ erg G^{-1}), the nuclear magnetic moment (μ_I) in nuclear

magnetons, and the nuclear-spin quantum number ($I = 5/2$ for ^{85}Rb and $I = 3/2$ for ^{87}Rb). The electron is an eigenstate of the total spin quantum number $F = I + S$, which equals 3 or 2 for ^{85}Rb (76.6% natural abundance) and 2 or 1 for ^{87}Rb (23.4% natural abundance). The presence of a magnetic field splits the F state into various sub-levels: m_F.

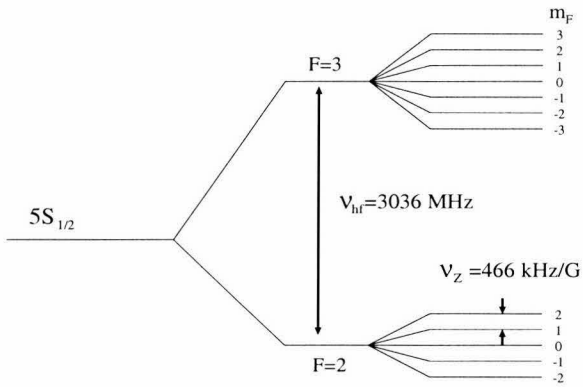

Figure 3.1: Level diagram for ^{85}Rb. The Zeeman splitting of the m_F sub-levels is given by ν_Z.

The process of optical pumping begins by exposing a sample of rubidium vapor with circularly polarized photons tuned to the D1 ($5S_{1/2} \longrightarrow 5P_{1/2}$) transition. If the photon helicity is in the same direction as the magnetic field, then electrons from all sub-levels, except the $m_F = 3$ (for the case of ^{85}Rb) sub-level, can be excited. These excited electrons can return to any of the ground state sub-levels. In time, all but the $m_F = 3$ sub-level will become depopulated.

A simplified form of the optical pumping process is shown in Figure 3.2. Here electrons in the $m_J = -1/2$ ground state are excited to the $(5P_{1/2}, m_J = 1/2)$ state where they decay to the $m_J = 1/2$ and $m_J = -1/2$ ground states. Since selection rules prohibit the $m_J = 1/2$ ground state electrons from being excited, the $m_J = -1/2$ ground state will quickly become depopulated.

As excited electrons return to the ground state they will emit a photon at the D1 wavelength (795 nm). This photon is randomly polarized and can excite electrons

from the $m_F = 3$ ground state. Since optical pumping relies on these electrons not being excited, a method known as quenching is employed to prevent the optical de-excitation of electrons. A buffer gas of N_2 is introduced. Collisions between the Rb and N_2 allow, through the mechanical excitation of N_2, the electron to decay without emitting a photon. The amount of N_2 gas is chosen to be a couple of orders of magnitude less than the ^{3}He density and few orders of magnitude more than the Rb density. For this condition, only about 5% of excited electrons decay by emitting a photon [50].

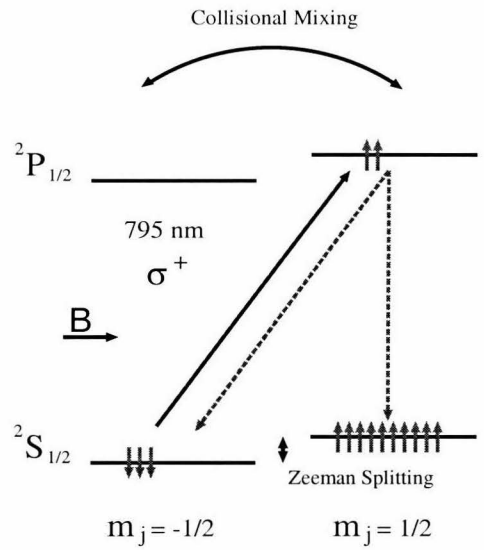

Figure 3.2: Optical pumping of Rubidium.

In regions of abundant laser light, high Rb polarization is expected. The local polarization (P_{Rb}) of the Rb vapor is given in terms of the optical pumping rate (R) and the spin destruction rate (Γ_{SE}):

$$P_{Rb} = \frac{R}{R + \Gamma_{SD}}. \tag{3.2}$$

The electron spin destruction rate is primarily governed by collisions of Rb atoms with other gas particles, as opposed to collisions with the wall or depolarization from

photons created by optical de-excitation. The rate is given by:

$$\Gamma_{SD} = k_{Rb-He}[^3He] + k_{Rb-Rb}[Rb] + k_{Rb-N_2}[N_2] \tag{3.3}$$

The spin destruction rate constants, k_{Rb-x}[cm^3/s], have been measured by Wagshul and Chupp [56]: $k_{Rb-He} \leq 2 \times 10^{-18}$, $k_{Rb-Rb} = 8 \times 10^{-13}$, and $k_{Rb-N_2} = 8 \times 10^{-18}$. The densities of the various species for our experiment are [He]$\approx 2\times10^{20}$cm^{-3} and [N_2]$\approx 2\times10^{14}$cm^{-3}; the rubidium density is given by the Killian formula [57]: [Rb] $= 1.507 \times 10^{26}(\frac{10^{-4040/T}}{T}) \approx 2.5 \times 10^{18}$cm^{-3} for $T = 170$°C. An order of magnitude approximation for the spin destruction rate is $1/\Gamma_{SD} = 10^{-3}$s. The depopulation rate of the $m_j = -1/2$ ground state is on the order of 10^{-6}s [53]. Rubidium vapor is therefore nearly 100% polarized in regions where optical absorption is occurring and nearly zero in regions where the light does not penetrate.

3.1.2 Spin Exchange

The transfer of polarization from the Rb electrons to the ^{3}He nuclei occurs through a weak hyperfine interaction in which a ^{3}He nucleus collides and exchanges its spin with the outer electron of rubidium. The evolution of the ^{3}He polarization ($P_{He}(t)$) is given by:

$$P_{He}(t) = < P_{Rb} > \frac{\gamma_{SE}}{\gamma_{SE} + \Gamma}\left(1 - e^{-(\gamma_{SE}+\Gamma)t}\right), \tag{3.4}$$

where $< P_{Rb} >$ is the volume average rubidium polarization, the spin exchange rate is given by γ_{SE}=k_{SE}[Rb], and Γ is the ^{3}He nuclear spin relaxation rate in the absence of Rb vapor or an electron beam. The spin exchange rate constant was measured to be $k_{SE} = (6.7 \pm 0.6) \times 10^{-20}$[cm^3/s] [52]. For our rubidium density, γ_{SE} is about 1/(10 hrs). The relaxation rate was measured for each cell and had a typical value of about 1/(40 hrs). A typical maximum polarization for the cells out of the electron beam was 40%. Working backwards, this implies a volume averaged Rb polarization of about 60%. Although procedures exist to measure the Rb polarization [58], they

were not implemented for this experiment.

3.2 Target Cells

The optical pumping and spin exchange process take place within a target cell. The cells are made from an aluminum-silicate glass (Corning 1720 or GE180) and are comprised of three parts: a pumping chamber, a target chamber, and a transfer tube (Figure 3.3). The pumping chamber is spherical and was placed within a plastic oven in order to control the rubidium vapor density. The target chamber is a 40 cm tube that was placed along the electron beam path. The transfer tube simply connects the two chambers.

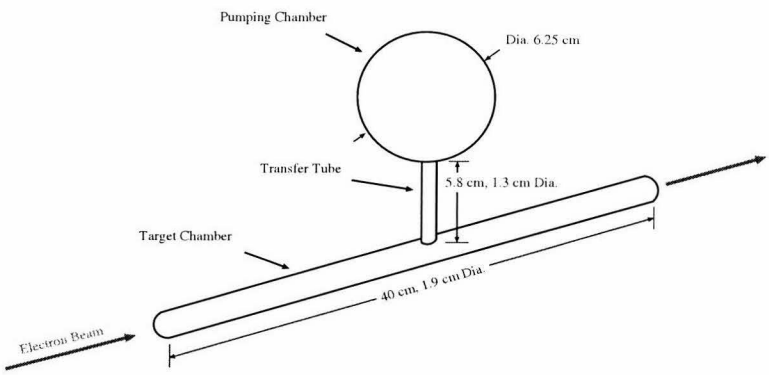

Figure 3.3: A target cell with basic dimensions.

Six target cells were used for this experiment and each cell was given a name: *Don't Worry, Be Happy, Armageddon, Nepheli, Sysiphos,* and *Jin.* Their construction involves three steps. First, stock tubing is blown to a larger diameter for the target chamber and transfer tube. This is done in order to reduce the presence of micro fissures along the interior walls. A spherical cell is formed separately to make the pumping chamber. All three parts are cleaned with an acid wash, joined, and then connected to a glass string that is attached to a vacuum system. The second step is to bake the target cell while under vacuum. This reduces the presence of paramagnetic

impurities that cause depolarization via collision with ^{3}He or rubidium. Once the cell is baked out and a good (10^{-9} torr) vacuum is achieved, the cell is filled. First, rubidium is chased into the pumping chamber. Next, N_2 gas is filled into the cell to a pressure of 60-70 torr. Last, the cell is filled to about 10 atm. of ^{3}He. Before the cell is sealed, or "tipped off," a container of liquid helium is placed around the target chamber. This reduces the internal gas pressure to below 1 atm. and makes the target cell safe to tip off.

By studying the decay of polarization in an apparatus similar to the one described in Section 3.3, a cell's lifetime ($=1/\Gamma$) was measured. The lifetime of a cell is the amount of time it takes for the ^{3}He polarization to drop by a factor of $1/e$ when the cell is at room temperature and no electron beam is present. A cell with a short lifetime ($\leq$20 hrs) cannot obtain high polarization. Lifetime was an important selection criterion on cell quality. The lifetimes are listed in Table 3.1.

Cell	Lifetime (hours)
Don't Worry	43.5±1
Be Happy	39.5±1
Armageddon	40±1
Nepheli	20±1
Sysiphos	53±1
Jin	29±1

Table 3.1: Lifetimes for the target cells measured after construction.

3.2.1 Cell Geometry

A cell's mechanical properties are important for accurately determining the amount of ^{3}He polarization, the density of the target as seen by the electron beam, and the amount of material through which the incident and scattered electron pass. The relevant pieces of information needed are: the thickness of the target chamber entrance window, the thickness of the target chamber wall, the total internal volume, the vol-

umes of the three target cell components, and the inner radius of the target chamber. The following sections describe how the cell geometry was characterized.

Window Thickness

The entrance and exit windows for the target chamber were constructed to have thin windows (≈100 microns). Accurate measurement of the window thickness is important in understanding the amount of energy the electron loses as it passes through the glass window for estimating radiative corrections.

Two methods were used to measure the window thickness: one mechanical and the other optical. After the end windows were blown, they were measured using a micrometer of 1.3 μm resolution [50]. The results are listed in Table 3.2 and should only be considered a check of the optical method. The optical method used scattered laser light from the surface of the window. The intensity of the light depends on the wavelength and window thickness. The intensity of reflected light off of a parallel plate is given by [59]:

$$I_r = \frac{\frac{4\left(\frac{n-1}{n+1}\right)^2}{\left(1-\left(\frac{n-1}{n+1}\right)^2\right)^2}\sin^2\left(\frac{2\pi nt\cos\theta_2}{\lambda}\right)}{1+\frac{4\left(\frac{n-1}{n+1}\right)^2}{\left(1-\left(\frac{n-1}{n+1}\right)^2\right)^2}\sin^2\left(\frac{2\pi nt\cos\theta_2}{\lambda}\right)}, \tag{3.5}$$

where n is the index of refraction (1.528±0.01), λ is the wavelength of the incident laser light (780 nm), θ_2 is the angle of the refracted light (3.27°), and t is the thickness of the window. The basic setup is shown in Figure 3.4. For the surface to be considered a parallel plate, a small beam spot size was used and only the reflected light that was in the same plane as the incident beam and surface normal was detected. By recording and fitting the variation of the intensity as a function of wavelength to Eq. 3.5, the thickness was determined to an uncertainty of ±0.5%. Results are listed in Table 3.2.

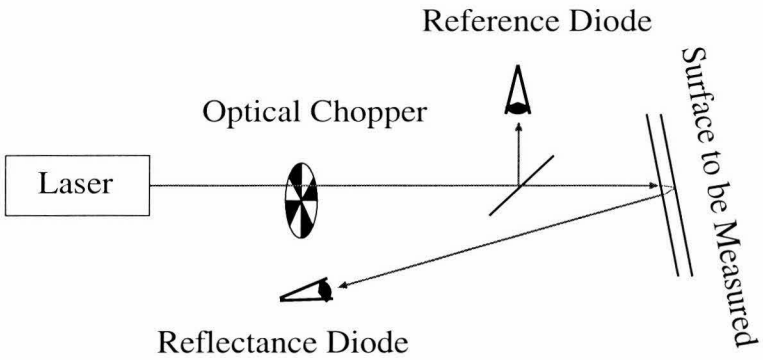

Figure 3.4: Setup for an interferometric thickness measurement.

Internal Volume

The total internal volume can be measured precisely using Archimede's principle, which equates the magnitude of the buoyant force to the weight of the fluid displaced. After a cell was created, it was tied to a block of known volume and weight, attached to a scale, and lowered into a bath of water. The internal volume, $V_{internal}$, of the target cell is given by:

$$V_{internal} = \frac{1}{\rho_g}\left(\rho_b V_b + m_{He} + \rho_g V_w - \rho_g V_b - \rho_w V_w - \frac{W_{c+b}}{g}\right), \tag{3.6}$$

where g is the gravitational constant, ρ_g is the density of glass, ρ_b is the density of the block, ρ_w is the density of water, V_g is the volume of the glass, V_b is the volume of the block, V_w is the volume of the water displaced by the cell-block combination, W_{c+b} is the weight of the cell-block combination when it is submerged, and m_{He} is the estimated mass of the ^{3}He (0.3 grams). The precision of this method is about 0.5% with the dominant uncertainty coming from the measurement of the amount of displaced water. Results are listed in Table 3.3.

Determining the internal volume is the first step towards calculating the volumes of the various chambers. The internal volume of a particular chamber was determined in two ways. The first is done by multiplying a chamber's outer volume by the ratio

Target Cell	Window #	Thickness [μm]	
		Mechanical	Optical
Don't Worry	2	137.2±1.3	135.9±0.6
	21	143.5±1.3	140.1±0.5
Be Happy	4	129.5±1.3	-
	5	132.1±1.3	135.3±1.6
Armageddon	VII	125.7±1.3	121.9±0.6
	XVIII	142.2±1.3	139.1±0.7
Nepheli	-	-	-
	-	-	-
Sysiphos	9	152.4±1.3	134.2±1.0
	18	132.1±1.3	121.0±1.0
Jin	14	142.2±1.3	136.1±1.2
	15	137.2±1.3	134.8±0.8

Table 3.2: Target chamber window thicknesses. *Nepheli*'s windows were not recorded.

Cell	Wall Thickness		r_{target}	V_{pump}	$V_{transfer}$	V_{target}	V_{total}
	ave. [mm]	uncertainty	[cm]	[cm^3]	[cm^3]	[cm^3]	[cm^3]
Don't Worry	0.995	3.7%	0.843	107.7	6.5	82.8	197.1
Be Happy	0.990	9.0%	0.833	122.3	5.1	89.8	217.2
Armageddon	1.182	9.0%	0.810	97.2	4.9	86.4	188.5
Nepheli	0.956	9.0%	0.860	104.2	6.4	91.0	201.5
Sysiphos	0.986	2.5%	0.902	110.0	5.5	97.0	212.4
Jin	0.874	4.0%	0.866	102.0	8.4	89.1	199.5

Table 3.3: Internal dimensions for the target cells.

of the total internal and external volumes:

$$V_{chamber}(internal) = V_{chamber}(external)\frac{V_{internal}}{V_{external}}. \tag{3.7}$$

A caliper was used to measure the external volumes.

A second method starts by using the external dimensions and subtracting away the glass thickness. The amount subtracted was determined using the results of the total internal volume measurement. In this way, internal dimensions were predicted and volumes calculated. Results are listed in Table 3.3. The two methods agreed to within

1%. Taking this into consideration, along with the uncertainty in the total internal volume, a ±1.5% uncertainty was placed on the chamber volume determination.

Target Chamber Wall Thickness

Measurement of the target chamber wall thickness was carried out in the same manner as the window thickness. The measurements were performed after the experiment on the surviving target cells: *Don't Worry, Sysiphos*, and *Jin*. For these cells, the average variation of the thickness (t) along the length of the cell was $\frac{\Delta t}{t} = 0.03$. The uncertainty on the average thickness was about ±3.5%.

For the target cells that did not survive the experiment–*Be Happy*, *Armageddon*, and *Nepheli*–a thickness had to be inferred from a comparison of the optical method to a method which assumes a constant cross-sectional area during the enlarging process. Recall that the stock tubing for the target chamber is blown to a larger diameter to remove micro-fissures. The original stock tubing had an outer radius $r_o = 0.741$ cm for Corning 1720 and 0.788 cm for GE 180 and an inner radius of $r_i = 0.630$ cm for Corning 1720 and $r_i = 0.621$ for GE 180. The thickness is predicted from measuring the resized tube's outer radius (r'_o):

$$thickness = r'_o - \sqrt{(r'_o)^2 - (r_o^2 - r_i^2)}. \tag{3.8}$$

The optical method on surviving cells found a systematic shift of 14%±9% greater thickness than the mechanical method. The mechanical thicknesses of *Be Happy*, *Armageddon*, and *Nepheli* were adjusted by adding this amount. Results are listed in Table 3.3.

3.2.2 Cell Density

Knowledge of the ^{3}He density within the target cell was needed for calculating radiative corrections, determining the target polarization, and, eventually, for extracting

the ^{3}He total cross section. Two methods were used to measure the ^{3}He density. One relies on keeping track of temperatures, volumes, and pressures during the filling process. The other is an optical technique. Both methods were to find the final density for each target cell.

During the filling process ^{3}He is deposited into the target cell from a calibrated volume (Figure 3.5). The volume is filled with a small amount of ^{3}He to a particular pressure and then released into the target/string combination. By repeating the process, the final desired number density of the ^{3}He is obtained. This "fill density" is calculated from the ideal gas law and is given by [60]:

$$n_0 = \frac{1}{k_B T_{fill} V_{cell}} \left(\left(\sum_{j=1}^{N-1} (P_j^{int} - P_j^{final}) + P_N^{int} \right) V_{fill} - P_{final}(V_{fill} + V_{string-cell}) \right), \tag{3.9}$$

where n_0 is the number density of the ^{3}He within the target cell, N is total number of times the cell is filled from the calibrated volume, P_j^{int} is the pressure in the fill volume after charging it up for the j-th time, P_j^{final} is the equilibrium pressure after opening the valve to the string/target cell for the j-th time, P_{final} is the equilibrium pressure in the charge volume and string after the target cell has been pulled off, T_{fill} and V_{fill} are the temperature and volume of the calibrated volume, and $V_{string-cell}$ is the volume of the string after the cell has been pulled off. Results are listed in Table 3.5. The uncertainty in this method is 2.2%.

Once a cell has been created, its density can be measured by observing the collisional absorption broadening [61, 62]. The natural D1 and D2 absorption lines of Rb are broadened by the presence of ^{3}He. By measuring the absorption spectrum, the density of ^{3}He was determined.

The absorption spectrum has the form $\ln \frac{I(0)}{I(\nu)} \sim \sigma(\nu)$, where $I(0)$ is the incident intensity, $I(\nu)$ is the transmitted intensity, and $\sigma(\nu)$ is the absorption cross section.

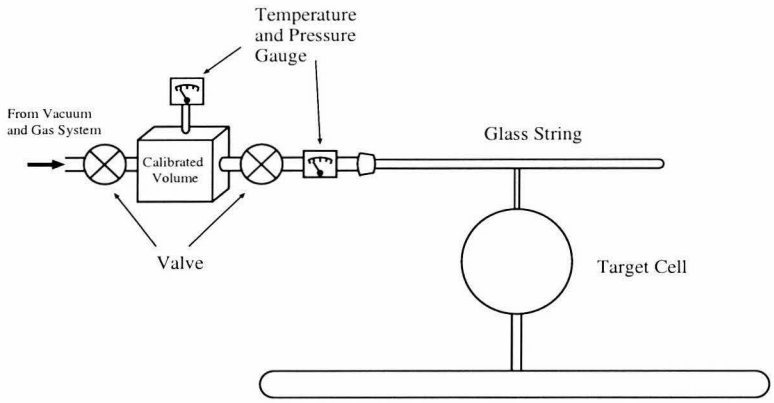

Figure 3.5: The cell filling system.

The absorption cross section has the form of an asymmetric Lorentzian:

$$\sigma(\nu) = \frac{A[1 + C \cdot \delta\nu]}{(\delta\nu)^2 + (\Gamma/2)^2} + B, \tag{3.10}$$

where A, B, and C are fit parameters and Γ is the line-width. Γ is proportional to the density of the gas: $n_0[\mathrm{cm}^{-3}]=\mathrm{k}_{broadening}\Gamma$. The constants of proportionality, $\mathrm{k}_{broadening}$, were determined using a reference cell filled to a known number density [61]. They are listed in Table 3.4. They are in units of Gigahertz per amagats. An amagat (amg.) is the number of particles per cubic centimeter at 0°C and 1 atmosphere: 1 amg. = 2.689×10^{19} cm^{-3}.

	^{3}He	N_2
D1 full width [GHz/amg]	18.7±0.3	17.8±0.3
D2 full width [GHz/amg]	20.8±0.2	18.1±0.3

Table 3.4: Constant of proportionality used to determine density from optical line broadening.

For each cell both the fill density and the average of D1 and D2 line widths were recorded. The average of the D1 and D2 results are considered one measurement of the ^{3}He density. The uncertainty in this method is 1.1%. The results are listed in

Table 3.5. Results of the measurements, along with a weighted average, are listed in Table 3.5. The uncertainty on the final weighted average of the density is assigned to be ±1.0%.

Cell	D1	D2	D1-D2 Ave.	Fill	Weighted Mean (n_o)
Don't Worry	10.03	9.94	9.99	9.82	9.93
Be Happy	9.28	9.39	9.34	9.33	9.32
Armageddon	10.09	10.25	10.17	10.14	10.15
Nepheli	11.47	11.32	11.40	11.0	11.33
Sysiphos	8.31	8.14	8.23	8.09	8.16
Jin	8.46	8.42	8.44	8.42	8.41

Table 3.5: Results of measurements of the ^{3}He density in amagats.

3.3 Target Setup

The target used for the E94-010 experiment is comprised of three main systems: an optical pumping system, a Nuclear Magnetic Resonance (NMR) system used to measure the target's polarization, and an Electron Paramagnetic Resonance (EPR) system, discussed in Section 4.2.8, used to calibrate the NMR system (Figure 3.6).

Optical Pumping System

The optical pumping system's principal components are the Helmholtz coils used to create a holding field and the laser system used to optically pump the rubidium's outer shell electron. Two sets of Helmholtz coils were to used create a uniform field of 20 Gauss about the target. The two coil sets were perpendicular to one another and turned 19 degrees off of the central beam line (Figure 3.7). Their approximate size was 60 inches in diameter (Figure 3.8). The direction of the holding field was kept along the beam path and rotated perpendicular to the beam in order to redirect the ^{3}He spins.

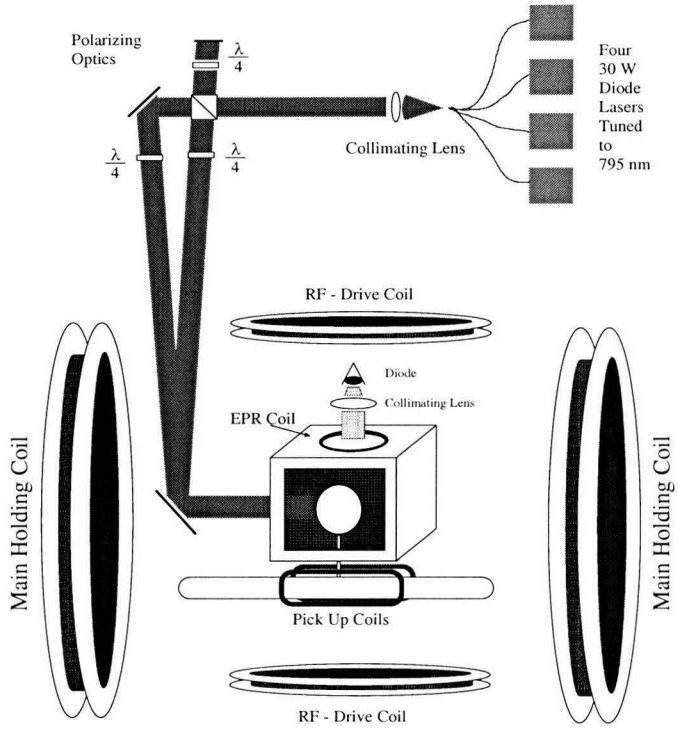

Figure 3.6: Schematic of the E94-010 target showing components of the pumping system, NMR system, and EPR system. A second set of Helmholtz coils is not shown.

The laser system used to pump the rubidium vapor was designed and constructed at Caltech (Figure 3.9). Its basic structure is comprised of seven diode lasers, a set of circular polarizing optics to polarize the laser light, and a set of mirrors and lenses to direct the light towards the target. The entire system was housed in a protective concrete hut located near the target on the Hall A floor. The diodes were manufactured by *OptoPower*. They consist of two 15 Watt diode bundles that are coupled together into one fiber optic cable. The lasers have both local current and temperature controls, and a system was created that allowed for control of the laser operation from the counting house. The output had a FWHM of $\leq$2.5 nm and achieved 30 Watts of output power at a central wavelength of 795 nm. The light that is emitted from the end of the fiber optic cable comes out in a 12° cone.

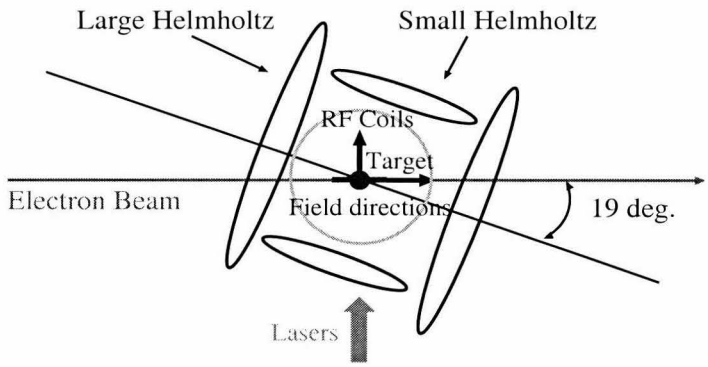

Figure 3.7: A top view of the E94-010 target.

The system of optics (Figure 3.9) used to direct the divergent diode laser to the target starts with a collimating lens. Using a polarizing cube, the light is split into its S and P components of linear polarization. The P component passes straight through the cube and reflects off a mirror. It then passes through a quarter-waveplate and on towards the target. The S component passes out of the polarizing cube at 90°. Moving away from the target, the S component passes through a quarter-waveplate, is reflected by a mirror, and back through the same quarter-waveplate. This process has the effect of rotating the sense of polarization by 90°. The light then passes straight through the polarizing cube and then through a quarter-waveplate on its way towards the target. Four of the seven lasers were dedicated for pumping in the longitudinal direction (when the magnetic field is aligned with the electron beam). Once the light from these lasers reach the target area, they are directed down and onto the target by a pair of compensating mirrors. The other three lasers are used for transverse pumping (when the magnetic field is pointing 90° with respect to the electron beam direction) and reach the target directly from the side. Helicity of the longitudinal lasers could be reversed remotely using a set of half waveplates. The laser system was robust and ran with nearly 100% efficiency during the experiment.

The ^{3}He target was mounted to a target ladder which also contained spaces for a reference target and a carbon foil target (Figure 3.10). The reference target could

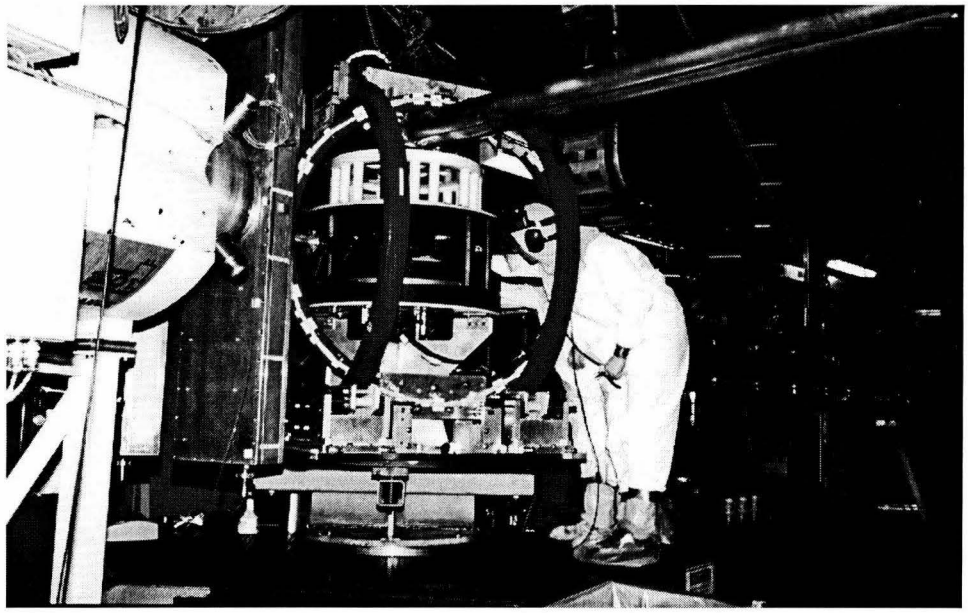

Figure 3.8: The E94-010 target in situ at Jefferson Lab.

be evacuated or filled with either N_2 or ^{3}He up to 70 psi. The carbon foil target had seven thin plates of carbon spaced evenly apart. It was used to study the optics of the spectrometers. Finally, the target could be put into a "no-target" position for beam tuning.

The target ladder was mounted onto a Torlon (a high temperature plastic) oven which was used to heat the pumping chamber. Hot air was passed into the oven through an electric coil heater. The temperature was regulated using a Resistive Thermal-couple Device (RTD) mounted on the inside of the oven. The oven was mounted to a rod that could move vertically, allowing the different targets into the beam line remotely. Cooling jets of ^{4}He were directed at the end windows of the target chamber to cool them from the electron beam heating.

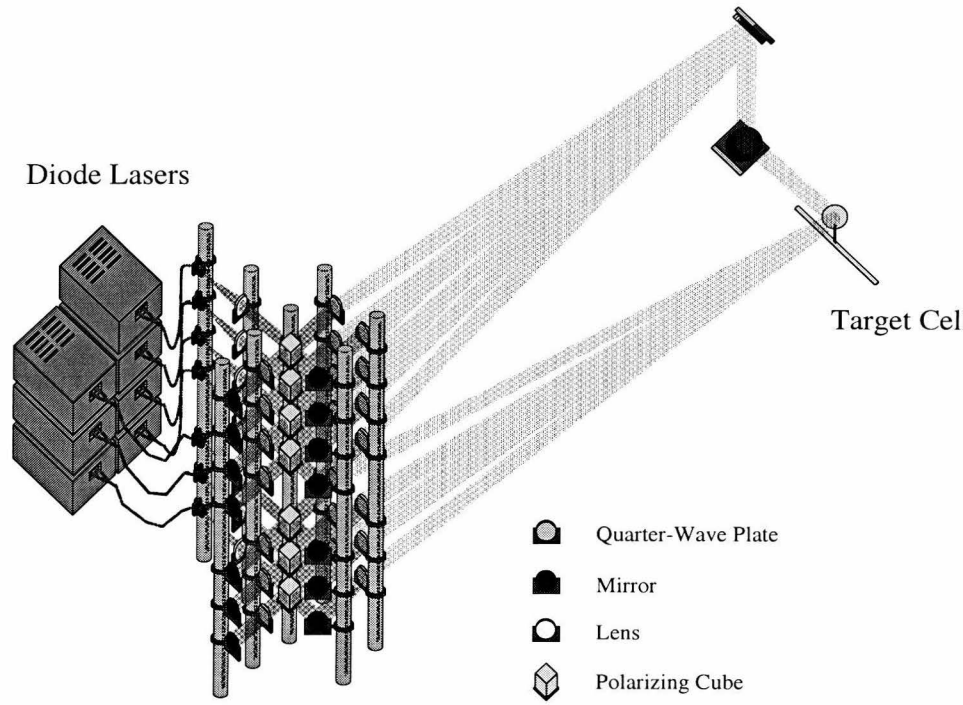

Figure 3.9: The E94-010 laser system. Not shown in the drawing is a set of half-waveplates that could be moved in and out of the laser path to reverse the helicity.

NMR System

The value of the ^{3}He polarization was determined from observing the ^{3}He Nuclear Magnetic Resonance (NMR) signal. Two additional components were added to the system in order to make this measurement (Figure 3.6). A Helmholtz coil was placed around the target in order to create a vertical RF field. The field had a frequency of 91 kHz and a magnitude of about 100 mG. A set of pickup coils was placed within the target chamber and used to detect the NMR signal. They were 1 inch tall, 4 inches long, and 1/2 inch wide. Each coil had 150 windings of 32 gauge copper wire. When a measurement needed to be taken, the target chamber was lowered out of the beam path and placed in between the pick coils (Figure 4.4).

The NMR system was controlled using a computer located in the counting house (Figure 3.11). The signal from the pickup coils was read by a lock-in amplifier refer-

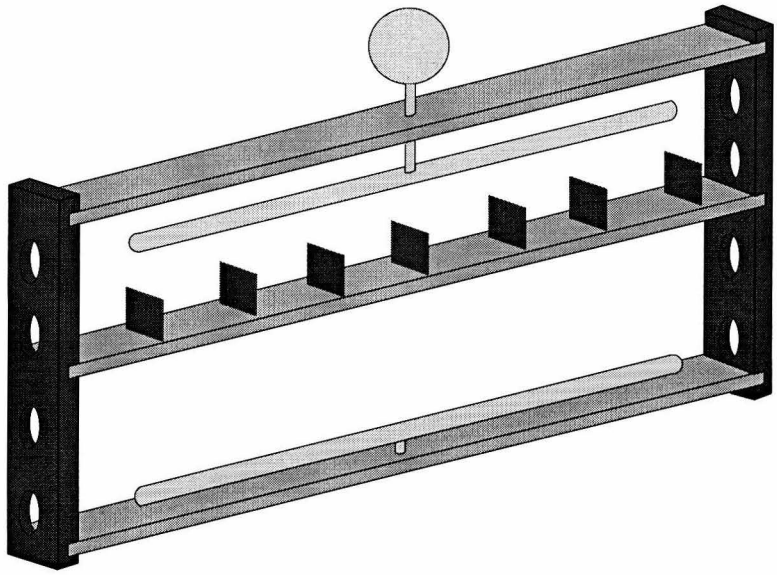

Figure 3.10: The target ladder used for the E94-010 experiment. The ^{3}He, reference, and carbon targets are shown.

enced to a RF generator. The output of the RF generator went into a RF amplifier located in the counting house, which was then connected to the RF coils located in Hall A. The magnitude of the holding field was swept from 18 to 25 Gauss using a function generator. The function generator creates a voltage sweep that is fed into the control input of a Kepco power supply.

3.3.1 Cell Temperature

Heating the pumping chamber causes ^{3}He to concentrate in the target chamber in order to equilibrate the pressure throughout the cell. Assuming an ideal gas law, the relation of the number density for a particular chamber to the nominal density is given by:

$$\frac{n_p}{n_0} = \left(1 + \frac{V_{target}}{V_{total}}\left(\frac{T_p}{T_t} - 1\right)\right)^{-1} \quad \text{and} \quad \frac{n_t}{n_0} = \left(1 + \frac{V_{pump}}{V_{total}}\left(\frac{T_t}{T_p} - 1\right)\right)^{-1}. \quad (3.11)$$

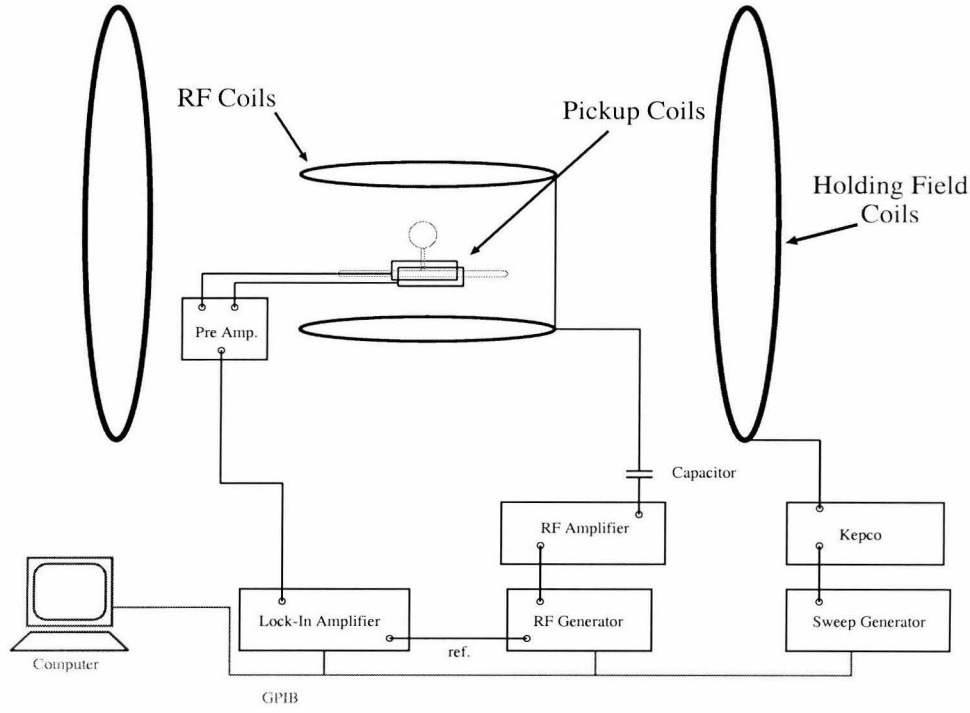

Figure 3.11: Schematic of the electronics used in the NMR system.

Here $n_{p(t)}$ and $T_{p(t)}$ are the volume averaged number density and temperature for the pumping (target) chamber. The volumes–V_{total}, V_{target}, and V_{pump}– are listed in Table 3.3 and the nominal densities, n_0, are listed in Table 3.5. What is needed to calculate $n_{p(t)}$ are the chamber temperatures.

In order to understand the temperature distribution each cell used had seven resistive thermocouple devices (RTDs) attached to them: two RTDs placed on the pumping chamber and five RTDs placed along the target chamber separated by 6 ± 1 cm (Figure 3.12). The RTD values were recorded by hand before polarimetry measurements were performed and by the DAQ at the beginning of each data taking run. At room temperature the RTD readings did not differ by more than 1°C. Under running conditions, the relative RTD readings were stable to within a few degrees. Average RTD values were calculated from all the values (75 to 150) recorded for a particular cell. To this value 1.4°C, as determined from a previous study [50], was added to

reflect a slight drop in temperature across the cell wall. The standard deviation on this average was approximately 3.5°C, and an uncertainty of 5°C was placed on each average RTD value.

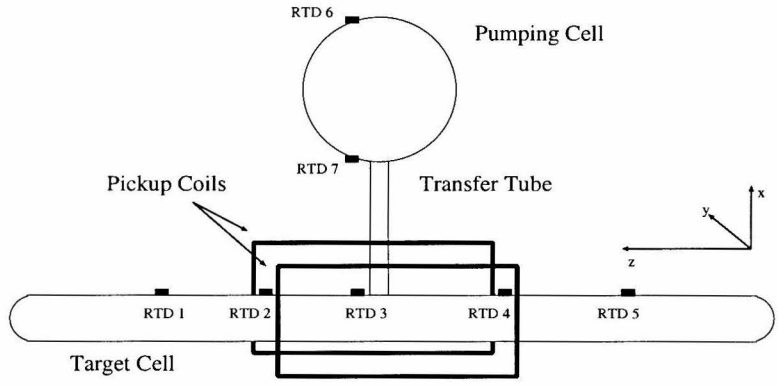

Figure 3.12: Position of the RTDs used to measure the temperature of a target cell.

A weighted sum of the RTD values was used to calculate T_t:

$$T_t = (6/40)(\text{RTD\#2} + \text{RTD\#3} + \text{RTD\#4}) + (11/40)(\text{RTD\#1} + \text{RTD\#5}). \quad (3.12)$$

Measurement of the pumping chamber's volume averaged temperature, T_p, is complicated by the deposition of heat from the lasers. Since the lasers tend to heat the center of the chamber, the temperature difference between T_p and the average of the pumping chamber RTDs ($\frac{1}{2}$(RTD#6 + RTD#7)) can be quite large. By looking at cases where two NMR signals, one with lasers on and one with lasers off, were conducted closely in time with one another, a prediction for this difference can be made.

The strength of a NMR signal is proportional to the density of ^{3}He between the pickup coils: $n_c = n_t(T_t/T_c)$, where T_c=(1/2)r3+(1/4)(r2+r4) is the temperature of the gas between the coils. If a NMR signal is obtained when the lasers are on (S_{He}^{on}) and when they are off (S_{He}^{off}), the temperature of the pumping cell while the lasers

were on is given by:

$$T_{predicted} = \frac{V_{pump} T_t^{on}}{\frac{S_{He}^{off}}{S_{He}^{on}} \frac{T_t^{on} T_c^{off}}{T_t^{off} T_c^{on}} \left[V_{total} + V_{pump} \left(\frac{T_t^{on}}{T_p^{off}} - 1 \right) \right] - V_{total} + V_{pump}} \tag{3.13}$$

Equation 3.13 is predicated on the assumption that all RTD measurements truly reflect the temperature inside the cell, except those on the pumping chamber when the lasers were on.

During the experiment there were 17 cases where a NMR measurement was performed with the lasers in one state and 5 to 15 minutes later with the lasers in the other state. The amount by which the pumping chamber is hotter than the average of RTDs #6 and #7 is called Δ. The 17 values calculated for Δ are shown in Figure 3.13. There was a large range of values predicted for the interior pumping chamber temperature with seemingly no correlation to the amount of time between NMR measurements or to whether the lasers were on or off initially. The large variation in results is most likely from unrecorded conditions at the time of the measurement.

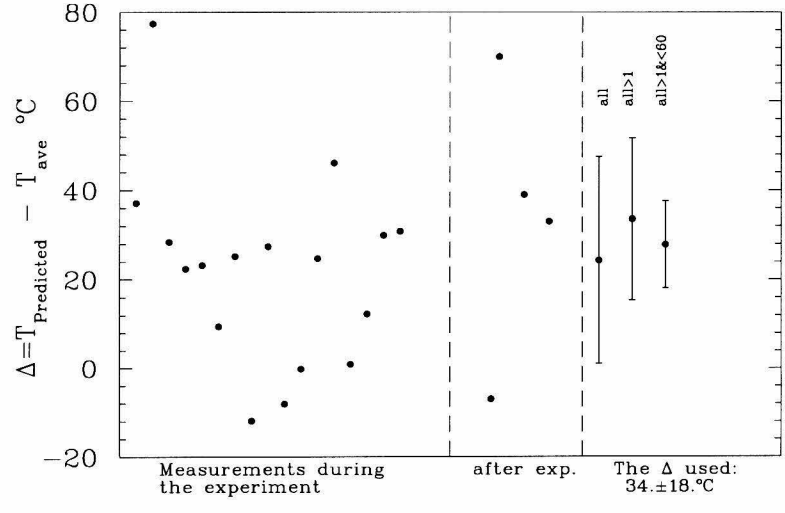

Figure 3.13: Measurements of Δ. Errors bars are standard deviations for different data sets.

To understand the variations, four, carefully recorded tests were conducted after

Cell	T_p (°C)	T_c (°C)	T_t (°C)	n_p/n_0	n_t/n_0	n_c/n_0
Don't Worry	235	67	64	0.825	1.224	1.211
Be Happy	221	57	53	0.829	1.234	1.221
Armageddon	213	62	54	0.819	1.201	1.175
Nepheli	214	57	55	0.821	1.201	1.194
Sysiphos	213	53	51	0.815	1.207	1.201
Jin	220	59	53	0.824	1.208	1.188

Table 3.6: Temperatures and relative densities.

the experimental run (Figure 3.13). The negative prediction for Δ was correlated to heaters coming on at the same time the lasers were turned off. This had the effect of temporarily making the pumping chamber hotter and forcing more ^{3}He into the target chamber. To circumvent this effect, two of the tests were done with both the laser and heater turned off. The calculated results for Δ were 39 and 34°C. The fourth test attempted to reproduce the conditions of the measurements taken during the experimental run. This time Δ was equal to 71°C. There was no apparent reason for this high value.

An average of all the measurements, which had a value greater than one, was used to calculate Δ. The uncertainty applied to this number was the standard deviation of these points. The final result of Δ was 34±18°C and $T_p = \Delta + (1/2)(\mathrm{r6} + \mathrm{r7})$ with an assigned uncertainty of ±18°C.

Using the results for T_p, T_t, and the volumes, Eqs 3.11 were solved. The results are listed in Table 3.6. Each relative density has an uncertainty of ±2.0%.

Chapter 4 ^{3}He Polarimetry

4.1 NMR-AFP Polarimetry

Knowledge of the ^{3}He polarization is critical for measuring the extended GDH sum rule. The polarization is monitored throughout the experiment by the Nuclear Magnetic Resonance (NMR) technique of Adiabatic Fast Passage (AFP) [63]. The strength of the NMR signal is proportional to the amount of polarization.

Classically, NMR-AFP is described by considering one free particle with spin $\mathbf{I}$ and magnetic moment $\mathbf{M} = \gamma\mathbf{I}$, where γ is the gyromagnetic ratio. When this particle is placed in a magnetic field $\mathbf{H}$, its moment experiences a torque:

$$\frac{d\mathbf{M}}{dt} = \gamma\mathbf{M} \wedge \mathbf{H}. \tag{4.1}$$

It's useful to transform this equation into a frame that is rotating at a frequency and direction given by $-\boldsymbol{\omega}$. Following [64], Eq. 4.1 becomes

$$\frac{\partial\mathbf{M}}{\partial t} = \gamma\mathbf{M} \wedge \left(\mathbf{H} - \frac{\boldsymbol{\omega}}{\gamma}\right). \tag{4.2}$$

The magnetic field $\mathbf{H}$ in Eq. 4.1 is now replaced by an effective field comprised of the laboratory field and a fictitious field, $\mathbf{H}_e = \left(\mathbf{H} - \frac{\boldsymbol{\omega}}{\gamma}\right)$.

In our case, the laboratory field is a holding field in the z-direction, $H_z\hat{\mathbf{k}}$, and a RF field in the x-direction, $\mathbf{H}_{rf} = 2H_1\cos(\omega_0 t)\hat{\mathbf{i}}$. The RF field can be expressed in terms of two counter-rotating components:

$$\mathbf{H}_{rf} = H_1\hat{\mathbf{i}}'_+ + H_1\hat{\mathbf{i}}'_-, \tag{4.3}$$

where $\hat{\mathbf{i}}'_{\pm} = \cos(\omega_0 t)\hat{\mathbf{i}} \pm \sin(\omega_0 t)\hat{\mathbf{j}}$. If we set $\boldsymbol{\omega}$ equal to $\omega_0\hat{\mathbf{k}}$, then the effective field in the rotating system becomes

$$\mathbf{H}_e = \left(H_z - \frac{\omega_0}{\gamma}\right)\hat{\mathbf{k}} + H_1\hat{\mathbf{i}}'. \tag{4.4}$$

The ^{3}He average magnetic moment, $< \mathbf{M} >$, aligns itself with the effective field.

During AFP, the holding field changes in value such that it passes through the value $|\frac{\omega_0}{\gamma}|$. The angle that $< \mathbf{M} >$ makes with the z-axis increases until $H_z = \frac{\omega_0}{\gamma}$ and the spins are at an angle of 90° (Figure 4.1). For our conditions $\omega_0 = 2\pi f$, where f=91 kHz, and γ for ^{3}He is $-20378 s^{-1}G^{-1}$ making $|\frac{\omega_0}{\gamma}| = 28.06G$. When this resonance condition is met, the ^{3}He average magnetic moment induces an EMF signal in the pickup coils located on both sides of the target chamber. As the holding field increases in value beyond $|\frac{\omega_0}{\gamma}|$, the spins end up pointing in the opposite direction. This process is called a spin flip.

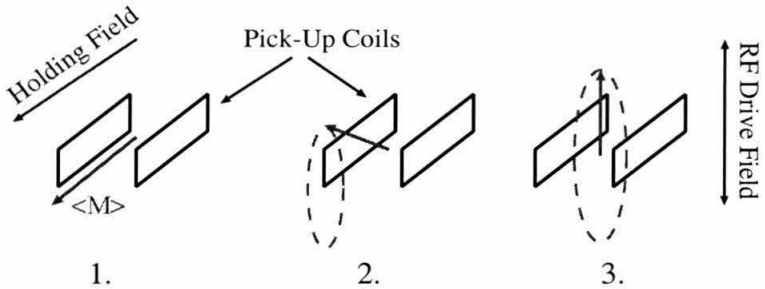

Figure 4.1: The process of an AFP-NMR spin flip. 1) Initially the spins are aligned with the holding field. 2) A 91 kHz RF field is applied, and the magnetic moment of the ^{3}He begins to precess about the z axis as the holding field moves towards 28.06 G. 3) When the holding field is at 28.06 G the ^{3}He spins are rotating perpendicular to the z-axis, an EMF signal is induced in the pickup coils.

Measurements of the ^{3}He polarization was done by scanning the holding field from 25 to 32 G and back, at a rate of 1.2 G/s. This procedure results in two spin flips, inducing an EMF signal twice. The signal size is proportional to the transverse

component of the magnetization:

$$S_{He}^{nmr}(t) \propto \frac{< \mathbf{M} > H_1}{\sqrt{(H_z(t) + \frac{\omega_0}{\gamma})^2 + H_1^2}}, \tag{4.5}$$

where

$$< \mathbf{M} >= P_{He}\mu_{He}[^3\mathrm{He}]. \tag{4.6}$$

An example of a NMR signal can be seen in Figure 4.2. Signals were fitted to Eq. 4.5, plus a slope and constant: $m \cdot H_z(t) + C$. It is the fitted amplitude that is considered to be proportional to the polarization.

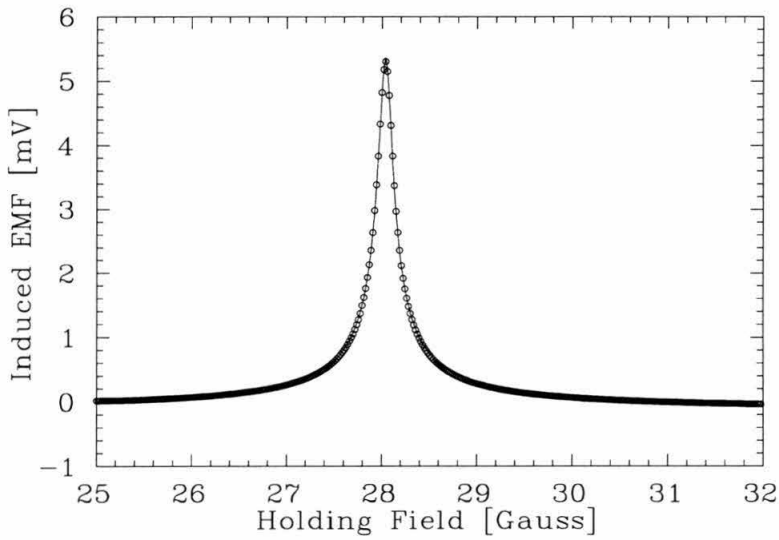

Figure 4.2: A NMR signal.

The condition for adiabatic fast passage is met when:

$$\frac{D|\nabla H_z|^2}{H_1^2} \ll \frac{\dot{H}_z}{H_1} \ll \omega_0, \tag{4.7}$$

where D is the ^{3}He diffusion rate. The holding field rate of change must be slow enough that the spins can follow adiabatically and fast enough that spin relaxation

at resonance is minimal. For our conditions, both considerations were easily met:

$$\frac{D|\nabla H_z|^2}{H_1^2} \approx 10^{-2}[s^{-1}] \ll \frac{\dot{H}_z}{H_1} = 24[s^{-1}] \ll \omega_0 = 9.1 \times 10^4[s^{-1}]. \tag{4.8}$$

4.2 Calibration

In order to extract a polarization value for the ^{3}He, the NMR system needed to be calibrated. This was done by placing a substance with a known polarization between the pickup coils, taking a NMR measurement, and calculating a constant of proportionality, κ, between signal height and polarization. This constant can then be used to extract the polarization of ^{3}He:

$$S_{He} = \kappa P_{He}. \tag{4.9}$$

The constant of proportionality depends on several factors. Some of the factors (e.g., position and density) depend on which target cell is being used. The other factors are independent of the target cell and measure the NMR system's responsiveness, or amount of signal seen for a given spin. Therefore, the calibration constant κ for each cell is a product of two parts:

$$\kappa_{cell} = \kappa^* \underbrace{\Phi_{He} G_{He}^{Q} n_o \left(\frac{n_c}{n_o}\right)}_{\text{cell dependent}}, \tag{4.10}$$

where κ^* is the responsiveness of the system, Φ_{He} is the geometrical flux produced by a particular cell, and G_{He}^{Q} is a measure of the LRC circuit's gain at the time of the measurement. The purpose of calibration is to determine κ^*.

Two methods were used to calibrate the NMR system. The first method relied on the thermally polarized protons contained in water. Their polarization is given by

the Boltzmann distribution:

$$P_w^{th} = \tanh \frac{\mu_p B}{kT} \approx 7 \times 10^{-9}, \tag{4.11}$$

where μ_p is the magnetic moment of the proton, B is the magnetic field, k is Boltzmann's constant, and T is the temperature. The second method used the polarization of ^{3}He as determined by the electron paramagnetic resonance signal coming from polarized Rb [65].

4.2.1 The Calibration Constant κ_w^*

For the water calibration, a water cell with the same geometry as a helium cell was filled with de-oxygenated, de-ionized water. This cell was mounted in the same setup as the helium cells, and a NMR measurement was taken. The thermal polarization of the protons in the water at room temperature and at the field strength used during the experiment is quite low (Eq. 4.11). Typically 100 to 300 NMR sweeps were taken and averaged. Once a water signal was obtained, a fit was performed to determine the amplitude: S_w. With the water signal, the calculated thermal polarization, and a number of other factors, the calibration factor κ_w^* can be found. The calibration becomes:

$$\kappa_w^* = \frac{S_w}{P_w^{th}} \cdot \frac{\mu_{He}}{\mu_p} \cdot \frac{G_{He}^{pre}}{G_w^{pre}} \cdot \frac{1}{G_w^Q} \cdot \frac{1}{\Phi_w} \cdot \frac{1}{n_p} \cdot C_{\frac{\delta H}{H}} \cdot C_{cover}, \tag{4.12}$$

where $G_{He,w}^{pre}$ are the settings for the preamplifier, n_p is the number density of the protons (2482 amg.), and $C_{\frac{\delta H}{H}}$ and C_{cover} are slight correction factors to the water signal. Details of these various parameters for κ_w^* are discussed below.

4.2.2 Water Signal and Thermal Polarization

There are two challenging aspects of using water as a calibration medium. One is that the thermal polarization present depends on the holding field strength, which

changes between 18 and 25 Gauss. The other complication is that the proton spins in water tend to relax away from the direction of the effective field, H_{eff}, towards the direction of the holding field, H_z. This relaxation process can be described by [63]

$$\frac{dM_z}{dt} = -(M_z - < \mathbf{M} >)/T_1, \tag{4.13}$$

where M_z is the component of the average magnetic moment,$< \mathbf{M} >$, in the z-direction and T_1 is the longitudinal relaxation time. For protons in water, T_1 is on the order of a couple of seconds. The proton polarization increases as the field changes from 18 to 25 Gauss and loses polarization as the angle between H_{eff} and H_z increases. By the time the field reaches 25 Gauss, all of the spins have relaxed back toward the holding field direction. This does not occur for ^{3}He because the relaxation time is on the order of 10^5 seconds. As the field sweeps back down from 25 to 18 Gauss, the spins will again go through resonance but this time starting with a higher polarization.

In order to understand the amount of thermal polarization at the moment that the spins are at resonance, we use the Bloch equations. These equations describe the three components of the polarization in the rotating reference frame: x', y', and z':

$$\begin{aligned}
\frac{dP_{x'}}{dt} &= \gamma P_{y'}(H_z(t) - \frac{\omega}{\gamma}) - \frac{P_{x'} - \chi H_1}{T_2}, & (4.14)\\
\frac{dP_{y'}}{dt} &= -\gamma P_{x'}(H_z(t) - \frac{\omega}{\gamma}) + \gamma P_{z'} H_1 - \frac{P_{y'}}{T_2}, & (4.15)\\
\frac{dP_{z'}}{dt} &= -\gamma P_{y'} H_1 - \frac{P_{z'} - \chi H_z(t)}{T_1}, & (4.16)\\
H_z(t) &= \frac{\omega}{\gamma} + \alpha t, & (4.17)
\end{aligned}$$

where α is the sweep rate of the holding field (1.2 G s^{-1}), T_2 is the transverse relaxation time, H_1 is the value of the RF field (90.8±0.5 mG), ω is the radial frequency of the RF field ($2\pi f$, f=91kHz), χ is the magnetic susceptibility ($3.4616 \pm 0.0117 \times 10^{-10}$ G^{-1} at 22°), and γ is the gyromagnetic ratio of the proton (2.6752×10^4 s^{-1} G^{-1}).

The Bloch equations do not have an analytic solution. However, the equations can be solved numerically in order to determine the shape and behavior of the resonance signal under different conditions. It was found that T_2 did not significantly effect the shape of the signal but did effect the height. If, for the purpose of creating an analytic solution, we set $T_1 = T_2$ and assume that under adiabatic conditions the polarization follows the effective field ($H_{eff} = (H(t) - \omega/\gamma)\hat{k} + H_1\hat{i}$) in the rotating coordinate system, then the Bloch equations can be reduced to one equation for $P_{eff} = \sqrt{P_x^2 + P_y^2 + P_z^2}$:

$$\frac{dP_{eff}}{dt} = \frac{1}{T_1}(P_{eq}(t) - P_{eff}) \tag{4.18}$$

where

$$P_{eq} = \chi \left(\frac{H(t)(H(t) - \frac{\omega}{\gamma}) + H_1^2}{\sqrt{H_1^2 + (H(t) - \frac{\omega}{\gamma})^2}} \right). \tag{4.19}$$

The integral solution is given by:

$$P(t) = e^{-(t-t_0)/T_1} \left(P(t_0) + \frac{1}{T_1} \int_{t_0}^{t} e^{(t'-t_0)/T_1} P_{eq}(t') dt' \right). \tag{4.20}$$

By expanding the exponential and the denominator of P_{eq} to first order in t', the integral can be solved. This will yield an approximate analytic solution to the Bloch equations. Comparison of the approximate solution to the integral solution showed agreement within 0.4% of the peak height everywhere along the curve. The analytic solution allows one to fit the water signal in order to determine the signal height. The thermal polarization detected at any time is given by P_x; therefore, P_{th} is just equal to the maximum value of P_x.

Three water signals were taken during the experiment. They were conducted on the following dates: Sept. 25th, Nov. 3rd, and Nov. 25th. The experiment collected data from Sept. 26th to Dec. 24th, 1998.

Figure 4.3 shows the water signal taken on Sept. 25th. The *UP* and *DOWN* sweeps

are each comprised of 373 points, each one of which represents the EMF pickup from the coils at that particular holding field value. The uncertainty assigned to each point comes from the standard deviation of the values recorded for that particular field. Also, shown in Figure 4.3 are the fits to the *UP* and *DOWN* sweeps. The fitting function is the analytical solution to the Bloch equations where $T_1 = T_2 = 2.95$ s [66]. The uncertainty in the fitted amplitude is taken to be less than 2%.

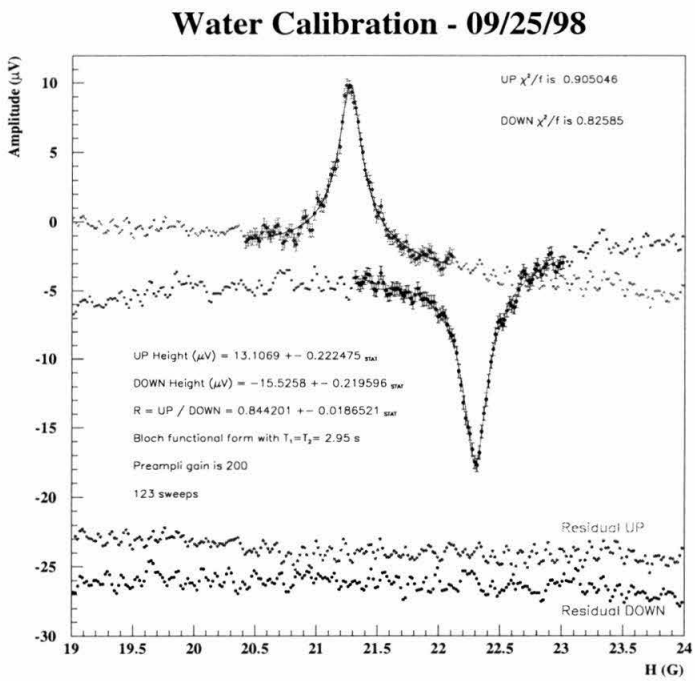

Figure 4.3: The fit to the *UP* and *DOWN* sweeps for the water signal taken on 9/25/98. The position of the resonance for the *DOWN* sweep has been shifted in this plot.

To find a value of T_1 for de-oxygenated, de-ionized water, the ratio of the *UP* and *DOWN* sweep amplitudes was studied. Their ratio, $R = S_w^{UP} / S_w^{DOWN}$, has a strong T_1 dependence. An initial T_1 was chosen, the *UP* and *DOWN* water signals were fitted, the ratio calculated, and a new T_1 was predicted. This new T_1 was then plugged into the analytic solution and the *UP* and *DOWN* signals were re-fitted predicting T_1 again.

The process is repeated until the predicted T_1 matches the initial T_1 used. By taking the weighted average of the ratio from the three water signals, it was found that

$$R = 0.839 \pm 0.010, \tag{4.21}$$

which leads to a value for T_1 of

$$T_1 = 3.0 \pm 0.4s. \tag{4.22}$$

This value is in good agreement with the world value for de-oxygenated water of $T_1 = 2.95s$ [66] at $20°C$. The value of T_2 is related to the value of T_1 [67]: $\frac{1}{T_1} - \frac{1}{T_2} = 0.125s^{-1}$. If we assume that T_1 and T_2 are 100% correlated, and for a RF field, H_1, of 90.8 ± 0.5 mG, then

$$T_2 = 2.7 \pm 0.4s. \tag{4.23}$$

The analytical equation that is used to determine S_w assumes that $T_1 = T_2$. The fact that T_1 does not equal T_2 causes the fitted amplitude to be decreased by a small amount. By solving the Bloch equations numerically and comparing to the case when $T_1 = T_2$, it was determined that the *UP* and *DOWN* thermal polarizations needed to be corrected up by 0.36% and 0.21% respectively with negligible uncertainty.

The calculated thermal polarizations at the moment when resonance occurs is

$$P^{th}_{UP} = 6.415 \times 10^{-9} \qquad \text{and} \qquad P^{th}_{DOWN} = 7.655 \times 10^{-9}. \tag{4.24}$$

The total uncertainty (Table 4.2.2) on these polarizations comes mainly from the uncertainty in the initial and maximum value of the holding field during a sweep.

The fitted amplitudes to the three water calibrations are listed in Table 4.2. For the purposes of calculating κ_w, the fitted amplitudes for *UP* and *DOWN* sweeps will be divided by their corresponding thermal polarizations and then averaged, yielding just one value of S_w/P^{th}_w for each water calibration. This value, divided by the gain

Parameter	T_1	Initial Field	Integration	Temperature	Total
Value	3.0 ± 0.4 s	$18(25) \pm 0.5$ G		22 ± 1°C	
Uncertainty	0.3%	1.1%	0.5%	0.3%	1.3%

Table 4.1: Systematic uncertainties on P_w^{th}.

of the preamplifier, is listed as *ave* in Table 4.2.

sweep direction	Date of water calibration		
	9/25/98	11/3/98	11/25/98
UP (μV)	13.11±0.22	6.48±0.12	66.85±0.89
DOWN (μV)	15.52±0.22	7.83±0.13	79.54±0.93
R	0.845 ± 0.019	0.828 ± 0.021	0.840 ± 0.015
G_w^{pre}	200	100	1000
# of sweeps	123	271	213
ave [mV/%]	101.9±1.1	102.1±1.3	104.5±0.9

Table 4.2: Fitted values for S_w with systematic uncertainties (μV) and the average of S_w/P_w^{th} for each water calibration divided by G_w^{pre}.

4.2.3 Corrections to the Water Signal

By comparing the resonance position of groups of 50 water sweeps, it was found that the initial and maximum holding field values drift at a rate of $\delta H/H = 0.001 hr^{-1}$. Because the computer assumes that the sweep always starts and stops at the same value, the signal is slightly broadened, and the peak height is reduced. In order to model this effect, a number of Lorentzian lines shapes were generated with their resonance positions shifted by an amount corresponding to the field drift. The Lorentzian line shapes were averaged and then fitted. The fitted height estimates the reduction in the amplitude due to the field drift. The amount of the correction necessary for each water signal is listed in Table 4.3. The assigned systematic uncertainty in the correction is taken to be ±0.2%.

During the experiment, the RF Helmholtz coils were surrounded by an aluminum

Date	9/25/98	11/3/98	11/25/98
# of sweeps	123	271	213
$C_{\frac{\delta H}{H}}$	1.0035	1.0156	1.0099

Table 4.3: Values for $C_{\frac{\delta H}{H}}$.

sheet. This cover was not in place when a water signal was measured. Two tests were conducted with different target cells and at different polarization values. In both cases the lasers were turned off. Table 4.4 lists the NMR values and time recorded during each test, as well as the apparent rate of depolarization and the effect of the cover being off. Both tests found that the effect of the cover off was to increase the signal by 1.7%. To correct the water signal $C_{cover} = 0.983$. By assuming different loss mechanisms and seeing the effect on C_{cover}, a systematic uncertainty of 0.3% was determined.

Cell: *Blue*			Cell: *Jin*		
cover	NMR[mV]	Δt[s]	cover	NMR[mV]	Δt[s]
on	2.37	0	on	9.15	0
off	2.34	11	off	9.20	12
off	2.16	40	on	8.93	25
Depolarization rate [μV/sec.]					
6.2				8.8	
Effect on signal height [%]					
1.7				1.7	

Table 4.4: Results of tests for C_{cover}.

4.2.4 Cell Position and Flux

The amount of voltage produced in the pickup coils depends on four factors: the rate of spin precession (ω_o), the density of spins, the polarization, and the position of the target cell (Figure 4.4). The geometrical flux, Φ, is the number of magnetic field lines that pass through the pickup coils when the spins are on resonance. The contribution

to Φ was calculated for each chamber using

$$\Phi = \oint_C \int_V \frac{\vec{m} \wedge \vec{r}}{\vec{r}^3} \vec{dl} dV. \tag{4.25}$$

Here, $\vec{m}$ is the density of magnetization for the target. It will be considered unit-less and therefore Φ will have the units of cm^2. The volume of a chamber is given by V, and the coil boundary is C. The target cell pumping chamber contribution to the flux was weighted by $\frac{(n_p/n_o)}{(n_c/n_o)}$ to reflect the fact that the density is not uniform. The total flux for each water signal was determined (Table 4.5), and studies of the dependence of the flux on cell position were done using Eq. 4.25.

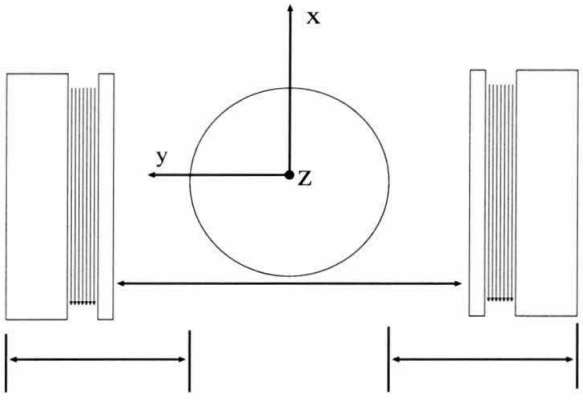

Figure 4.4: Positioning of the target chamber between the pickup coils.

The uncertainty in the amount of geometrical flux associated with each cell comes from two primary sources: the position of the cell in the y-direction and inner radius of the target chamber. Each time a cell was mounted, its position relative to the pickup coils was measured using a caliper. The uncertainty from this type of measurement is about ± 1.5 mm. This contributes an uncertainty of 1.0% to the total flux. The contributions from the uncertainty in the pickup coils in the x and z-directions, along with tilting and rotations, are all less than $\pm 0.3\%$. The inner radius of the target chamber is known to ± 0.05 mm. This leads to an uncertainty in the flux of $\pm 1.7\%$. The total uncertainty in the flux is assigned to be $\pm 2.1\%$ for all

Calibration date or Helium cell	Flux of each part (cm)			$\Phi_{He,w}$
	Target	**Pump**	**Transfer**	**Total**
9/25/98	46.33	-3.90	0.04	42.47
11/3/98	49.60	-3.92	-0.06	45.61
11/25/98	49.78	-3.92	-0.08	45.79
Don't Worry	44.31	-2.57	0.11	41.85
Be Happy	45.87	-3.28	0.10	42.69
Armageddon	44.32	-2.36	0.06	42.02
Nepheli	47.91	-2.50	0.01	45.42
Sysiphos	49.23	-2.58	0.04	46.69
Jin	47.71	-2.43	0.02	45.30

Table 4.5: The flux, Φ, for each water calibration and for each ^{3}He cell.

cells except *Armageddon*. The position of *Armageddon* was not recorded. Therefore, its flux uncertainty is derived from assuming that the cell could be anywhere along the y-direction and is set at $\pm 3.4\%$.

4.2.5 Coil Gain

One consequence of having target cells filled to 10 atmospheres is that they can explode. When this happens the explosions cause small changes in the gain of the LRC circuit. In order to monitor this effect, a small excitation coil was fixed within the RF Helmholtz coils. A RF signal was sent to the excitation coil which created a response in the pickup coils. By changing the frequency of the excitation coil, the pickup coils' Q-curve, or response curve, could be mapped out. The voltage induced in the pickup coils as a function of frequency, f, is given by:

$$V(f) = \frac{Af}{\sqrt{\frac{1}{Q^2}\frac{f^2}{f_0^2} + \left(\frac{f^2}{f_0^2} - 1\right)^2}}. \tag{4.26}$$

The numerator, Af, is the induced EMF. 'A' depends on geometric factors and the amplitude of the signal that drives the excitation loop. The parameters A,

f_0, and Q are determined by fitting the data to equation 4.26. G^Q is defined by $V(f = 91kHz)/(A \cdot 91kHz)$. The results of the calculated gain agree closely with one another (Figure 4.5).

It appears (Figure 4.5) that following *Armageddon* and *Nepheli*'s explosions there was a change in the Q-curve. The values of G^Q for the water signals taken on 9/25/98, 11/3/98, and 11/25/98 are 1.265, 1.260, and 1.255 respectively. For the target cells, G^Q is 1.265 for *Don't Worry*, *Be Happy*, and *Armageddon*, 1.260 for *Nepheli*, and 1.255 for *Sysiphos* and *Jin*.

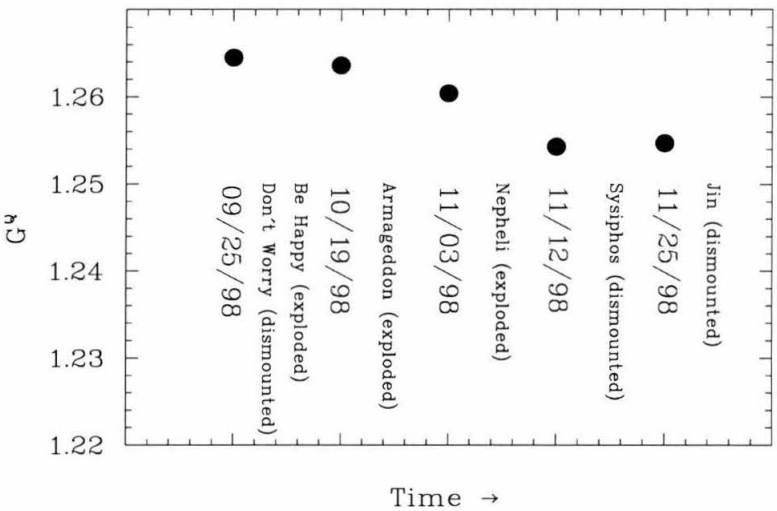

Figure 4.5: The value of G^Q as a function of time.

4.2.6 Calculation of κ_w^*

Recall that the water calibration constant κ_w^* is given by Eq. 4.12:

$$\kappa_w^* = \frac{S_w}{P_w^{th}} \cdot \frac{\mu_{He}}{\mu_p} \cdot \frac{G_{He}^{pre}}{G_w^{pre}} \cdot \frac{1}{G_w^Q} \cdot \frac{1}{\Phi_w} \cdot \frac{1}{n_p} \cdot C_{\frac{\delta H}{H}} \cdot C_{cover}.$$

The three water signal's *UP* and *DOWN* sweeps yield six measurements of κ_w^*. By combining the *UP* and *DOWN* S_w/P_w^{th} ratios, there will be only one κ_w^* for each

water signal. These three κ_w^* are then averaged. Table 4.6 lists the input values for Eq. 4.12 and Figure 4.6 shows the results.

Parameter	Value	Uncertainty (%)
(S_w^{up}, S_w^{down})	(13.1,15.5), (6.48,7.83), (66.9,79.5) μV	1.3
P_w^{th}	6.415, 7.655 ($\times 10^{-9}$)	1.3
μ_{He}/μ_p	0.762	-
n_p	2482 amg.	0.1
G_{He}^{pre}/G_w^{pre}	1/200, 1/100, 1/1000	0.5
G_w^Q	1.2645, 1.2604, 1.2547	-
Φ_w	43.0, 46.2, 46.4 cm^2	2.1
$C_{\frac{\delta H}{H}}$	1.0035, 1.0156, 1.0099	0.2
C_{cover}	0.983	0.3
Total:κ_w^*	5.56×10^{-4} $\left[\frac{mV}{\%\cdot amg.\cdot cm^2\cdot Q-gain}\right]$	2.3

Table 4.6: The values for the parameters that go into calculating κ_w^* and their uncertainties.

The uncertainty on each point in Figure 4.6 is derived from those listed in Table 4.6. An estimate of the total systematic uncertainty on κ_w^* was calculated by considering the correlated and uncorrelated portions seperately:

$$\sigma_{(\kappa_w^*)} = \sqrt{\frac{1}{3}(\sigma^2_{(S_w)} + \sigma^2_{(P_w^{th})} + \sigma^2_{(G^{pre})} + \sigma^2_{(\Phi_w^{pos})} + \sigma^2_{(C_{\frac{\delta H}{H}})}) + \sigma^2_{(n_p)} + \sigma^2_{(\Phi_w^{rad})} + \sigma^2_{(C_{cover})}}. \tag{4.27}$$

The flux uncertainty was broken up into two parts: the uncorrelated uncertainty due to the position (1.2%) and the correlated uncertainty due to the inner radius (1.7%). The total uncertainty on the average of the three water signals is estimated to be $\pm$2.3%. This uncertainty is similar to the one determined for the SLAC E154 experiment [50]. The value for κ_w^* is

$$\kappa_w^* = 5.56 \times 10^{-4} \left[\frac{\text{mV}}{\%\ \text{amg cm}^2\ \text{Q}}\right]. \tag{4.28}$$

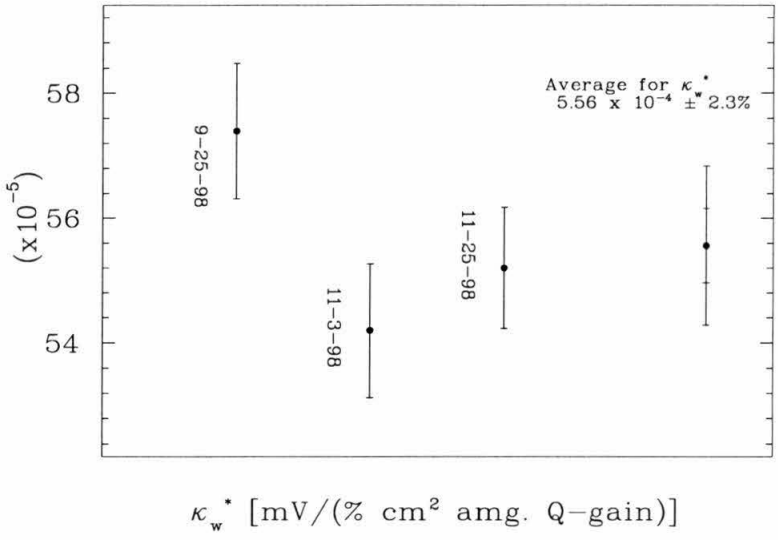

Figure 4.6: The value of κ_w^* for the three water signals.

4.2.7 The Calibration Constant κ^*_{epr}

The second method by which the NMR system was calibrated was to measure the separation of the ^{85}Rb $(F = 3, m = -3)$ and $(F = 3, m = -2)$ energy levels (Figure 3.1), or electron paramagnetic resonance (EPR). This separation, $\Delta\nu$, is proportional to the ^{3}He polarization in the pumping chamber: P_{He}^{pump}. The pumping chamber polarization is in turn related to the polarization measured by the NMR system: P_{He}^{targ}. Just as in the case of water, a NMR signal related to a known polarization allows for the calculation of κ^* as presented in Eq. 4.10. Explicitly, κ^*_{epr} is given as

$$\kappa^*_{epr} = \frac{S'_{He}}{P_{He}^{targ}} \cdot \frac{1}{G'^{Q}_{He} \cdot \Phi'_{He} \cdot n'_o \left(\frac{n'_c}{n'_o}\right)}. \tag{4.29}$$

Here, the prime indicates the quantities for the particular cell used during the calibration and P_{He}^{pump} is related to the EPR measurement.

There are three factors that account for the separation in energy levels: the holding field, the magnetic field caused by polarized ^{3}He, and the spin exchange of Rb-^{3}He.

The amount of separation caused by the magnetic field of the ^{3}He is proportional to its magnetization, M_{He} : $B_{He} = \frac{8\pi}{3} M_{He}$. The separation created by this field is small in comparison to the separation created by the holding field (≈11 GHz for 25 Gauss). Therefore, the ^{3}He magnetic field shift can be related to the derivative of the EPR frequency, $\nu(F,m)$, of the $(F, m \rightarrow F, m-1)$ transition:

$$\Delta\nu_M = \frac{d\nu(F,m)}{dB}\frac{8\pi}{3}M_{He} = \frac{d\nu(F,m)}{dB}\frac{8\pi}{3}[He]\mu_{He}P_{He}, \tag{4.30}$$

where $[He]$ is the ^{3}He number density, μ_{He} is the ^{3}He magnetic moment, and P_{He} is the amount of ^{3}He polarization. The spin exchange of Rb-^{3}He also creates a separation that is equivalent to an additional magnetic field:

$$B_{SE} = \frac{2\hbar K_{SE}\Gamma_{SE}}{g_e\mu_B}K_z, \tag{4.31}$$

where K_{SE} is the ratio of the imaginary and real parts of the spin-exchange cross section, $< v\sigma_{SE} >$ is the velocity averaged real part of the cross section, $g = 2$ for the electron, μ_B is the Bohr magneton, and K is the ^{3}He nuclear spin. Again, the separation created by B_{SE} is related to the derivative: $\Delta\nu = \frac{d\nu(F,m)}{dB}B_{SE}$.

The total separation of the $(F = 3, m = -3)$ and $(F = 3, m = -2)$ sublevels due to the polarized ^{3}He is

$$\Delta\nu = \Delta\nu_{SE} + \Delta\nu_M = \frac{8\pi}{3}\frac{d\nu(F,m)}{dB}\kappa_o\mu_{He}[He]P_{He}, \tag{4.32}$$

where κ_o is related to the spin-exchange cross section and does not depend on the ^{3}He density or polarization. It is normalized such that if only the magnetic field created by the polarized ^{3}He were considered, κ_o would equal one. However, $\kappa_o \approx 6$, which implies that there is an attraction between the Rb electron wavefunction and the ^{3}He

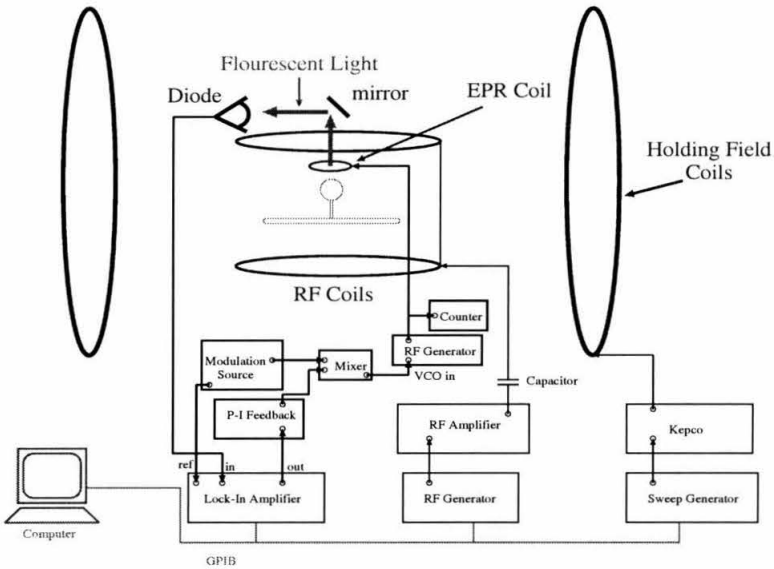

Figure 4.7: A schematic of the EPR electrons setup.

nucleus. The constant κ_o was measured explicitly by [65] and is known to $\pm 1.5\%$:

$$\kappa_o = 4.52 + 0.00934 \cdot T(^\circ\mathrm{C}). \tag{4.33}$$

The derivative of the EPR frequency $\left(\frac{d\nu(F,m)}{dB}\right)$ for the $(F = 3, m = -3 \rightarrow F = 3, m = -2)$ transition is given by the Breit-Rabi equation [68]:

$$\frac{dv(F,m)}{dB} = \frac{\mu_B g_e}{h(2I+1)}\left(1 + \frac{8I}{(2I+1)^2}\frac{\mu_B g_e B}{hA}\right), \tag{4.34}$$

where $I = 5/2$ and $A = 1012$ MHz for ^{85}Rb. Substituting Eq. 4.34 into Eq. 4.32, the ^{3}He polarization can be written as

$$P_{He}^{pump} = 0.852\left[\frac{\text{amg.}}{\text{kHz}}\right]\frac{\Delta\nu}{\kappa_o n_o'\left(\frac{n_p'}{n_o'}\right)}. \tag{4.35}$$

4.2.8 EPR System

Measurement of the EPR shift, $\Delta\nu$, was performed by observing the D2 fluorescent light emitted by decaying rubidium. This fluorescent light was observed with a photodiode (Figure 4.7). The intensity of the fluorescence is inversely proportional to the amount of Rb polarization. This is because only atoms that are not polarized can be excited and then give off a photon. By inducing the transition of the rubidium's outer electron from the $(F = 3, m_F = -3)$ state (a non excitable state) to the $(F = 3, m_F = -2)$ state (an excitable state) with a small coil located above the pumping chamber (EPR coil), the amount of optical pumping will increase and therefore the amount of fluorescence. The frequency of the $m_F = -3 \rightarrow -2$ transition is proportional to the holding field plus the field created by the polarized ^{3}He.

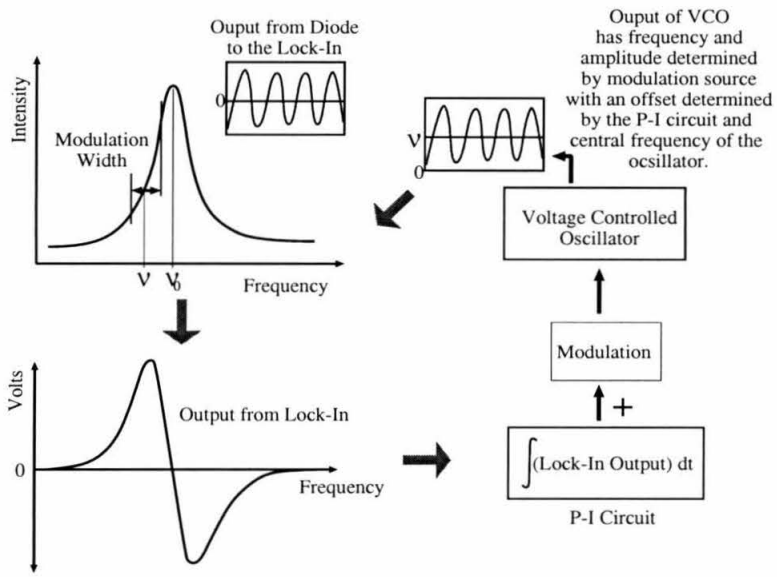

Figure 4.8: The feedback mechanism for the EPR setup.

It was necessary to lock onto the EPR resonance because of drifts in the holding field. This was done by using a feedback mechanism (Figure 4.8). The driving frequency for the EPR coil was modulated by 6 kHz at a frequency of 200 Hz. This in turn swept out a portion of the intensity spectrum which created a sine wave whose

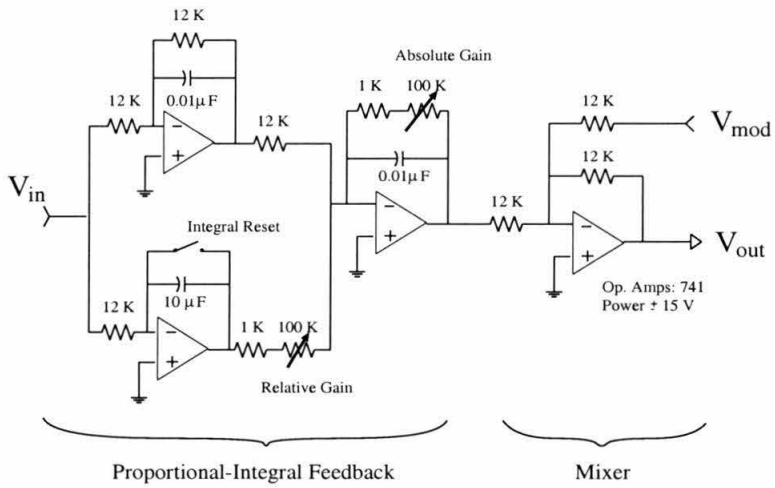

Figure 4.9: Circuit diagram for the proportional-integral feedback and the mixer.

amplitude depended on the value of the central driving signal (ν) in relation to the resonance frequency (ν_o). The output of diode was read by the lock-in amplifier. The lock-in output was proportional to the amplitude of the sine wave; it was zero on and far off resonance. The output of the lock-in was integrated and mixed with a modulation signal using a P-I/Mixer circuit (Figure 4.9). This signal was then sent into the *Wavetek Model 80* Voltage Controlled Oscillator (VCO) whose output was a sine wave with a central frequency determined by the value set on the device and the integral of the lock-in. This frequency was varied by the modulation source and was used to drive the EPR coil. As an example, assume that the frequency ν is less than ν_o. The lock-in detects a sine wave and outputs a positive signal which is then integrated. The positive signal from the P-I feedback box, along with the modulation signal, is inputed into the VCO and causes the signal to shift to a higher frequency. The frequency ν is now closer to ν_o. It was in this way that the feedback mechanism moved and kept the central frequency ν at the same value of the resonance frequency ν_o.

In order to isolate the shift contribution related to the polarized ^{3}He, a measurement was first done with the spins in one direction and then reversed (Figure 4.10).

The flip was performed using AFP, by changing the RF field to induce the transition.

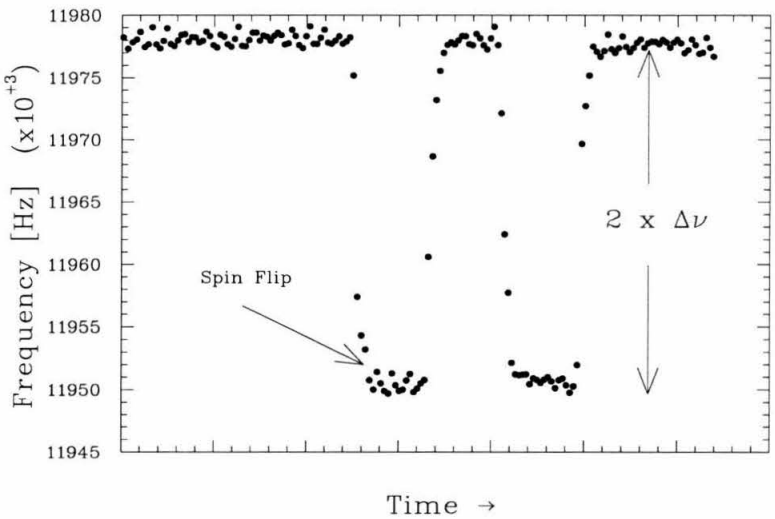

Figure 4.10: An EPR measurement showing the change in resonance frequency due to the ^{3}He spins being flipped.

4.2.9 Polarization Gradient

If the target cell (Figure 3.3) were comprised of only one chamber, then a direct comparison between the EPR shift and a NMR signal could be made. However, with a two chamber cell the ^{3}He polarization originates in the pumping (top) chamber and diffuses down into the target (bottom) chamber. In order to relate an EPR measurement to a NMR measurement, understanding of this transfer of polarization is necessary.

The flux of ^{3}He atoms, with desired spin direction, along the transfer tube is given by

$$\mathcal{J}(z) = \frac{1}{2} n(z) D(z) \frac{dP}{dz} = \text{constant}, \tag{4.36}$$

where $n(z)$ is the number density along the transfer tube, $D(z)$ is the diffusion coefficient, and P is the amount of polarization. The diffusion coefficient at 1 atm. and

80°C is 2.76 cm^2/s [69]. This is related to $D(z)$ by the following relation:

$$D(z) = 2.76[cm^2/s]\frac{0.773amg.}{n(z)}\left(\frac{T(z)}{353°K}\right)^{m-1}, \tag{4.37}$$

where $m = 1.7$ [69]. The temperature distribution, $T(z)$, along the transfer tube is $T(z) = T_t + \frac{T_p - T_t}{L_{tran}}(z + \frac{L_{tran}}{2})$. By integrating Eq. 4.36 along the length of the transfer tube, the polarization flux can be expressed in terms of the pumping and target chamber polarizations:

$$\mathcal{J} = \frac{D_t n_t K}{2L_{tran}}(P^{pump} - P^{targ}). \tag{4.38}$$

Here, D_t is the diffusion coefficient at the target chamber and $K = \frac{(2-m)(T_p - T_t)T_t^{1-m}}{T_p^{2-m} - T_t^{2-m}}$.

Knowing the polarization flux, the time rate-of-change for each chamber is given by:

$$\frac{dP^{pump}}{dt} = -G_p(P^{pump} - P^{targ}) \qquad \text{and} \qquad \frac{dP^{targ}}{dt} = -G_t(P^{targ} - P^{pump}), \tag{4.39}$$

where

$$G_p = \frac{A_{tran}n_t}{V_p L_{tran} n_p} D_t K \qquad \text{and} \qquad G_t = \frac{A_{tran}}{V_p L_{tran}} D_t K. \tag{4.40}$$

However, even these equations are not enough to describe the polarization in each chamber, for they only describe the diffusion of the gas from one chamber to the next. For a complete description of the polarization the effects of spin exchange and depolarization need to be included. The complete rate equations for the polarization in terms of the cell lifetime, Γ, and the spin exchange rate, γ_{SE}, are

$$\frac{dP^{pump}}{dt} = -G_p(P^{pump} - P^{targ}) + \gamma_{SE} < P_{Rb} > -(\gamma_{SE} + \Gamma)P^{pump} \tag{4.41}$$

$$\frac{dP^{targ}}{dt} = -G_t(P^{targ} - P^{pump}) + \Gamma P^{targ}. \tag{4.42}$$

The solution to this set of coupled equations is

$$P^{pump,targ}(t) = A_1^{pump,targ} e^{-\gamma_{slow} t} + A_2^{pump,targ} e^{-\gamma_{fast} t} + P_\infty^{pump,targ}, \tag{4.43}$$

where $A_{1,2}$ are constants and $P_\infty^{pump,targ}$ are the saturation polarizations given by

$$P_\infty^{pump} = \frac{\gamma_{SE}}{G_p + \gamma_{SE} + \Gamma + \frac{G_p G_t}{\Gamma + G_t}} < P_{Rb} > \qquad \text{and} \qquad P_\infty^{targ} = \frac{G_t}{\Gamma + G_t} P_\infty^{pump}. \tag{4.44}$$

The term that goes like $e^{-\gamma_{fast} t}$ in Eq. 4.43 vanishes and can be neglected. Solving for $e^{-\gamma_{slow} t}$, a linear relation between the target and pumping chamber polarizations is formed:

$$P^{targ} = \alpha_1 P^{pump} + \alpha_2, \tag{4.45}$$

where

$$\alpha_1 = \frac{\gamma_{fast} P_\infty^{targ}}{\gamma_{fast} P_\infty^{pump} - \gamma_{SE} < P_{Rb} >}, \tag{4.46}$$

$$\alpha_2 = P_\infty^{targ} \left(1 - \frac{\gamma_{fast} P_\infty^{targ}}{\gamma_{fast} P_\infty^{pump} - \gamma_{SE} < P_{Rb} >} \right), \tag{4.47}$$

and

$$\gamma_{fast} = \frac{1}{2} \left[G_t + G_p + 2\Gamma + \gamma_{SE} + \sqrt{(G_t - G_p - \gamma_{SE})^2 + 4 G_p G_t} \right]. \tag{4.48}$$

The polarization of the target chamber, P_{He}^{targ}, can now be calculated from the EPR shift using Eqs. 4.45 and 4.35. The difference in pumping and target chamber polarizations, ΔP, were typically ~1% (Table 4.7).

4.2.10 Calculation of κ_{epr}^*

In order for Eq. 4.45 to be valid, the pumping system (e.g., number of lasers on, temperature, etc.) has to be stable. Nine EPR calibrations were done during the experiment using four different cells (Figure 4.11). Parameters for each calibration

#	Cell	$\Delta\nu$ [kHz]	$S'_{He}[mV]$	$\left(\frac{n'_c}{n'_o}\right)$	$\left(\frac{n'_p}{n'_o}\right)$	ΔP [%]	κ^*_{epr} [$\times 10^{-4}$]
1	*Don't Worry*	8.15	4.26	1.112	0.919	0.03	5.46
2	*Nepheli*	11.77	6.37	1.214	0.808	1.26	5.22
3	*Nepheli*	13.74	8.01	1.215	0.807	1.24	5.54
4	*Nepheli*	16.64	9.57	1.213	0.810	1.13	5.40
5	*Sysiphos*	14.02	8.80	1.209	0.808	1.03	5.70
6	*Jin*	16.70	10.10	1.159	0.826	0.50	5.89
7	*Jin*	17.11	11.76	1.223	0.786	0.87	6.19
8	*Jin*	18.03	11.64	1.209	0.801	0.77	5.95
9	*Jin*	13.24	8.08	1.166	0.818	0.97	6.08

Table 4.7: Conditions for the nine EPR calibrations. ΔP is the difference between the pumping and target chamber polarizations.

are listed in Table 4.7.

The calculation of two new parameters, $< P_{Rb} >$ and γ_{SE} (Eq. 4.41), were needed to complete the EPR calibration. The spin exchange rate for Rb-^{3}He, γ_{SE}, is given as a function of temperature by [57, 52]:

$$\gamma_{SE} = 6.7 \times 10^{-20} \left[\frac{\text{cm}^3}{\text{s}}\right] \cdot (1.507 \times 10^{26}) \frac{10^{-4040/T}}{T} [\text{cm}^{-3}], \tag{4.49}$$

where T is the lowest temperature inside the pumping chamber. Typically, the low temperature spot was near the bottom of the pumping chamber. A RTD was placed near that spot: rtd#7. So, T is taken to be the value read by rtd#7. The average Rb polarization, $< P_{Rb} >$, was estimated from the spin-up curves performed on various cells and applying Eq. 3.4. The results provided a range of values from 60 to 90%.

The value and uncertainty for κ^*_{epr} was calculated by taking a weighted average of the nine EPR measurements. Correlated and uncorrelated uncertainties were treated separately (Table 4.8). The χ^2_ν for the average of κ^*_{epr} for each cell was found to equal 3, this implies that the uncertainty for each cell is underestimated. To take this into account, each uncertainty was multiplied by a factor, $f = 1.725$, such that the χ^2_ν was equal to one. This same factor was then applied to the original error on the weighted

Parameter	Uncer. in Parameter	Uncer. in κ^*_{epr} [%]
Totally Uncorrelated		
$\Delta\nu$	$\pm$50 Hz	0.4
$< P_{Rb} >$	$\pm$0.15	2.0
T_p	$\pm$18°C	1.4
T_c	$\pm$1.1%	1.2
rtd#7	$\pm$5°C	2.0
Correlated by cell		
n_o	$\pm$1.2%	0.1
Φ'_{He}	$\pm$2.1%	2.1
Correlated between cells		
κ_o	$\pm$1.5%	1.5

Table 4.8: Uncertainties contributing towards the total uncertainty on κ^*_{epr}.

mean. The final estimated uncertainty for κ^*_{epr} is $\pm$2.8%, where

$$\kappa^*_{epr} = 5.66 \times 10^{-4} \left[\frac{\text{mV}}{\%\ \text{amg. cm}^2\ \text{Q}} \right]. \tag{4.50}$$

4.3 Elastic Peak Asymmetry

The constant κ^* as determined using water and EPR was checked by measuring the asymmetry in elastic scattering for electrons by a polarized ^{3}He target (Section 1.2). Two sets of elastic data were taken: at $E = 0.862$ GeV and $E = 1.72$ GeV. With this data a raw asymmetry is formed:

$$A^{Raw}_{elas} = \frac{N^{\uparrow\uparrow} - N^{\uparrow\downarrow}}{N^{\uparrow\uparrow} + N^{\uparrow\downarrow}}, \tag{4.51}$$

where $\uparrow\uparrow$ ($\uparrow\downarrow$) refers to the case when the electron and target spins are parallel (anti-parallel) with one another. N is the counting rate of elastically scattered electrons normalized to the beam current.

The raw asymmetry is related to the asymmetry (Eq. 1.17) associated with elastic

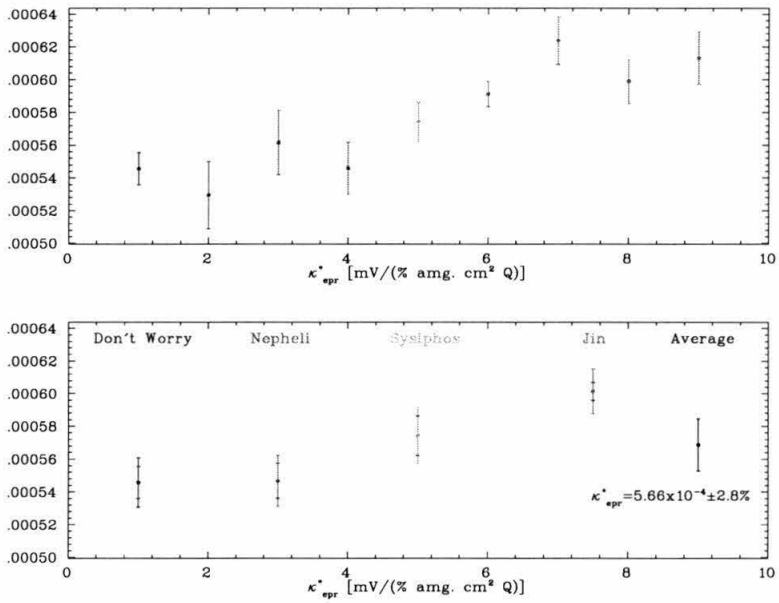

Figure 4.11: The nine EPR measurements for κ^*_{epr}. Multiple measurements for one cell were averaged before a total average of all four cells was determined.

electron scattering by

$$A^{phys}_{elas} = \frac{A^{Raw}_{elas}}{f \cdot P_b \cdot P_t}, \tag{4.52}$$

where P_b is the polarization of the electron beam, P_t is the polarization of the target, and f is the dilution factor. The dilution factor is simply the fraction of scattered electrons considered to be produced from an elastic collision compared to the total. Mistaken events mostly come from the scattering of the electrons by N_2 gas in the target cell. The dilution factor is approximately 0.993 for the 0.862 GeV data and 0.915 for the 1.72 GeV data.

A Monte Carlo simulation, that corrects for the spectrometer's acceptance and the target's spatial dimensions, was used to generate an expected asymmetry: $A^{M.C.}$. By comparing this asymmetry to the raw asymmetry, a κ^*_{elas} was calculated using

$$\kappa^*_{elas} = \frac{S_{He}}{\frac{A^{Raw}}{A^{M.C.} f P_b} \Phi_{He} G^Q n_o \left(\frac{n_c}{n_o}\right)}. \tag{4.53}$$

Systematic Uncertainties [%]	
P_b	3.0
$A^{M.C.}$	3.0
n_o	1.0
Φ_{He}	2.1
(n_c/n_o)	2.0
Total	5.2
Statistical Uncertainties [%]	
A^{Raw}(0.862 GeV)	3.5
A^{Raw}(1.72 GeV)	10

Table 4.9: Systematic and statistical uncertainty on κ^*_{elas}.

The results for the two energies are

$$\kappa^*_{elas}(0.862\text{GeV}) = 6.10 \times 10^{-4} \quad \text{and} \quad \kappa^*_{elas}(1.72\text{GeV}) = 5.99 \times 10^{-4}. \tag{4.54}$$

The uncertainties for these values are listed in Table 4.9 [70].

4.4 Calibration Results

Results for κ^* show good agreement between κ^*_{epr}, κ^*_w, and κ^*_{elas} (Figure 4.12). The final result for κ^* was calculated by taking the weighted average of κ^*_{epr} and κ^*_w. It has an uncertainty of $\pm 1.8\%$:

$$\kappa^* = (5.60 \pm 0.10) \times 10^{-4} \left[\frac{mV}{\% \cdot \text{amg.} \cdot \text{cm}^2 \cdot Q^2} \right]. \tag{4.55}$$

To calculate the constant of proportionality that relates the NMR signal to polarization, recall Eq. 4.10:

$$\kappa_{cell} = \kappa^* \Phi_{He} G^Q n_o \left(\frac{n_c}{n_o} \right).$$

Each of the parameters in Eq. 4.10 has been calculated and their uncertainties es-

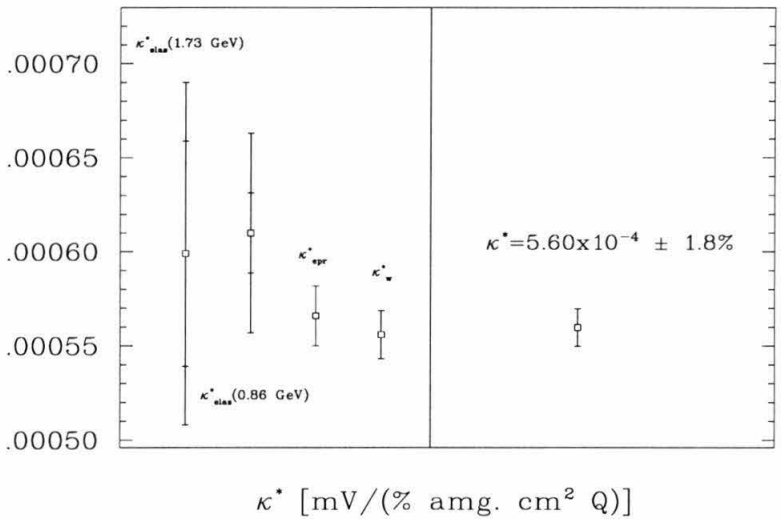

Figure 4.12: Results of the four NMR system's responsiveness, κ^*, measurements.

timated (Table 4.10). The total uncertainty assigned to κ is $\pm 3.6\%$ ($\pm 4.5\%$ for *Armageddon*). The values, depending on which cell was in use, that were used to calculate the polarization of the target are listed in Table 4.11.

Parameter	Value	Uncertainty (%)
κ^*	5.60×10^{-4}	1.8
Φ_{He}	Table 4.5	2.1
G^Q	Section 4.2.5	-
n_o	Table 3.5	1.0
$\left(\frac{n_c}{n_o}\right)$	Table 3.6	2.0
Total		3.6

Table 4.10: Contributions towards the total uncertainty on κ.

4.5 Target Performance

NMR measurements of the target's polarization were taken approximately every four hours throughout the experiment. Each data "run" lasted about 20-30 minutes and

$\kappa_{Don't Worry}$	$\kappa_{BeHappy}$	$\kappa_{Armageddon}$	$\kappa_{Nepheli}$	$\kappa_{Sysiphos}$	κ_{Jin}
0.355	0.343	0.354	0.432	0.320	0.317

Table 4.11: Values of κ for each cell in units of [mV/%].

was assigned an NMR value based upon a linear interpolation of NMR signals taken before and after the run. Depending on the cell used, the signal was divided by κ to give the polarization for that run. Results on the polarization measurements are shown in Figure 4.13. The average polarization for the experiment was ~33%.

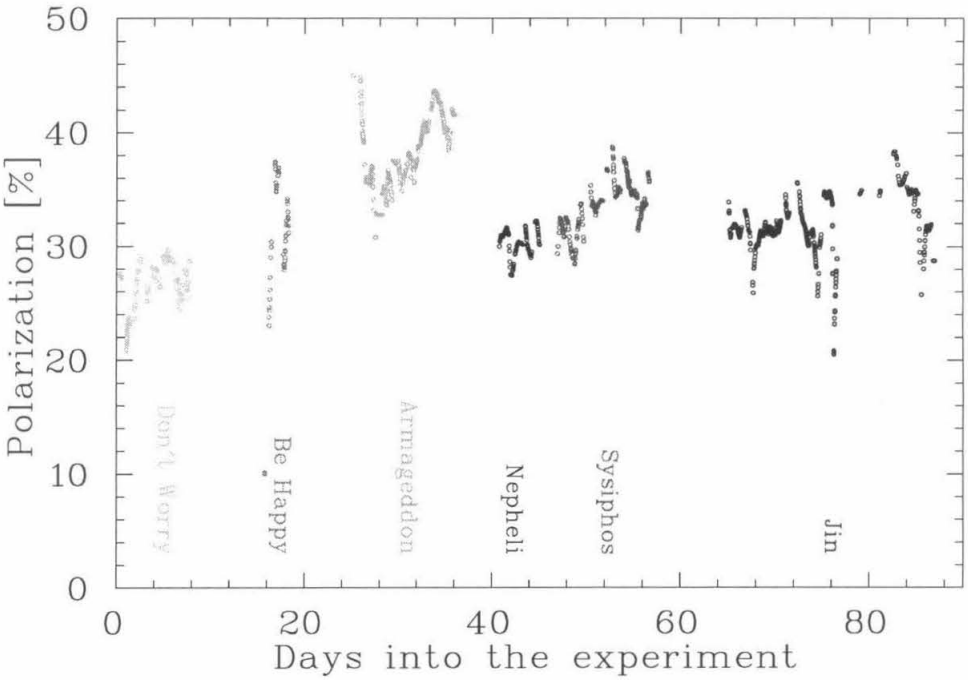

Figure 4.13: The polarization as a function of time for all of the data taken during experiment E94-010.

Chapter 5 Results

5.1 Data Collection

Nearly six billion events or 3.9 TBytes of data were recorded during the E94-010 experiment for the interaction $^3\vec{\mathrm{He}}(\vec{e}, e')X$. The event rate was about one thousand events per second. Six initial energies of the electron were used (0.86, 1.7, 2.6, 3.4, 4.3 and 5.1 GeV), and there were 38 spectrometer momentum settings (Sec. 2.3). The kinematic coverage ranged from $0.2 < Q^2 < 1.2$ GeV^2 and $0.5 < W < 2.5$ GeV (Figure 5.1).

The data was read out by the Hall A event analyzer ESPACE [71]. ESPACE used the raw data from the detector ADCs and TDCs along with a database of spectrometer constants to create a focal plane vertex (the plane of the VDCs) for each detected particle trajectory. The vertex and track are then traced back through the spectrometer to obtain kinematic information at the interaction vertex. The output of ESPACE is a series of histograms and ntuples which are used to analyze the data.

A number of cuts were applied to each data set in order to select 'good' electrons [48, 72, 73, 70]. These cuts excluded events originating from the target end windows and events that were reconstructed outside of the known acceptance of the detector. Electron identification was determined using the Čerenkov and shower detectors. Finally, a good track recorded by the VDCs was also required.

The complete data set includes information from elastic scattering up to the deep inelastic regime. Data was collected at momentum settings for both longitudinal and transverse target orientations. The polarization of the electron beam was longitudinal throughout the experiment. The GDH integral, $I(Q^2)$, was determined for 0.15

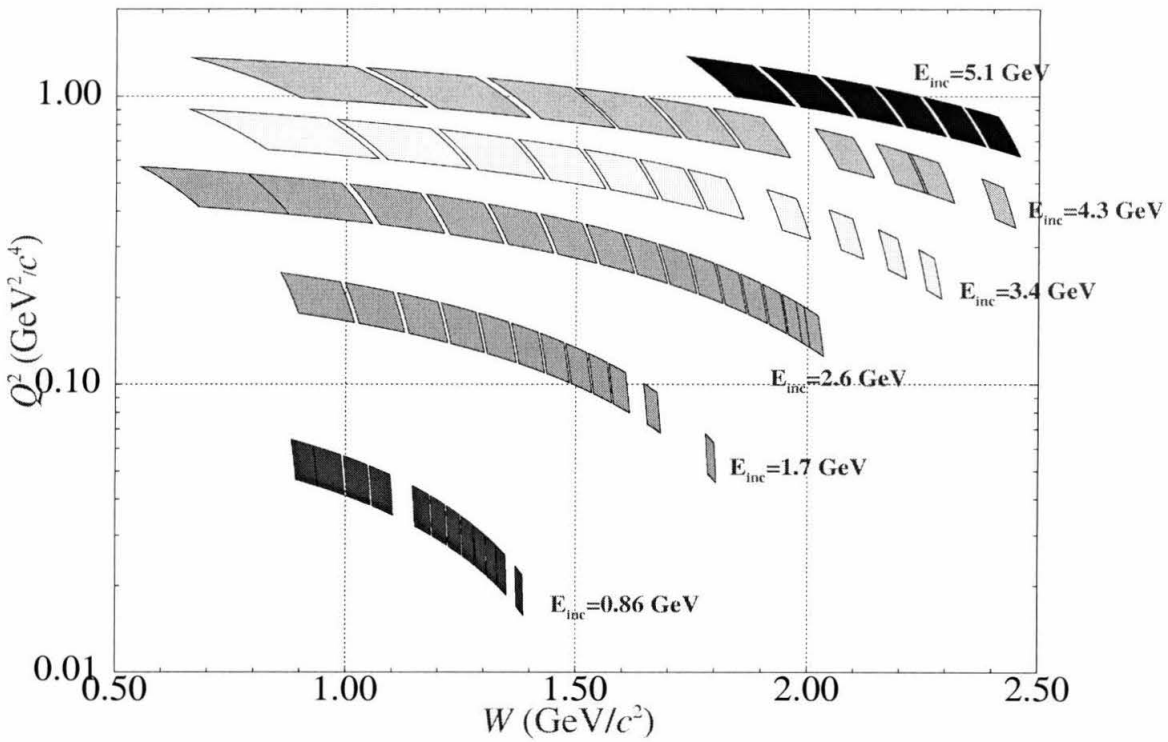

Figure 5.1: Kinematic coverage for E94-010. Each block represents one momentum setting on the spectrometer.

$\mathrm{GeV}^2 < Q^2 < 1.00\ \mathrm{GeV}^2$.

5.2 Data Analysis

The experiment collected approximately 1800 'runs'. A run is approximately 30 minutes of data collection or 1.8 million events. During and after the data collection, a portion was scanned to evaluate the data quality. Histograms of target reconstruction, acceptance, momentum, deadtime, Čerenkov ADCs, shower ADCs, and scintillator efficiencies were examined for each run.

A few problems were uncovered. The shower detector used in the HRSH spectrometer was found to have a gap between the two sets of lead glass blocks. In addition,

the detector was misaligned such that no blocks existed to record the highest momentum electrons. For the present analysis no HRSH shower detector information was used for particle identification. It was also discovered that one of the mirrors in the HRSE Čerenkov detector was misaligned and had, as a result, a very low efficiency. A correction was applied to lower the threshold on what was considered an acceptable ADC value for that mirror. Runs were excluded that demonstrated clear beam instabilities or spectrometer failures.

A number of other issues were studied in detail. The most significant systematic studies are discussed below.

5.2.1 Deadtime

Not every scattered electron is recorded as an event by ESPACE. The computer is limited to about 1 event per 800μs. Since the event rate was around 1000 Hz, most events were recorded. The percentage of events missed is called the 'deadtime' (DT). It is related to the the number of events written to a scalar (S) and the number of events recorded (T):

$$DT = 1 - \frac{T}{S} \tag{5.1}$$

One minus the deadtime is known as the 'livetime' (LT):

Since the computer readout is primarily responsible for the deadtime, it should be independent of the electron beam helicity. However, there are mechanisms that can create false asymmetries in the data. In particular, when there was a period in which the deadtime was fluctuating to large values (50-60%), the overall deadtime experienced when the electron beam had a positive helicity and when it had a negative helicity was not the same. Such periods were observed to occur when data was periodically written to a storage disk. False asymmetries as large as 0.01 occurred on a run-to-run basis.

This effect of a helicity correlated deadtime was observed and studied in the

analysis of the $E = 0.86$ GeV and $E = 1.72$ GeV elastic data [70]. Deadtimes were calculated for both positive and negative helicities:

$$DT^{\pm} = 1 - \frac{T^{\pm}}{S^{\pm}}, \tag{5.2}$$

where $T^{\pm}$ and $S^{\pm}$ are the helicity gated number of events written to tape and recorded by a scalar, respectively.

Validity of this method was verified by using data from unpolarized targets: N_2 and ^{12}C. A histogram was created of the measured asymmetry:

$$A = \frac{T^{-} - T^{+}}{T^{-} + T^{+}}. \tag{5.3}$$

During periods of small deadtime fluctuations, the distribution of A had a width of 0.001 and had a gaussian shape. A distribution of A during a period of large fluctuations had a range of ± 0.01. After dividing the rates collected during an unstable period by the helicity correlated livetime ($\frac{T^{\pm}}{LT^{\pm}}$), the distribution of A matched that for a stable period (width of 0.001 and a gaussian shape).

Runs that had large deadtime fluctuations were omitted from the data set. However, the method of calculating separate, helicity correlated, deadtimes was implemented. Generally, the ^{3}He measured asymmetries had values ranging from 0 to -0.02. The amount they changed when the helicity correlated livetime was applied ranged over ± 0.0005.

5.2.2 Optics Study

For each event, four coordinates were recorded: $x_{det}, y_{det}, \theta_{det}$, and ϕ_{det}. The position of the event in the focal plane is described by x_{det} and y_{det}, and the event's trajectory is described by θ_{det} and ϕ_{det}. These observables are used to calculate a set of quantities

located at the target [1]: x, y, θ, ϕ, and δ. The two sets of coordinates are connected through a set of tensor relations. Calculation of the tensors required placing targets in the beamline at known positions, recording events, and changing the tensor values until an accurate reconstruction of the target is produced. For a detailed description of this process see [74, 75].

For this experiment, a series of ^{12}C elastic data was taken in order to optimize the tensors for event reconstruction. The carbon target consisted of seven thin carbon foil targets spaced evenly along the beam path (Figure 3.10). The total length covered was 40 cm. Data was collected with and without a sieve slit collimator (Figure 5.2). The sieve slit consisted of 49 holes in a grid pattern. Exact knowledge of the sieve hole positions and the carbon target foils allowed for optimization of the tensors needed for event reconstruction. The results from the optics study are listed in Table 5.1.

Angular resolution (FWHM)		Angle determination accuracy
ϕ	$\pm$2.0 mr	$\pm$0.2 mr
θ	$\pm$6.5 mr	$\pm$0.8 mr
Momentum resolution (FWHM)		
δ at target center	3×10^{-4}	
δ overall	4×10^{-4}	
Transverse position resolution (FWHM)		Transverse position accuracy
y	3.7 mm	$\pm$0.5 mm

Table 5.1: Resolution of the target vertex.

5.2.3 Efficiencies

In order to calculate a cross section, the trigger inefficiency, or percentage of time the trigger did not fire when it should have, needed to be determined. Normally, both planes of scintillators need to fire in order for an event to trigger. By looking

[1] The position of event vertex is given by x and y. The trajectory of the particle from the target is given by ϕ and θ. The event's relative momentum is given by $\delta = \frac{p-p_o}{p_o}$, where p_o is the central momentum of the spectrometer and p is the momentum of the event.

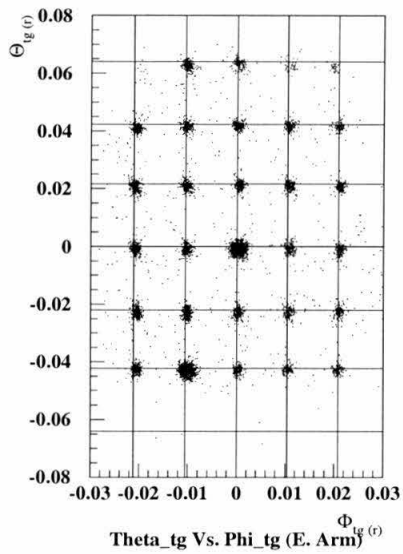

Figure 5.2: Data collected from the carbon target with the sieve slit in. The data represents the location of the events as they enter the spectrometer.

at events that fire only one plane, but otherwise were normal (i.e., a good track from the VDCs and a hit in the shower counter), and comparing those to the number of events that fire both planes, a map of the trigger inefficiency of the focal plane was determined. This map of inefficiency is generated using several runs and is calculated throughout the experiment. The global inefficiency was about 4.3%. The recorded data is corrected for this inefficiency to determine the total absolute event rate.

In addition to the trigger efficiency, efficiencies for the Čerenkov detector, the shower detector, and the VDCs were all determined. Just as in the case of the trigger, each detector was studied by looking at the number of times the detector did not fire when it should have as compared to the number of times it did. For all of the detectors listed above, the efficiencies were found to be >99%.

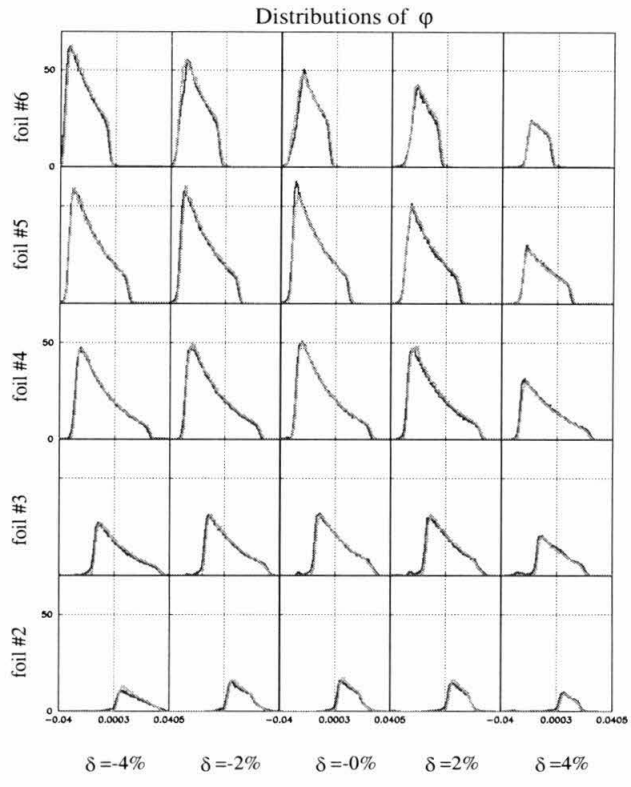

Figure 5.3: A comparison of elastic ^{12}C data (red) and the Monte Carlo (green) distributions for ϕ at the focal plane. Each row is a different carbon foil and each column is a different value of δ: -4%, -2%, 0%, 2%, and 4%.

5.2.4 Monte Carlo

Once the deadtime, spectrometer optics, and efficiencies were understood, a Monte Carlo was developed to understand the angular acceptance and momentum acceptance of the spectrometers [76]. The results of the Monte Carlo were checked against actual ^{12}C elastic data. By folding in the detector efficiencies, the deadtime, and the physics of ^{12}C elastic cross section, the Monte Carlo was able to predict a cross section to within $\pm$4% of the measured results (Figure 5.3). This accuracy is in line with, or slightly better than, previous experiments using the Hall A spectrometers [49].

In addition to the ^{12}C elastic data, the elastic data from ^{3}He was compared to a

prediction made by the Monte Carlo. Both the ^{3}He cross section and asymmetry were checked. The cross section agrees within error bars and the asymmetry also shows good agreement when data from both arms are combined (Figures 5.4 and 5.5).

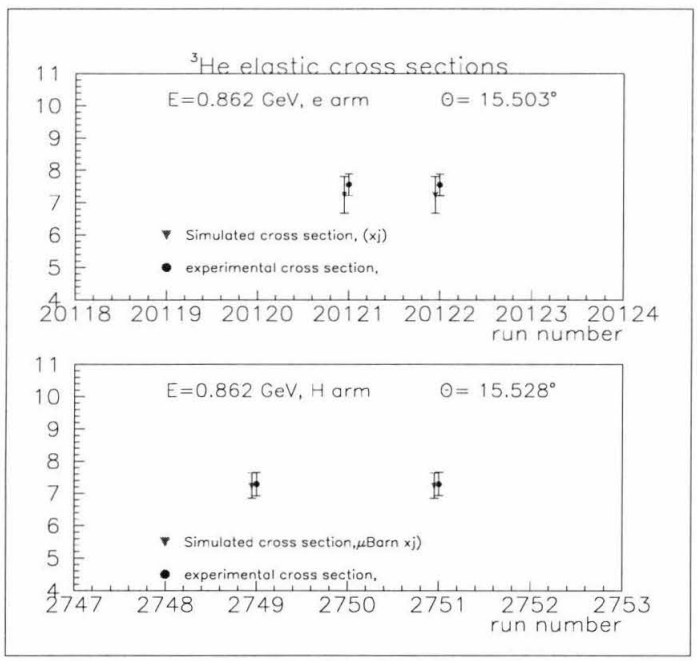

Figure 5.4: Comparison of the $E = 0.86$ GeV elastic data cross section for ^{3}He and the Monte Carlo prediction for two runs. The top plot shows the results from the HRSE spectrometer and the bottom is from the HRSH spectrometer. The vertical scale is in μbarns.

5.2.5 Pion Rejection

As discussed in Sections 2.3.3 and 2.3.4, the Čerenkov and shower detectors were used together to identify and reject pions. The Čerenkov detector, in principal, can reject all pions; however, occasionally a pion will knock off an electron which in turn is detected by the Čerenkov and gives a false identification. The shower detector has the ability to reject pions by measuring the ratio of the deposited energy and

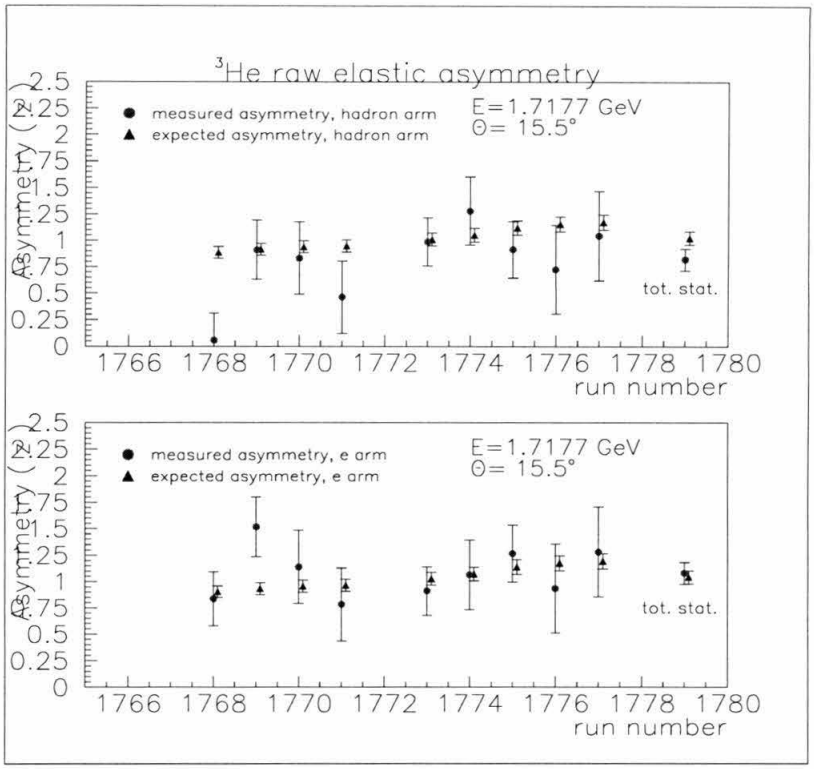

Figure 5.5: Comparison of the $E = 1.72$ GeV elastic data cross section for ^{3}He and the Monte Carlo prediction for two runs. The top plot shows the results from the HRSH spectrometer and the bottom is from the HRSE spectrometer. The vertical scale is in μbarns.

the momentum: E/p (Figure 5.6). The amount of pion contamination is determined by fitting the pion and electron peaks from the shower detector. By comparing results with and without a Čerenkov cut and calculating the amount of pion tail underneath the electron peak, it was found that the ratio of pions to electrons (π/e^-) was negligible: $\approx 10^{-4}$ [72].

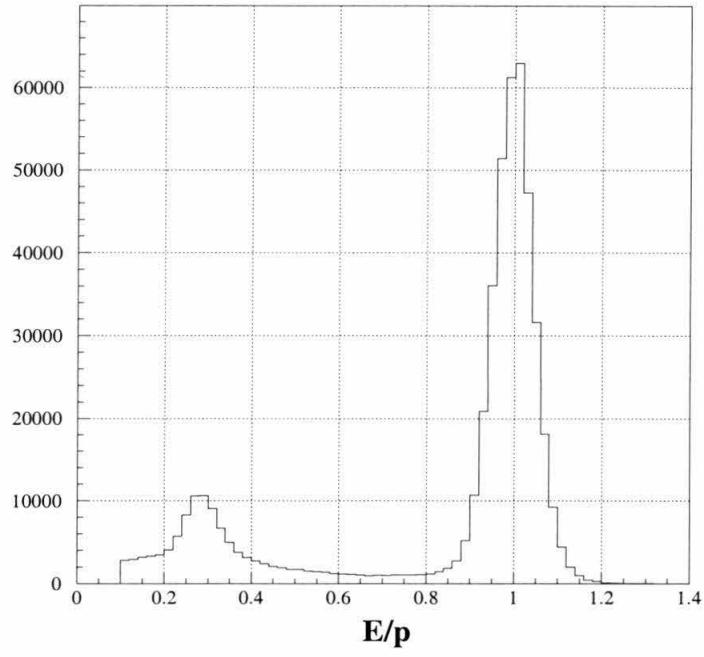

Figure 5.6: The E/p histogram for $E = 3.4$ GeV and $p_o = 2.199$ GeV. A cut on pions can be made by rejecting events with E/p<0.8.

5.2.6 Radiative Corrections

Corrections due to radiative effects (external and internal) were included in the analysis. External radiation involves the loss of electron energy as it passes through matter: external bremsstrahlung. For the E94-010 target, the external corrections included the glass windows and walls of the target and the ^{3}He itself. The effect of the external radiation is to cause a lower interaction energy at the event vertex and a lower perceived scattered energy. Corrections to the data for this type of radiation were done using the technique in [77].

Internal radiation includes emission of a real or virtual photon during the interaction between the electron and the target nuclei. Figure 5.7 shows six possible interactions. Diagrams **a** and **b** represent the emission of a real photon before or

after the interaction. Diagrams **c** and **d** represent the emission and re-absorption of a virtual photon by the incident or scattered electron. Diagram **e** represents exchange of a virtual photon between the incident and scattered electron. Diagram **f** represents the renormalization of the virtual photon due to vacuum polarization. Corrections for these types of radiative processes were done using a modified version of the program POLRAD [78, 79].

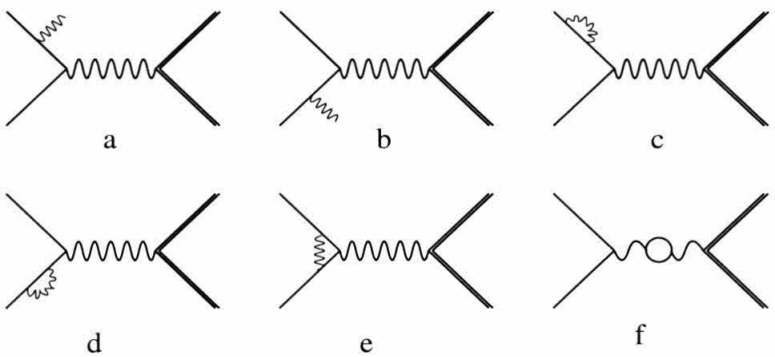

Figure 5.7: Six possible internal radiative processes.

Application of external and internal radiative corrections requires knowledge of the polarized and unpolarized cross sections over a wide kinematic range. These quantities have not been measured in the region of our data. Nuclear models [2] had to be used in order to perform the radiative corrections. The radiative corrections changed the shape of the cross sections dramatically (Figure 5.8), especially for the lower ν bins.

At present, there is no estimation of the uncertainty on the corrections for each ν bin. It is believed that the corrections for higher incident electron energies will later be understood due to further studies from data at lower energies. The corrections to the $E = 0.86$ GeV data are the most suspect because they rely upon models of the ^{3}He polarized cross sections at lower energies. This will in turn affect the corrections to the $E = 1.72$ GeV, which will influence the $E = 2.59$ GeV corrections and so on.

Overall, the radiative corrections dominate the lower incident electron cross sec-

tions. For the higher energy cross sections, corrections are as high as 50%. The corrections do not have as great an effect on the asymmetries. Typically, $A_{||}$ and $A_{\perp}$ were affected between 5 and 20% of their values.

5.3 Measured Quantities

For each momentum setting, a differential cross section was measured for each spin configuration of beam and target ($\uparrow\uparrow, \downarrow\uparrow, \uparrow\leftarrow$, and $\downarrow\leftarrow$):

$$\frac{d^2\sigma(\nu, Q^2)}{dEd\Omega} = \frac{N_{goode^-}}{N_e N_t \Delta E \Delta\Omega \varepsilon LT} \times RADCOR \tag{5.4}$$

where N_{goode^-} is the number of 'good' electrons recorded, N_e is the number of incident electrons, N_t is the target thickness in nuclei per unit area, ΔE is the energy width of the spectrometer, $\Delta\Omega$ is the solid angle of the spectrometer, ε represents the total efficiency (namely the multiplication of trigger, tracking, Čerenkov, and shower efficiencies), LT is the computer live-time, and $RADCOR$ is a radiative correction.

The recorded data was used to form two asymmetries:

$$A_{||}(\nu, Q^2) = \frac{1}{P_{beam} P_{target} f} \frac{\frac{N^{\downarrow\uparrow}_{goode^-}}{N^{\downarrow}_e LT^-} - \frac{N^{\uparrow\uparrow}_{goode^-}}{N^{\uparrow}_e LT^+}}{\frac{N^{\downarrow\uparrow}_{goode^-}}{N^{\downarrow}_e LT^-} + \frac{N^{\uparrow\uparrow}_{goode^-}}{N^{\uparrow}_e LT^+}} \tag{5.5}$$

and

$$A_{\perp}(\nu, Q^2) = \frac{1}{P_{beam} P_{target} f} \frac{\frac{N^{\downarrow\leftarrow}_{goode^-}}{N^{\downarrow}_e LT^-} - \frac{N^{\uparrow\leftarrow}_{goode^-}}{N^{\uparrow}_e LT^+}}{\frac{N^{\downarrow\leftarrow}_{goode^-}}{N^{\downarrow}_e LT^-} + \frac{N^{\uparrow\leftarrow}_{goode^-}}{N^{\uparrow}_e LT^+}}, \tag{5.6}$$

where P_{beam} is the polarization of the incident electrons, P_{target} is the polarization of the target, $N^{\uparrow\uparrow(\uparrow\downarrow)}$ is the number of events recorded when the beam and target polarizations are aligned (anti-aligned), $N^{\uparrow\leftarrow(\downarrow\leftarrow)}$ is the number of events recorded when the beam and target polarizations are perpendicular, $N_e^{\uparrow(\downarrow)}$ is the number of incident electrons with positive (negative) helicity, and $LT^{+(-)}$ is the livetime when the initial

electron helicity is positive (negative). The dilution factor, f, is the percentage of recorded events originating from the ^{3}He nuclei.

The largest contribution to the dilution comes from the presence of N_2 gas located in the target chamber. For values of ν above the elastic peak,

$$f \approx 1 - \frac{\#\text{ of } N_2 \text{ nuclei}}{\#\text{ of } ^3\text{He nuclei}} \approx 0.94. \tag{5.7}$$

For values of ν in the region of the ^{3}He elastic peak, the N_2 elastic cross section influences the amount of dilution. Using N_2 elastic data taken using the reference target, it was found [70] that $f \approx$0.99 for the E=0.86 GeV elastic peak, and $f \approx$0.91 for the E=1.72 GeV elastic peak.

The results with $P_{beam} = 70\%$ and $P_{target} = 30\%$ are shown in Figures 5.9 and 5.10.

For both $A_{||}$ and $A_{\perp}$ there is significant dynamic behavior. The asymmetries move from positive to negative values as the scattering moves from one regime to the next. The data for $A_{||}$ (E=3.4 GeV) illustrates this point. For $\nu \approx$ 400 MeV, the quasi-elastic peak is positive. The asymmetry then changes to a large negative value for the Δ resonance at $\nu \approx$650 MeV. It then returns to nearly zero before becoming large and negative again for the higher resonances.

Some general characteristics are noteworthy. For $A_{||}$, the Δ resonance, located at 250 to 750 MeV depending on the energy, is large for all incident energies. It is negative and has a magnitude of $\sim$0.02 over the entire range of incident energies. The quasi-elastic peak for $A_{\perp}$ is negative with magnitude of $\sim$0.02 over the entire range of incident energies. Outside of the quasi-elastic peak for $A_{\perp}$, the asymmetries tend towards zero for increasing beam energy.

The measured quantities in Eq. 5.4 are combined to form relations to the spin

structure functions, G_1 and G_2:

$$\frac{1}{P_{beam}P_{target}}\frac{d\sigma}{dE'd\Omega}(\downarrow\uparrow - \uparrow\uparrow) = \frac{4\alpha^2}{M^3Q^2}\frac{E'}{E}[MG_1(E + E'\cos\theta) - Q^2G_2] \tag{5.8}$$

and

$$\frac{1}{P_{beam}P_{target}}\frac{d\sigma}{dE'd\Omega}(\downarrow\leftarrow - \uparrow\leftarrow) = \frac{4\alpha^2}{M^3Q^2}\frac{E'^2}{E}\sin\theta[MG_1 + 2EG_2]. \tag{5.9}$$

These equations are used to solve for G_1 and G_2 (Figures 5.11). There is some noteworthy behavior displayed by the evolution of g_1 and g_2. Large changes were measured from one incident energy to the next for g_1. The value of g_1 goes from about -0.1 to -0.6 when the incident energy is increased from 2.6 to 3.4 GeV. Interestingly, over much of the range shown $g_2 \simeq -g_1$. This is in line with a prediction for the twist-2 contribution to g_2 by Wadzura and Wilcek [80]:

$$g_2^{WW}(x, Q^2) = -g_1(x, Q^2) + \int_x^1 \frac{dx'}{x'}g_1(x', Q^2). \tag{5.10}$$

In regions were ν is small and x fairly high, the contribution of the integral to g_2^{WW} is small, and $g_2 \sim -g_1$.

Comparison of $g_1^{^3He}(Q^2)$ measured by this experiment and that measured by SLAC experiment E154 [3] show good agreement even though the E94-010 data is at a lower Q^2 value (Figure 5.12).

The values for $G_1(\nu, Q^2)$ and $G_2(\nu, Q^2)$ were used to calculate the value of $\sigma_{TT}(\nu, Q^2)$:

$$\sigma_{TT}(\nu, Q^2) = (\sigma_{1/2} - \sigma_{3/2}) = \frac{8\pi^2\alpha}{M^3\left(\nu - \frac{Q^2}{2M}\right)}(M\nu G_1 - Q^2G_2). \tag{5.11}$$

The results for σ_{TT} are shown in Figure 5.13. The Δ and quasi-elastic peaks are now clearly seen. Both peaks have large values and have opposite signs. One challenge from this data is to disentangle the quasi-elastic and Δ peaks, which still overlap. This spillage can most clearly be seen in the $E = 2.6$ GeV data set. There is a

sharp zero crossing at ν =375 MeV. Understanding the contamination is important for calculating the GDH neutron integral.

The uncertainties on $A_{||}$, $A_{\perp}$, and σ_{TT} are primarily dominated by systematic uncertainties. There is a 5% uncertainty due to beam and target polarizations. There is an additional uncertainty on σ_{TT} from the acceptance: ~4%. The spectrometer angle adds an uncertainty of ~1%. The target spin angle adds an uncertainty of ~1% for $A_{||}$ and σ_{TT} and ~5% for $A_{\perp}$. Uncertainties due to the beam energy, deadtime, and dilution are small and have been neglected. Uncertainties on the spectrometer efficiency are currently estimated to be a few percent. Overall there is currently believed to be about a 10% uncertainty from all parameters together, other than the radiative corrections, in both asymmetries and cross section measurements [81].

5.4 The GDH Integral for ^{3}He and the Neutron

Calculation of the GDH integral, $I(Q^2)$, for Q^2 values of 0.03, 0.17, 0.39, 0.66, and 1.04 GeV, was performed by integrating σ_{TT} for each initial energy:

$$I^{He}_{GDH}(\bar{Q^2}) = \sum_{i=\nu_1}^{\nu_f} \frac{\sigma_{TT}(E,\nu_i)}{\nu_i}(\nu_{i+1} - \nu_i), \tag{5.12}$$

where $\bar{Q^2}$ is the Q^2 value at the Δ resonance, ν_i is the value of ν at the zero crossing between the quasi-elastic peak and Δ resonance, and ν_f is the highest value of ν for an incident energy E. This method provides only an approximation to the actual GDH integral for the neutron after extraction, since it integrates primarily over the Δ resonance which is expected to be the dominate contribution. It, however, does a poor job of including contributions from the higher energy resonances especially for the $E = 0.862$ GeV and $E = 1.72$ GeV cases. The integration is carried over constant E, not constant Q^2, as needed to represent properly the integral.

In order to extract neutron results using ^{3}He, the relationship between neutron and

^{3}He polarizations needs to be taken into account. To first order, the ^{3}He wavefunction of Friar *et al.* [21] can be used. From groundstate ^{3}He wavefunction calculations, they showed that the protons within ^{3}He are about 3% polarized in the opposite direction compared to the ^{3}He polarization. The neutron is about 87% polarized in the direction of the ^{3}He polarization. More recently, it was suggested by C. Ciofi degli Atti and S. Scopetta [2] to extract the extended GDH integral using the following relation:

$$\tilde{I}^{He}(Q^2) = 2p_p I^p(Q^2) + p_n I^n(Q^2), \tag{5.13}$$

where I^x is the GDH integral at a particular Q^2 and $p_{p(n)}$ is the effective polarization produced by the S' and D waves in the ground state of ^{3}He. They point out that extraction of $G_1^n(\nu, Q^2)$ using their method works in the deep inelastic region but is limited in the resonance region (the region of interest). However, extraction of a neutron GDH integral from ^{3}He is possible when the appropriate effective polarizations are used. For the purpose of an $I^n(Q^2)$ extraction from the calculated integral of Eq. 5.12, the effective polarizations p_p and p_n are set to 0 and 0.87 respectively. This extraction is shown in Figure 5.14 and listed in Table 5.2. The simple extraction does not follow a proposed evolution of the GDH integral as proposed by Burkert and Li [1], nor does the evolution towards -232.8μb at $Q^2 = 0$ appear likely. A number of effects that could alter the extrapolated values have yet to be fully understood and taken into account.

When the integration includes the quasi-elastic peak, an approximation of the GDH integral for ^{3}He is made. This is also shown in Figure 5.14. The evolution of this curve towards a point at $Q^2 = 0$ appears to be large and positive. This is in sharp contrast to the value of -496μb as predicted by the GDH sum rule.

$\bar{Q}^2$ [GeV]	$I^n_{GDH}(Q^2)$ [μb]
0.03	-62
0.17	-112
0.39	-51
0.66	-29
1.04	-14

Table 5.2: Calculated values of $I^n_{GDH}(\bar{Q}^2)$.

5.5 Interpretation

There are a number of issues yet to be investigated before the simple approximation of the GDH integral for the neutron can be believed. The integration performed using Eq. 5.12 was constant in energy, not constant in Q^2 as is necessary for proper representation of the GDH integral. However, this assumption should not change the results significantly, since most of the weight of the integral lies over the Δ resonance which is mainly at constant Q^2 (0.182 to 0.153 GeV in one case).

Another possible cause for the disagreement between the results using the simple approximation of the GDH integral for the neutron and the calculation done by Burkert and Li could be the existence of quasi-elastic events in the region of integration. The height of the quasi-elastic peak is positive and a factor of four larger compared to the Δ peak for the lower energies (Figure 5.13). These quasi-elastic events could spill into the more heavily weighted low ν bins.

For the two lowest energies, those corresponding to $I^n(\bar{Q}^2$=0.03 GeV) and $I^n(\bar{Q}^2 =$ 0.17 GeV), there is good separation of the quasi-elastic and Δ peaks. Yet, it is these points that disagree the most from prediction.

The cross sections for the other three incident energies do not show a clear separation between peaks. The effect on $I^n(\bar{Q}^2)$ from the quasi-elastic contamination should be small because of the relatively small size of the quasi-elastic peak. The values for $I^n(\bar{Q}^2)$ corresponding to these energies seem in line with the prediction.

Contribution from unmeasured resonances could also move the results. The data

for $\sigma_{TT}(E = 0.86$ GeV) does not extend high enough in ν to include resonances other than the Δ resonance. These higher energy resonances will increase the value of $I^n(\bar{Q} = 0.03$ GeV). Also, further extension in ν for the $\sigma_{TT}(E$=3.4 and 4.2 GeV) data sets will increase $I^n(\bar{Q} = 0.66$ GeV) and $I^n(\bar{Q} = 1.0$ GeV).

Some of these issues can be resolved by studying the radiative corrections to the quasi-elastic peak. With further study the 1.72 GeV data should be corrected. The 0.86 GeV data will probably not be corrected sufficiently to understand the evolution of the cross section because of the lack of lower energy data.

Lastly, there is another possibility as to the apparent discrepancy of the GDH sum rule and the evolution of the GDH integral towards a value at Q^2=0; the GDH sum rule could itself be incorrect. Of the underlying assumptions made in the derivation of the sum rule, the no subtraction dispersion relation is the most suspect. The no subtraction assumption implies that the value of the Compton scattering amplitude (Eq. 1.66) $f_2(\nu) \to 0$ as $\nu \to \infty$. If it is shown that a subtraction is necessary, it could indicate, among others things [82], that the constituent quarks have an anomalous magnetic moment or, in other words, internal structure. Such conjectures from the results of this experiment would be reckless, but it is interesting and humorous to consider.

Less in question is the GDH integral for ^{3}He. Here the integral is expected to evolve towards larger and larger positive values as $Q^2 \to 0$. Then, suddenly, it is expected to drop towards the real photon point of -496 μb. This is perhaps not as surprising as it seems. The GDH sum rule is a prediction for a real photon. The cross section for a real photon has no elastic or quasi-elastic interactions. Just how the quasi-elastic peak makes the transition from a large positive value, for virtual photons, to zero, for real photons, requires data with real photon beams. More data is required to observe this exciting behavior.

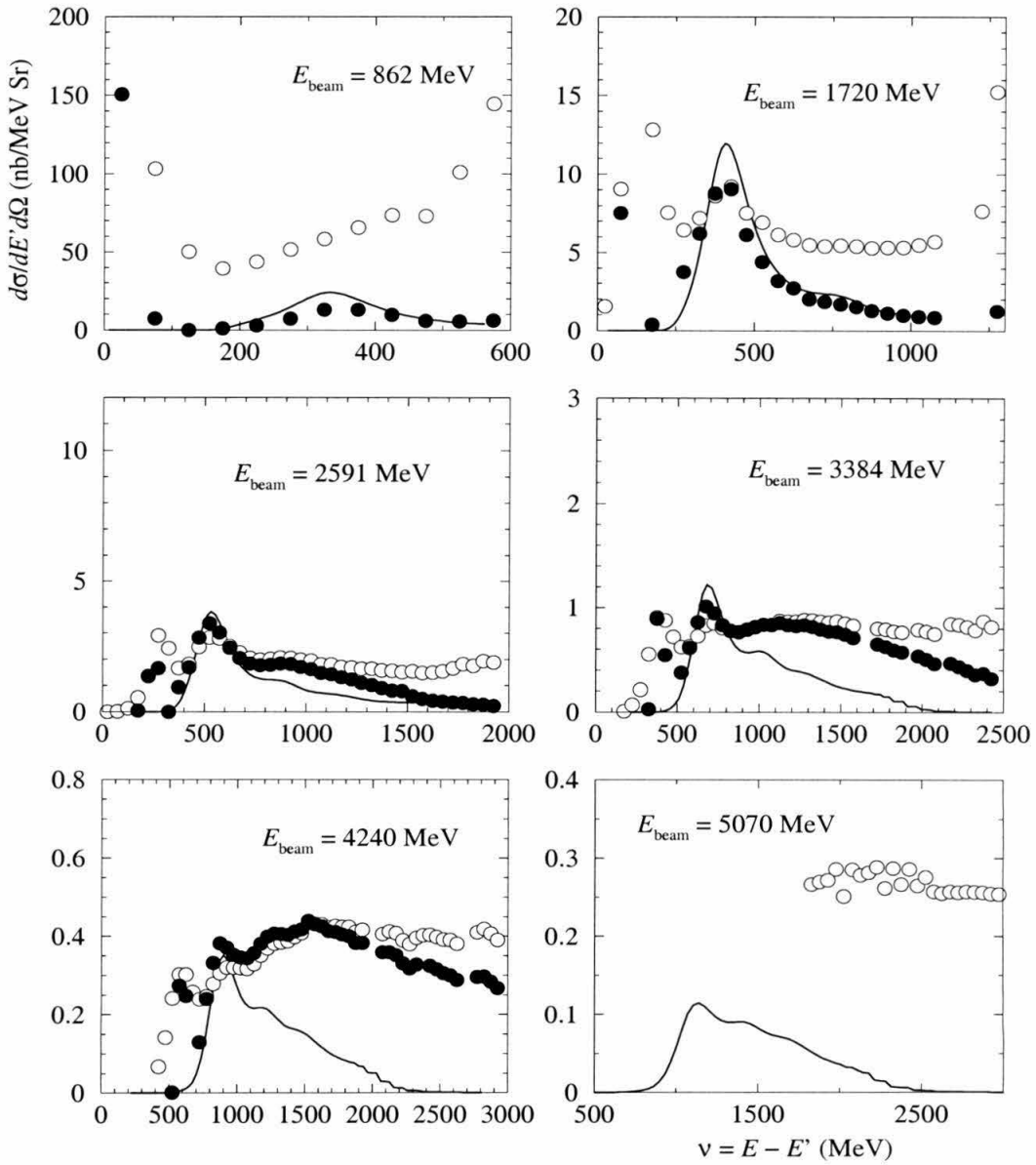

Figure 5.8: The ^{3}He cross section. The open circle points correspond to data without radiative corrections. The solid circle points are after radiative corrections are applied. The solid line is a calculation performed by Scopetta [2].

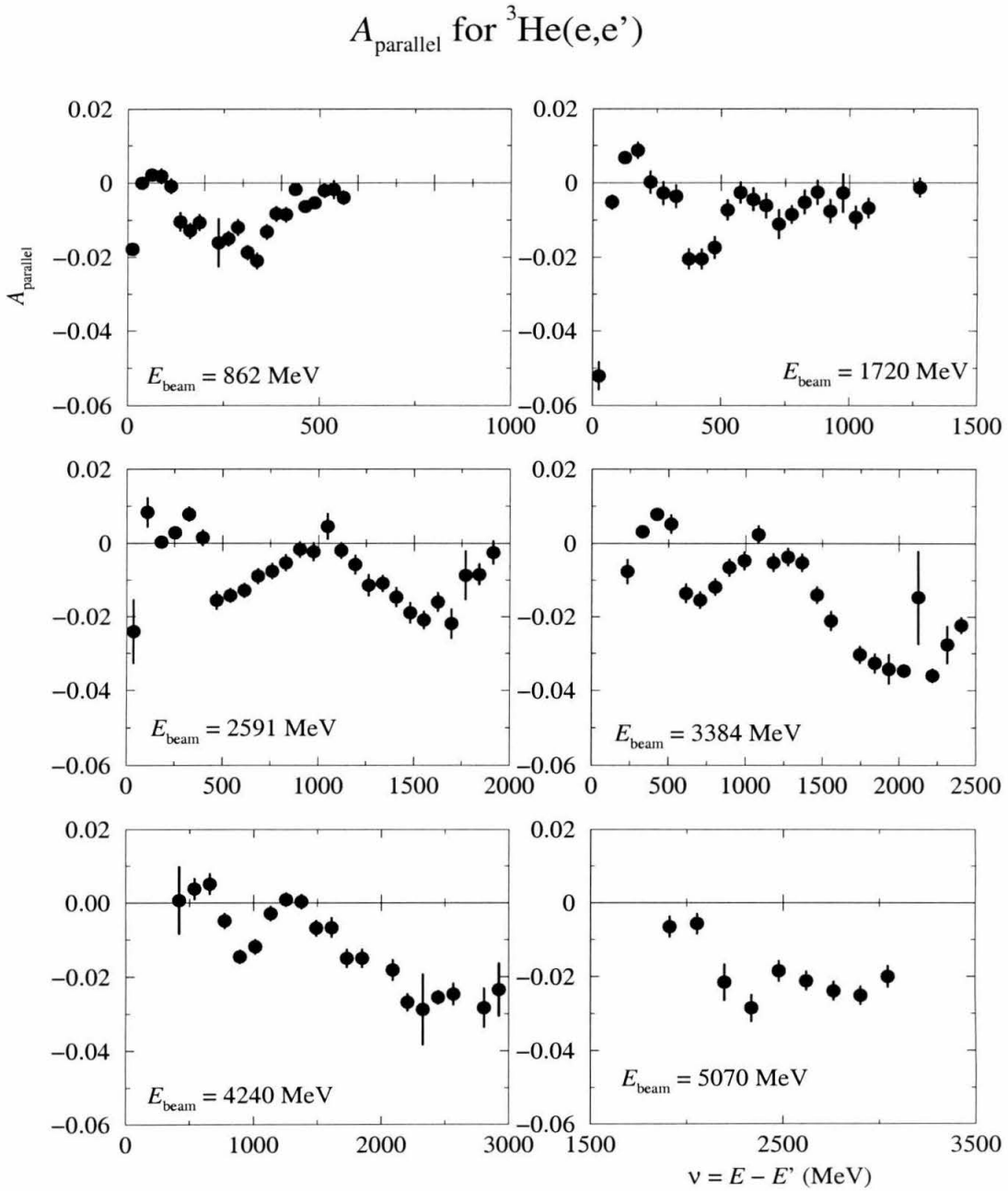

Figure 5.9: $A_{||}$ for the six initial beam energies. Error bars shown are statistical only.

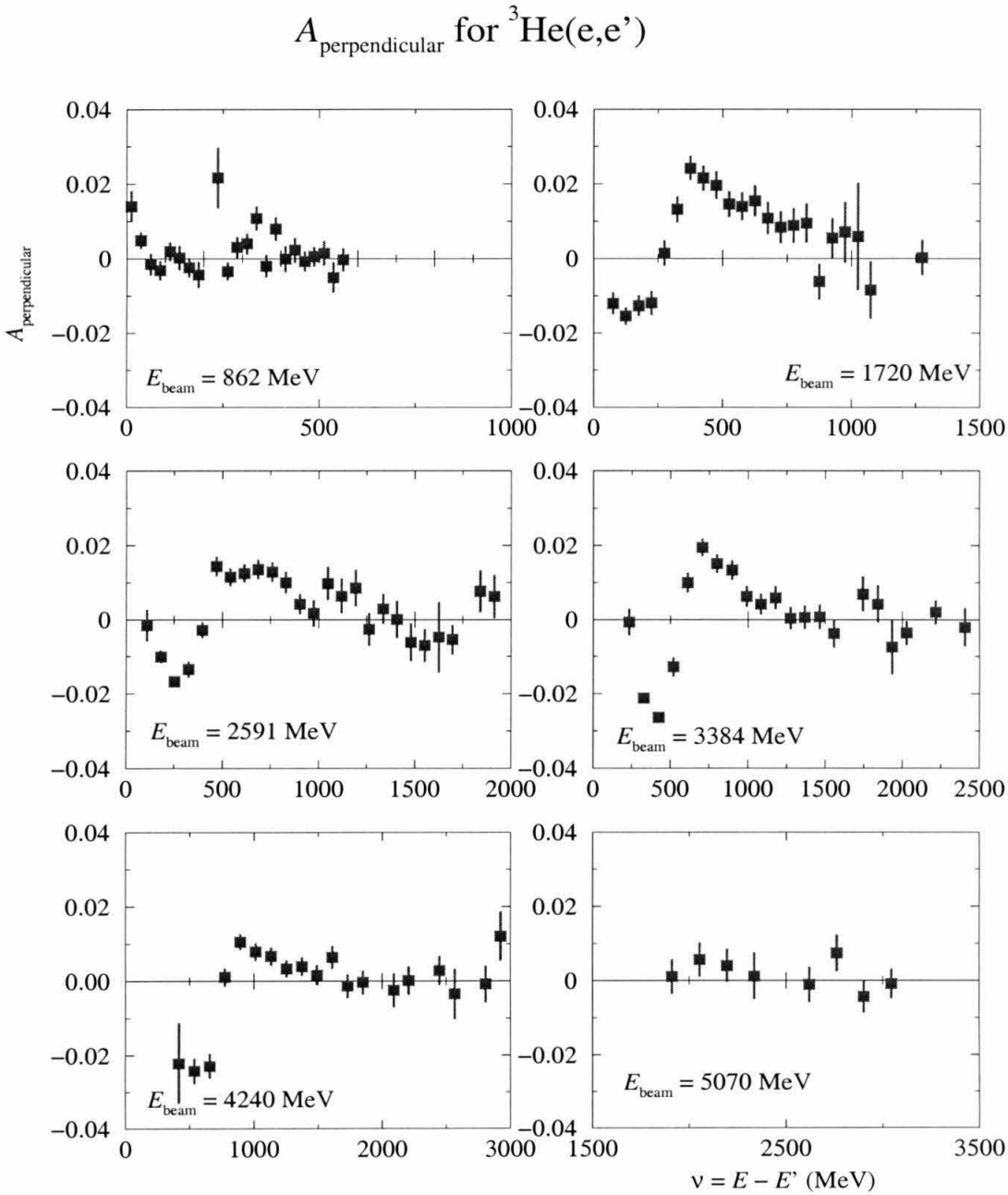

Figure 5.10: $A_\perp$ for the six initial beam energies. Error bars shown are statistical only.

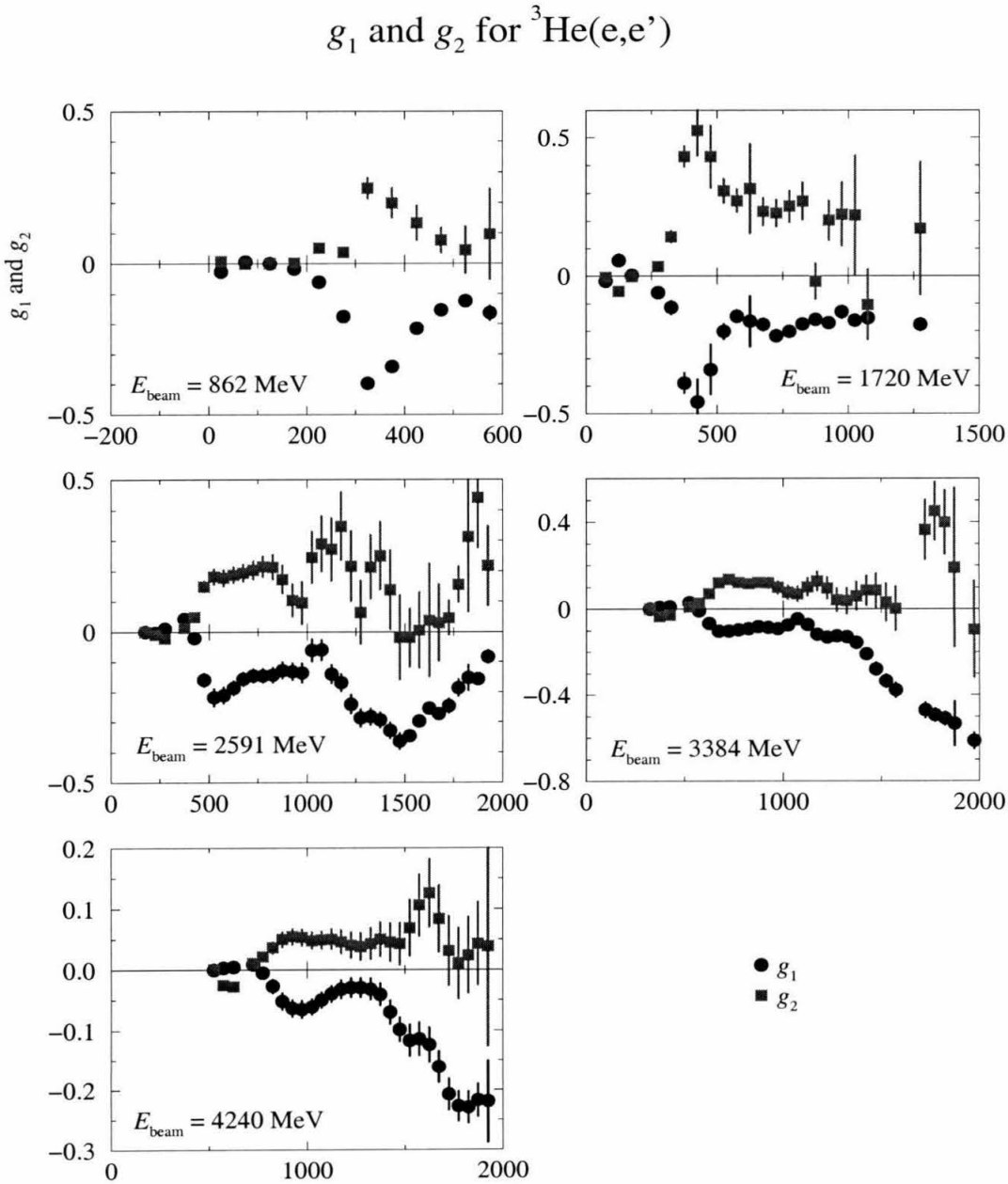

Figure 5.11: Results for the spin dependent structure function $g_1^{^3He}(\nu, Q^2) = \frac{\nu}{M} G_1$ and $g_2^{^3He}(\nu, Q^2) = \frac{\nu^2}{M^2} G_2$. Error bars are statistical only.

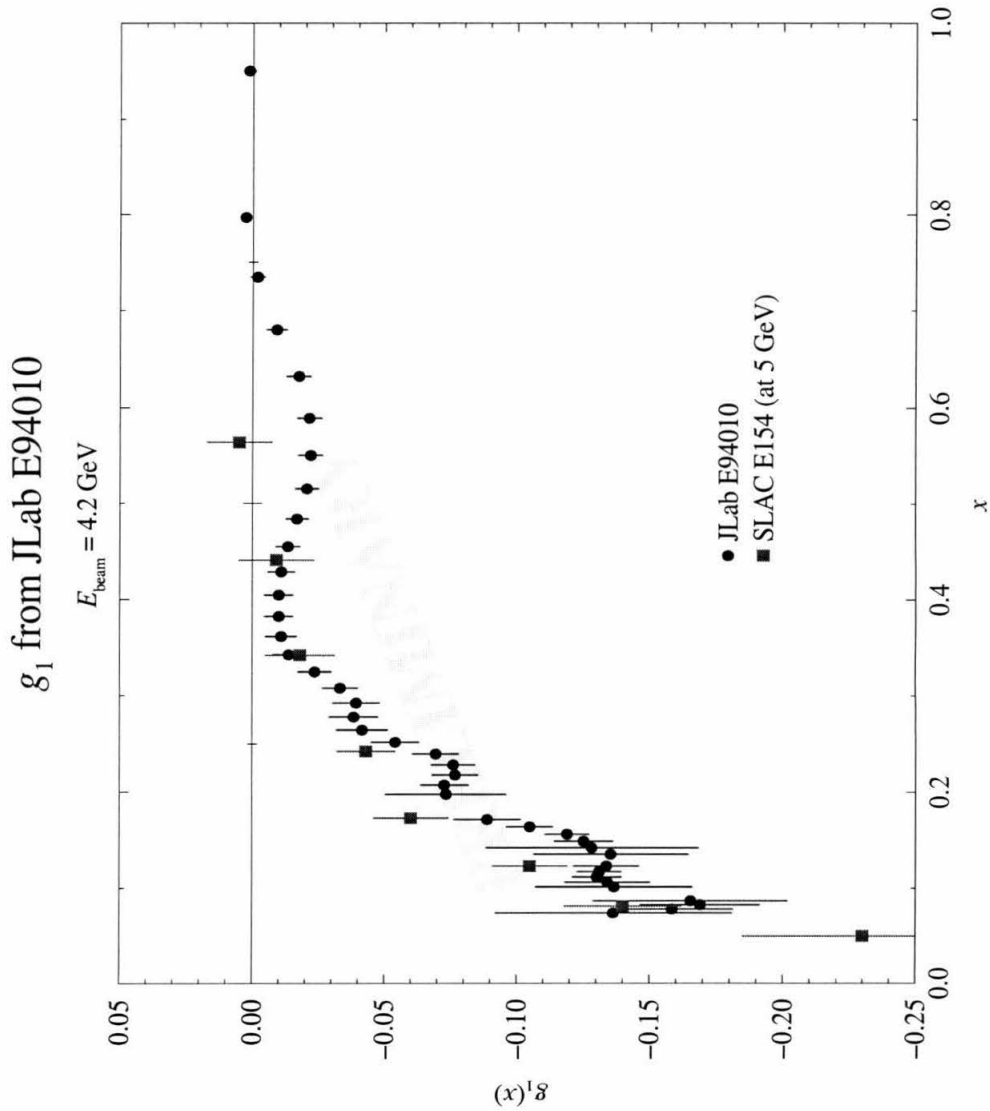

Figure 5.12: Comparison between $g_1^{He}(x) = \frac{\nu}{M} G_1^{He}$ as measured by this experiment and SLAC E154 [3] in the deep inelastic region.

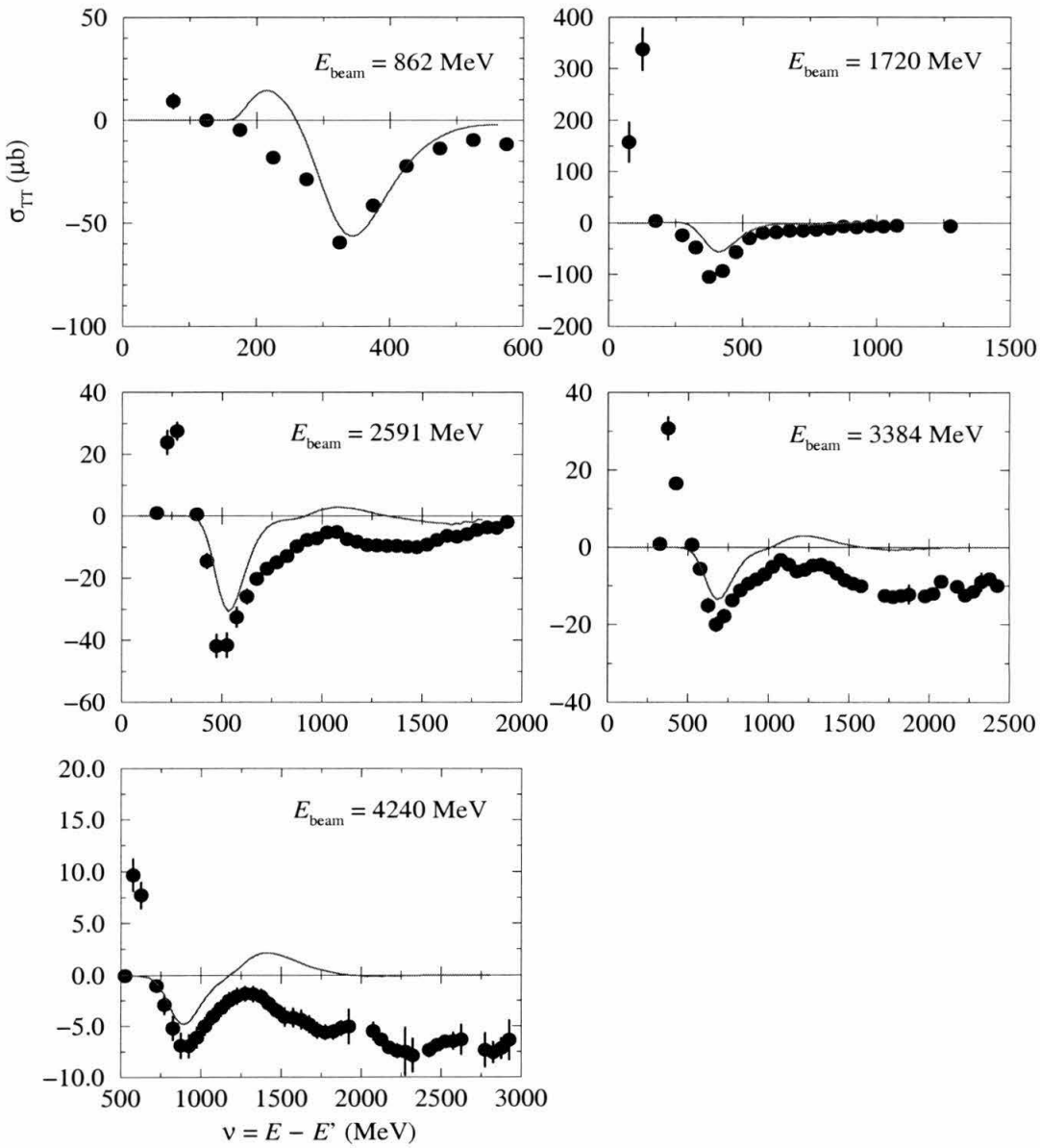

Figure 5.13: σ_{TT} plotted as a function of ν for five of the initial beam energies. Error bars shown are statistical only. The solid line is a calculation for the Δ resonance performed by Scopetta [2].

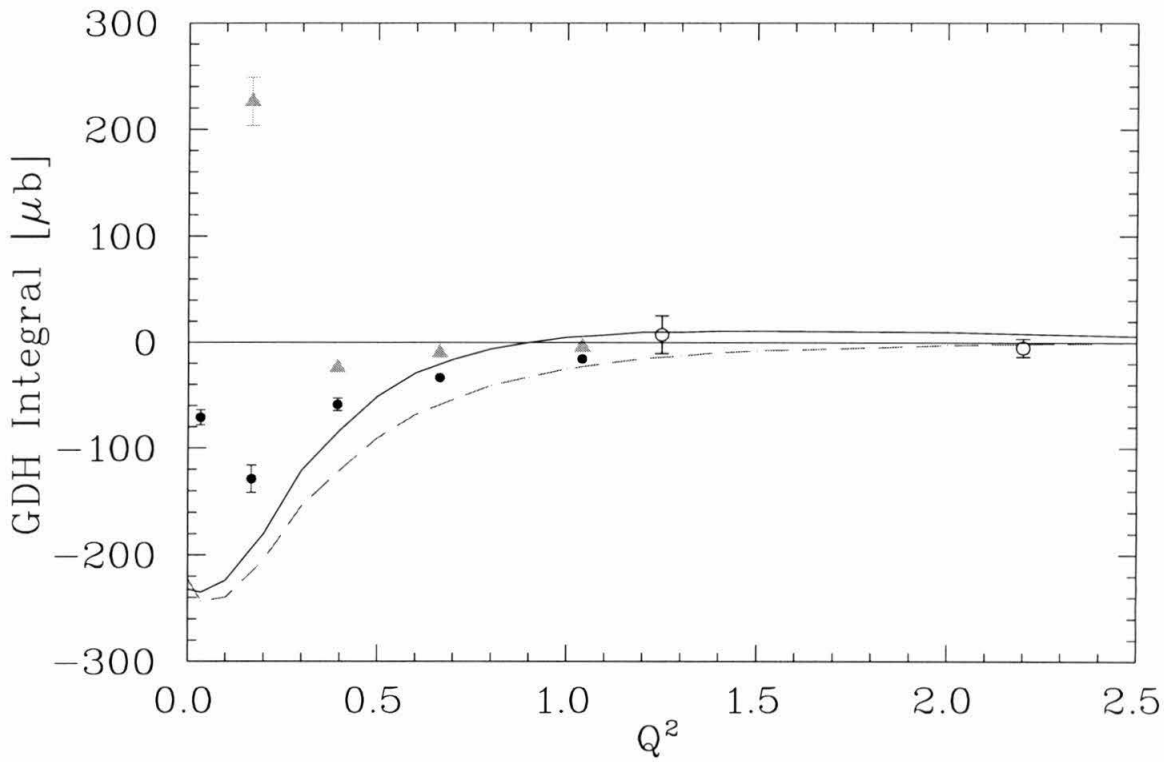

Figure 5.14: The GDH integral. The solid blue circles are results of a neutron extraction from this experiment (Eq. 5.12). The solid green triangles are results of an integration that includes the quasi-elastic peak. A 10% systematic uncertainty is placed on each extracted point of the GDH integral. The statistical uncertainty is negligible. The open black circles are results from Hermes [4] for a neutron. The solid line is the calculation performed by Burkert and Li [1] of the evolution of the GDH integral for a free neutron. The dashed line is the same calculation including only the Δ contribution.

Chapter 6 Conclusion

Jefferson Lab experiment E94-010 marks the first time the polarized ^{3}He cross sections have been measured at low Q^2. The measurements provide information in the quasi-elastic and resonance regions. At this time the analysis is still preliminary, but it does raise some interesting questions concerning the GDH integral for the neutron and ^{3}He. For the neutron, extrapolation of the GDH integral towards $Q^2 = 0$ is far from the real photon point. Uncertainties to be investigated may move the data more in line with predictions, but further measurement in this region is required. For ^{3}He, the GDH integral is expected to have dramatic behavior at very low Q^2 as a result of the data from this experiment. This dramatic behavior would be a direct consequence of the differences between real and virtual photons.

What is needed now is an experiment dedicated toward measuring the polarized ^{3}He cross section in the low to very low Q^2 region. Fortunately, such an experiment is set to take data in the summer of 2002. Jefferson Lab experiment E97-110, *The GDH Sum Rule and the Spin Structure of ^{3}He and the Neutron Using Nearly Real Photons*, will take data on the polarized ^{3}He cross sections at lower Q^2 and higher ν compared to E94-010 (Figure 6.1).

Increasing the kinematic coverage beyond that of E94-010 is made possible by the installation of two septum magnetics. A septum magnetic is a dipole magnet constructed to deflect electrons. The magnet will allow for measurements at more forward angles than currently possible in Hall A. Electrons scattering at an angle of 6° will be possible, whereas presently the minimum angle is 12.5°. This magnet will be added by moving the target upstream and placing them at the previous target location. Implementing this change reduces the angular acceptance from 7.2 msr to 3.7 msr and worsens the momentum resolution from 1.0×10^{-4} to 2.0×10^{-4}, but the

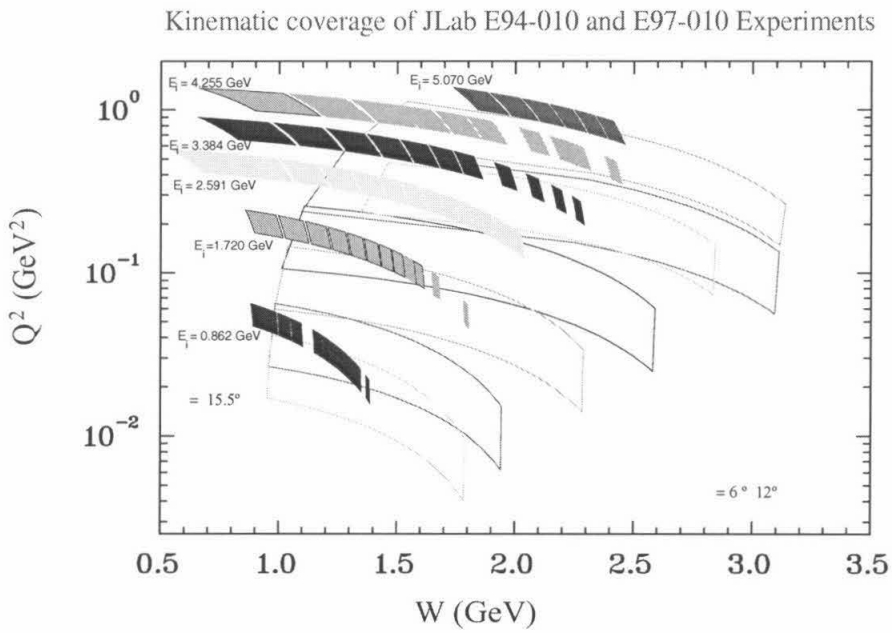

Figure 6.1: Comparison of kinematic coverage for experiments E94-010 and E97-110. The solid boxes represent the measured kinematic of E94-010. The open boxes represent the proposed kinematic coverage of E97-110.

total momentum range should remain unchanged (from 0.4 to 4.0 GeV).

Other than the septum magnetic, experiment E97-110 mirrors E94-010 in a number of ways. It will use six beam energies: 1.6, 2, 3, 4, 5, and 6 GeV. The scattered electrons will cover the ^{3}He quasi-elastic, resonance, and deep inelastic regions. It will use the same polarized ^{3}He target and polarized beam. It will also run for about the same amount of time: 3 months.

With the proposed data, more contributions to the GDH integral will be extracted (Figure 6.2). The goal of the experiment is to extrapolate the GDH integral to Q^2=0 and determine its slope at that point. Chiral perturbation theory predicts a positive

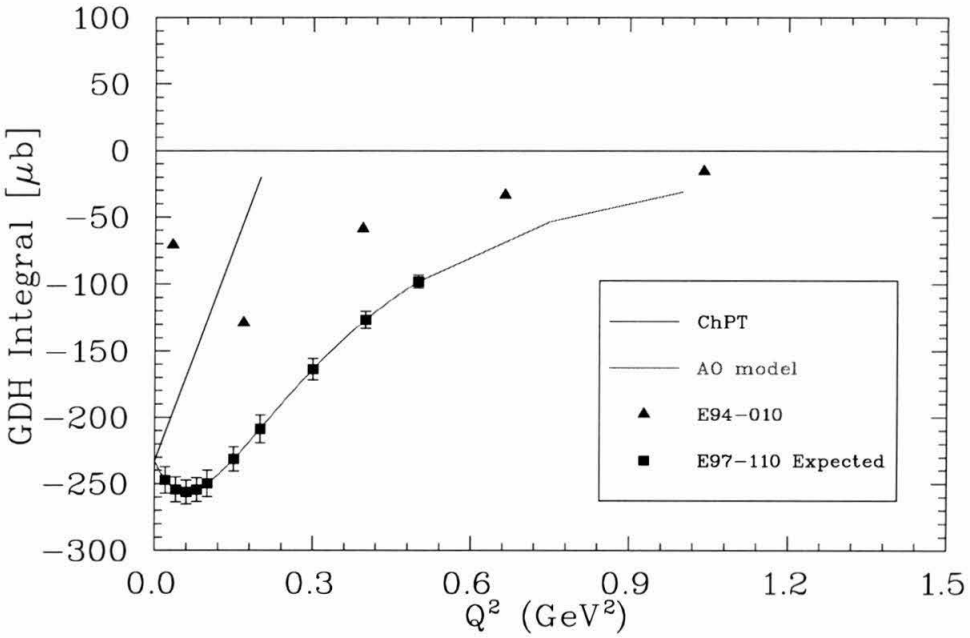

Figure 6.2: Expected precision of the E97-110 experiment for the measurement of the GDH integral. Error bars are systematic and statistical uncertainties added in quadrature.

slope [83], whereas phenomenological models predict a negative slope [1].

Experiment E94-010 and soon E97-110 are just two experiments in a long history of polarized electron scattering experiments. Early experiments sought to understand the spin structure at high Q^2. In this regime nuclear effects are small and the picture of the nucleon is one of quark and gluon interactions. It is described using perturbative QCD. These experiments determined the contribution of the quarks to the total nucleon spin and verified the Bjorken sum rule.

In contrast, this experiment collected data in the transition region between two regimes. One regime is that of the earlier experiments where quark-gluon interactions dominate. The other regime considers ^{3}He as a set of coherent hadrons. The experimental data of Jefferson Lab experiment E94-010 represents a first step towards understanding the transition region using polarized ^{3}He scattering. The hope

is that someday a consistent theory across all energies (such as lattice QCD) will be developed.

Bibliography

[1] V. Burkert and Z. Li, Physical Review D **47**, 46 (1993).

[2] C. C. degli Atti and S. Scopetta, Physics Letters B **404**, 223 (1997).

[3] K. Abe *et al.*, Physical Review Letters **79**, 26 (1997).

[4] K. Ackerstaff *et al.*, Physics Letters B **444**, 531 (1998).

[5] J. Ashman *et al.*, Physics Letters B **206**, 364 (1988).

[6] J. Ashman *et al.*, Nuclear Physics B **328**, 1 (1989).

[7] G. P. Ramsey, hep-ph/9702227 (unpublished).

[8] Alguard *et al.*, Physical Review Letters **41**, 70 (1978).

[9] G. Baum *et al.*, Physical Review Letters **51**, 1135 (1983).

[10] B. Adeva *et al.*, Physical Review D **58**, 364 (1998).

[11] P. Anthony *et al.*, Physical Review D **55**, 6620 (1996).

[12] K. Abe *et al.*, Physical Review D **58**, 112003 (1998).

[13] P. Anthony *et al.*, Physics Letters B **463**, 339 (1999).

[14] A. Airapetian *et al.*, Physics Letters B **442**, 484 (1998).

[15] E. Hughes and R. Voss, Annual Review of Nuclear and Particle Science **49**, 303 (1999).

[16] S. Boffi, C. Giusti, and F. Pacati, Physics Reports **226**, 1 (1993).

[17] N. d'Hose, Physics from MAMI and ELSA to ELFE (unpublished).

[18] T. Donnelly and A. Raskin, Annuals of Physics **169**, 247 (1986).

[19] P. Dunn *et al.*, Physical Review C **27**, 71 (1983).

[20] F. Close, *An Introduction to Quarks and Partons* (Academic Press, New York, 1979).

[21] J.L.Friar *et al.*, Physical Review C **42**, 2310 (1990).

[22] V. W. Hughes and J. Kuti, Annual Review of Nuclear and Particle Science **33**, 611 (1983).

[23] U. Stiegler, Physics Reports **277**, 1 (1996).

[24] K. Althoff *et al.*, Z. Phys. **327**, 327 (1979).

[25] V. Burkert, Jefferson Lab publication: PR-93-035 (unpublished).

[26] J. Bjorken, Physical Review **148**, 1467 (1966).

[27] S. Larin, F. Tkackev, and J. Vermaseren, Physical Review Letters **66**, 862 (1991).

[28] S. Gerasimov, Soviet Journal of Nuclear Physics **2**, 430 (1966).

[29] S. Drell and A. Hearn, Physical Review Letters **16**, 908 (1966).

[30] M. Gell-Mann, M. Goldberger, and W. Thirring, Physical Review **95**, 1612 (1954).

[31] G. Arfken, *Mathematical Methods for Physicists* (Academic Press, New York, 1985).

[32] F. Low, Physical Review **96**, 1428 (1954).

[33] M. Gell-Mann and M. Goldberger, Physical Review **96**, 1433 (1954).

[34] D. Drechsel, Progress in Particle and Nuclear Physics **34**, 181 (1995).

[35] M. Anselmino, B. Ioffe, and E. Leader, Soviet Journal of Nuclear Physics **49**, 136 (1989).

[36] X. Ji and J. Osborne, hep-ph/9905410 (unpublished).

[37] R. Alley *et al.*, Nuclear Instruments and Methods in Physics Research A **365**, 1 (1995).

[38] R. Prepost and T. Maruyama, Annual Review of Nuclear and Particle Science **45**, 41 (1995).

[39] A. Glamazdin, Fizika B **8**, 91 (1999).

[40] D. Griffiths, *Introduction to Electrodynamics* (Prentice Hall, New Jersey, 1989).

[41] L. Levchuk, Nuclear Instruments and Methods in Physics Research A **345**, 496 (1994).

[42] K. Unser, IEEE Transactions on Nuclear Science **16**, 934 (1969).

[43] V. Pascal, Nuclear Physics News **9**, 12 (1999).

[44] D. H. Perkins, *Introduction to High Energy Physics* (Addison-Wesley, London, 1982).

[45] K. Fissum *et al.*, MIT-LNS Internal Report #0397 (unpublished).

[46] J. Jackson, *Classical Electrodynamics* (Wiley, New York, 1975).

[47] M. Iodice *et al.*, Nuclear Instruments and Methods in Physics Research A **411**, 223 (1998).

[48] K. Slifer, E94-010 Technical Report #32 (unpublished).

[49] K. R. McCormick, Ph.D. thesis, Old Dominion University, 1999.

[50] M. V. Romalis, Ph.D. thesis, Princeton University, 1997.

[51] W. Happer, Review of Modern Physics **44**, 169 (1972).

[52] A. B.-A. Baranga *et al.*, Physical Review Letters **80**, 2801 (1998).

[53] T. Chupp *et al.*, Physical Review C **36**, 2244 (1987).

[54] W. Happer *et al.*, Physical Review A **29**, 3092 (1984).

[55] S. Applet *et al.*, Physical Review A **58**, 1412 (1998).

[56] M. Wagshul and T. Chupp, Physical Review A **49**, 3854 (1994).

[57] T. Killian, Physical Review **27**, 578 (1926).

[58] S. Appelt *et al.*, Applied Physics Letters **75**, 427 (1999).

[59] K. Moller, *Optics* (University Science Books, California, 1988).

[60] I. Kominis, E95-010 Technical Note #25 (unpublished).

[61] M. Romalis, E. Miron, and G. Cates, Physical Review A **56**, 4569 (1997).

[62] B.Larson *et al.*, Physical Review A **44**, 3108 (1991).

[63] P. of Nuclear Magnetism, *A. Abragam* (Oxford University Press, Oxford, 1994).

[64] H. Goldstein, *Classical Mechanics* (Addison-Wesley, Reading, Massachusetts, 1980).

[65] M. Romalis and G. Cates, Physical Review A **58**, 3004 (1998).

[66] J. Simpson and H. Carr, Physical Review **111**, 1201 (1956).

[67] S. Meiboom, Journal of Chemical Physics **34**, 375 (1961).

[68] G. K. Woodgate, *Elementary Atomic Structure* (Oxford University Press, Oxford, 1989).

[69] J. Kestin *et al.*, Journal of Physical Chemistry (Reference Data) **13**, 229 (1984).

[70] A. Deur, E94-010 Technical Report #33 (unpublished).

[71] E. Offermann and M. Kuss, ESPACE Manual Version 2.7.0 (1998) (unpublished).

[72] K. Slifer, E94-010 Technical Report #31 (unpublished).

[73] A. Deur, E94-010 Technical Report #29 (unpublished).

[74] H. Gao, Ph.D. thesis, Massachusetts Institue of Technology, 1999.

[75] N. Liyanage, Hall A Technical Report (unpublished).

[76] J. LeRose, hallaweb.jlab.org/news/minutes/tranferfuncs.html (unpublished).

[77] L. Mo and Y. Tsai, Review of Modern Physics **41**, 205 (1969).

[78] T. Kuchto and N. Shumeiko, Nuclear Physics 412 (1983).

[79] I. Akushevich and N. Shumeiko, Journal of Physics 513 (1994).

[80] S. Wandzura and F. Wilczek, Physics Letters 195 (1977).

[81] J. Chen, E94-010 spokesperson, private comunitation (unpublished).

[82] R. Pantforder, Ph.D. thesis, Physikalisches Institut der Universitat Bonn, 1998.

[83] G. Cates, J. Chen, and F. Garibaldi, E94-110 proposal (unpublished).